Synthesis and Raman Characterisation of Transition Metal Dichalcogenides

---

A thesis presented to the University of Dublin, Trinity College
for the degree of
Doctor of Philosophy in Chemistry

by

Maria O'Brien

Under the supervision of Prof. Georg S. Duesberg
School of Chemistry & AMBER

March 2017 Trinity College Dublin

Declaration

I declare that this thesis has not been submitted as an exercise for a degree at this or any other university and it is entirely my own work. Where I have consulted the published work of others, this is always clearly attributed. Where the thesis is based on work done by myself jointly with others, I have made clear exactly what was done by others and what I have contributed myself. I agree to deposit this thesis in the University's open access institutional repository or allow the Library to do so on my behalf, subject to Irish Copyright Legislation and Trinity College Library conditions of use and acknowledgement..

……………………………………….

Maria O'Brien, March 2017

Acknowledgements

First and foremost, I would like to thank my supervisor, Prof. Georg Duesberg, for allowing me the opportunity to pursue my research under his supervision, and for his help and support throughout the past four years. Without his insight and guidance none of this would have been possible. The ASIN group has been a great source of friendship and knowledge, and it's been a pleasure to work with and become friends with its members. There are a few special thank-yous owed to group members from over the years: to Sinéad for her advice, friendship, noises and cake; to Christian for the pumpkin spice lattes, dungeon defending, and story edits on the equipment calendars; to Hugo for many long, entertaining conversations (always about science, of course); to Nina for her never-ending support for pub time, girls night, and the Halloween parties; to Conor and John for always keeping my self-confidence at a realistic level, and asking where their names are on the acknowledgements; and finally to Niall for his encouragement, advice, coffee-breaks, falafel lunches, the pronunciation and spelling of many words, proof-reading, equipment-training, and for putting up with me not writing enough papers. Thanks also to all the other various members of the ASIN group over the years for their friendship, support and help in the lab – Toby, Kay, Hye-Young, Chanyoung, Daniela, Wungyeon, Hyun-Jeong , Ehsan, Riley, Kim, Katie, Lisanne, Alison, and the other summer students and interns of which there are too many to name individually.

I would like to thank all of the people who helped me over the course of my research, through collaborations and use of various equipment and tools. Firstly, I'd like to thank Dr. Niall McEvoy, for training on every tool I've used in the lab, in particular the Raman microscope, and for his immeasurable help, advice and support in my research. I'd like to thank Dr. Nina Berner and Conor Cullen for many, many XPS measurements and subsequent analysis. Thanks also to Clive Downing and Dermot Daly in the AML for their help with training and use of the TEM, FIB and SEM, and to all the AML staff for general help and assistance at every step of the way. I'd like to thank Dr. Kangho Lee and Riley Gatensby for furnace construction and automation, and Dr. Toby Hallam for help with AFM measurements. Thanks to Dr. Rachel Morrish and Prof. Colin Wolden for their XPS measurements on plasma-synthesised WS_2 and to Dr. Kangho Lee for gas-sensing measurements. Thanks to Dr. Hye-Young Kim for EBL device manufacture and measurements and to Dr. Damien Hanlon and J.B. Boland in Prof. Coleman's group for TMO dispersions that were used in our synthesis recipes. Thanks to Dr. Carlo Motta and Prof. Stefano Sanvito for their theoretical calculations on the phonon dispersion curves and band diagrams of our materials. Thanks to Dr. Nils Scheuschner and Prof. Janina Maultzsch from Berlin for many interesting and useful Raman discussions, and for providing the patterned substrates used to suspend MoS_2 over cavities here. Thanks to Prof. Jani Kotakoski, Prof. Jannik C. Meyer, and Kenan Elibol in Vienna for STEM measurements and interesting insights on MoS_2 and $PtSe_2$ films. Thanks to Dr. Jian-Yao Zheng and Prof. John Donegan for their help with blue laser and polarized Raman spectroscopic measurements.

None of this would be possible without financial support, and I would therefore like to extend my sincere gratitude to the Irish Research Council and Intel Ireland for their support *via* the Enterprise Partnership Scheme, Project 201517, Award 12508. I'd also like to thank my mentors from Intel over the last number of years, Dr. Alan Bell for help with device manufacture, Dr. Jennifer McKenna for her advice and support, and Chris Murray for both lab advice and for always having a great story to tell.

Finally, thanks to my friends and family: to Cairenn, who is one of the most generous and kind people I've ever known, and always cheers me up when I'm down; to Kate, who I've been annoying since first year physics labs in 2009, and yet, somehow, still puts up with me; to Claudia, for her excellent research advice and encouragement, but also for being a great friend and confidant; to Michelle and Sarah-Louise for always organising get-togethers of friends, and for much needed tea breaks; to the extended PCAM class of 2013 for always providing a welcome distraction from work, and never staying on-track for more than 3 messages in whatsapp group chats; to the large extended CRANN family (without naming them all individually) for lunchtime, office, and hallway chats; to the Social Elite crowd, for providing the most fun way to spend a Saturday evening in Dublin; to my large extended family, both in Cork and Dublin, who are unwavering in their support – with a special thanks to my grandad, Gaga, for being the only one who knew what a chalcogenide was, no matter how many times I told the rest of them; and to my siblings, Mar, Ger, and Tom, ~~for making it so easy for me to be the favourite child,~~ for their support, encouragement, and offers to "take care of" my enemies. Last, but not least, to my parents, Kay and Mike, for their unwavering love, for supporting my education for over 20 years, and for always encouraging me to do what makes me happy.

Abstract

In recent years there has been an increased interest in layered materials such as Transition Metal Dichalcogenides (TMDs). When isolated in their monolayer form, they are essentially a 2D material, with unique properties. The implementation of 2D materials into future electronic devices could be desirable for industry; as their potential applications include cheap, fast and flexible electronic devices. Furthermore, to fully exploit the unique electrical properties of these materials, such as high electron mobility, new synthesis, manipulation, integration and characterisation techniques must be developed.

The first part of this thesis focuses on the reliable vapour phase synthesis of TMDs. Initial research focused on the thermally assisted chalcogenisation of pre-deposited layers. The successful growth of crystalline, uniform thin films of MoS_2 indicated that this process was a significant step towards growth of TMD films in a manner compatible with techniques used in the semiconductor industry. Electrical transport in WS_2 films was highly sensitive to the presence of NH_3 gas, which was the first reported demonstration of a gas sensing response for WS_2 thin films. A sensitivity of 1.4 ppm NH_3 in nitrogen at room temperature was achieved, indicating device sensitivity comparable with commercially available metal-oxide-semiconductor and solid electrolyte sensors. However, films produced using these methods were typically polycrystalline, and therefore “bottom-up” chemical vapour phase synthesis methods were required to create single crystals with a high degree of crystallinity in the lattice. Highly crystalline TMD monolayers were realised by using a close proximity precursor supply in a microreactor setup. Monolayer TMD single crystals were synthesised with high reproducibility. A wide range of spectroscopic, microscopic, and electrical characterisation techniques reveal the high quality of the TMD samples produced, which could be used in the future for the facile production of electronic device components.

The second part of this thesis focuses on the spectroscopic characteristics of vapour phase grown TMDs. Raman characterisation of vapour phase grown $PtSe_2$ thin polycrystalline films is presented. $PtSe_2$ thin films were grown by conversion of Pt films to $PtSe_2$ at low temperatures under Se atmosphere. Scanning transmission electron microscopy measurements of these films experimentally confirmed the crystal structure to be 1T, which allowed predictions to be made of the phonon dispersion curve and expected frequencies of vibrational modes. These modes were experimentally confirmed and found to depend on film thickness for a variety of laser excitation wavelengths.

Chemical vapour deposition (CVD) grown TMDs were studied using low-frequency Raman spectroscopy. This allowed the measurement of the shear and layer-breathing modes in the multilayer crystals, which were visualised in maps. It was found that these low-energy Raman modes allowed the assessment of layer number, as well as stacking configuration (2H or 3R), of multilayer TMDs in a fast and reliable manner. Low-frequency Raman spectroscopy was further used to study suspended MoS_2 layers, in order to determine material properties without substrate perturbations, allowing an estimation of strain in suspended bilayer CVD-MoS_2 to be made. These studies also allowed the measurement of resonance effects in the low-frequency region of the WS_2 Raman spectrum.

In summary, reliable growth methods for highly-crystalline TMDs were realised, which were subsequently studied using Raman spectroscopy. This was found to be an ideal technique for the study of TMDs synthesised by different vapour phase methods, and revealed many insights into the behaviour of 2D materials.

Publication Highlights

This section lists some of the results in this thesis that have been published in peer-reviewed journals.

Elements of the work presented in Chapter 3 have appeared in the following publications:

1. O'Brien, M. et al. Plasma assisted synthesis of WS_2 for gas sensing applications. *Chemical Physics Letters* **615**, 6-10 (2014).
2. O'Brien, M. et al. Transition Metal Dichalcogenide Growth via Close Proximity Precursor Supply. *Scientific reports* **4**, 7374 (2014).

Elements of the work presented in Chapter 4 have appeared in the following publication:

1. O’Brien, M. et al. Raman characterization of platinum diselenide thin films. *2D Materials* **3**, 021004 (2016).

Elements of the work presented in Chapter 5 have appeared in the following publications:

1. O'Brien, M. et al. Low wavenumber Raman spectroscopy of highly crystalline $MoSe_2$ grown by chemical vapor deposition. *physica status solidi (b)* **252**, 2385-2389 (2015).
2. O'Brien, M. et al. Mapping of Low-Frequency Raman Modes in CVD-Grown Transition Metal Dichalcogenides: Layer Number, Stacking Orientation and Resonant Effects. *Scientific reports* **6**, 19476 (2016).

List of Abbreviations

- 2D – two dimensional
- AFM – Atomic Force Microscopy
- CVD – Chemical Vapour Deposition
- CVT – Chemical Vapour Transport
- DOS – Density of States
- FET – Field-Effect Transistor
- GGA – Generalised Gradient Approximation
- HAADF - High Angle Annular Dark Field
- HRTEM – High Resolution Transmission Electron Microscopy
- ICP – Inductively Coupled Plasma
- IPA – Isopropanol
- IR – Infrared
- LA – Longitudinal Acoustic
- LBM – Layer-Breathing Mode
- LO – Longitudinal Optical
- LPE – Liquid Phase Exfoliation
- PECS – Precision Etching and Coating System
- PL - Photoluminescence
- PMMA – Poly-Methyl Methacrylate
- QCM – Quartz Crystal Microbalance
- sccm - standard cubic centimetres per minute
- SEM – Scanning Electron Microscopy

- SM – Shear Mode
- STEM – Scanning Transmission Electron Microscopy
- TAC – Thermally Assisted Chalcogenisation
- TEM – Transmission Electron Microscopy
- TMD – Transition Metal Dichalcogenide
- TMO - Transition Metal Oxide
- UHV – Ultra-High Vacuum
- UV – Ultra Violet
- XPS – X-ray Photoelectron Microscopy

Contents

1 Introduction

1.1 Layered Nanomaterials

In 2004, with the isolation of graphene by Geim and Novoselov,[1] research into the field of two dimensional (2D) materials exploded. Graphene is a 2D sheet of carbon atoms, and is the basic building block for graphitic materials of all other dimensionalities, such as fullerenes, nanotubes and bulk graphite, as shown in Figure 1(a). The isolation of graphene made it possible to study its exciting properties, and has led to a burgeoning interest in the isolation of monolayers of other materials with various interesting electrical, optical and physical properties. What these monolayers have in common are weak interplanar van der Waals bonds, meaning they can be sheared away from their nearest neighbouring layer, while retaining strong in-plane anisotropic bonds.[2] The discovery of other 2D materials with a diverse range of properties – for example, hexagonal boron nitride (hBN) as an insulator, molybdenum disulfide (MoS_2) and tungsten disulfide (WS_2) as semiconductors, and tantalum disulfide (TaS_2) and niobium diselenide ($NbSe_2$) as superconductors[3] – means that 2D materials could be suitable for use in a wide range of future applications. For example, stacking these materials to form heterojunctions[3, 4] as shown in Figure 1(b) could lead to ultrathin, high performance devices at the ultimate thickness limit.[5] New materials and designs are constantly being pursued to provide realistic solutions for future electronics, with added functionality, while maintaining the device performance and cost of the current market. Research into 2D materials is currently being pursued worldwide, due to their various properties that make them desirable for industrial adaptation.

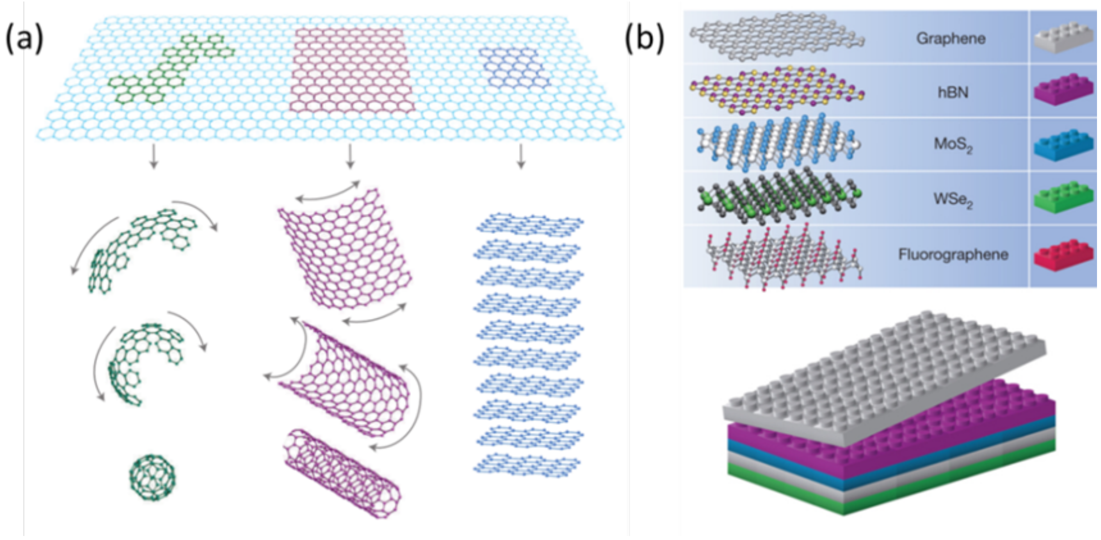

Figure 1

(a) Schematic of graphene as a 2D building block for various carbon nanomaterials.[6] (b) Schematic comparing 2D materials with different electronic properties (semi-metals, semiconductors and insulators) to Lego bricks, showing how a huge variety of devices could be constructed from 2D materials.[3]

In 2010, Mak *et al.*[7] and Splendiani *et al.*[8] showed that MoS_2, which had previously been shown to exist in a few-layer state,[9] showed extraordinary photoluminescence (PL) in its single-layer form. This was demonstrated by optical studies on MoS_2 layers, which had been mechanically exfoliated to obtain few-layer crystals. An example of such mechanically exfoliated layers is shown in Figure 2(a). MoS_2 transforms from an indirect to direct bandgap semiconductor as it thins from bulk to monolayer, as indicated by the band structures in Figure 2(b).[8] This direct bandgap manifests itself in extraordinary room temperature PL, which is attributed to the effect of quantum confinement on the material's electronic structure,[7] and allows fast identification of single layers. The presence of a significant direct bandgap in MoS_2 and other atomically thin transition metal dichalcogenides (TMDs) such as WS_2 indicates that they could be more suitable than graphene for use as active materials for the semiconductor industry, as the zero bandgap in graphene limits its use in practical applications. Direct bandgap materials are also preferred in optoelectronic applications, as light can be more efficiently absorbed, even with thinner active layers. TMDs are generally inorganic materials with a chemical formula of MX_2 where M is a transition metal (*e.g.* Mo, W) and X is a chalcogen (*e.g.* S, Se, Te). The 2D TMDs studied in this thesis have layers consisting of an X-M-X sandwich, as shown in Figure 2(c) and Figure 2(d) for the example of MoS_2.

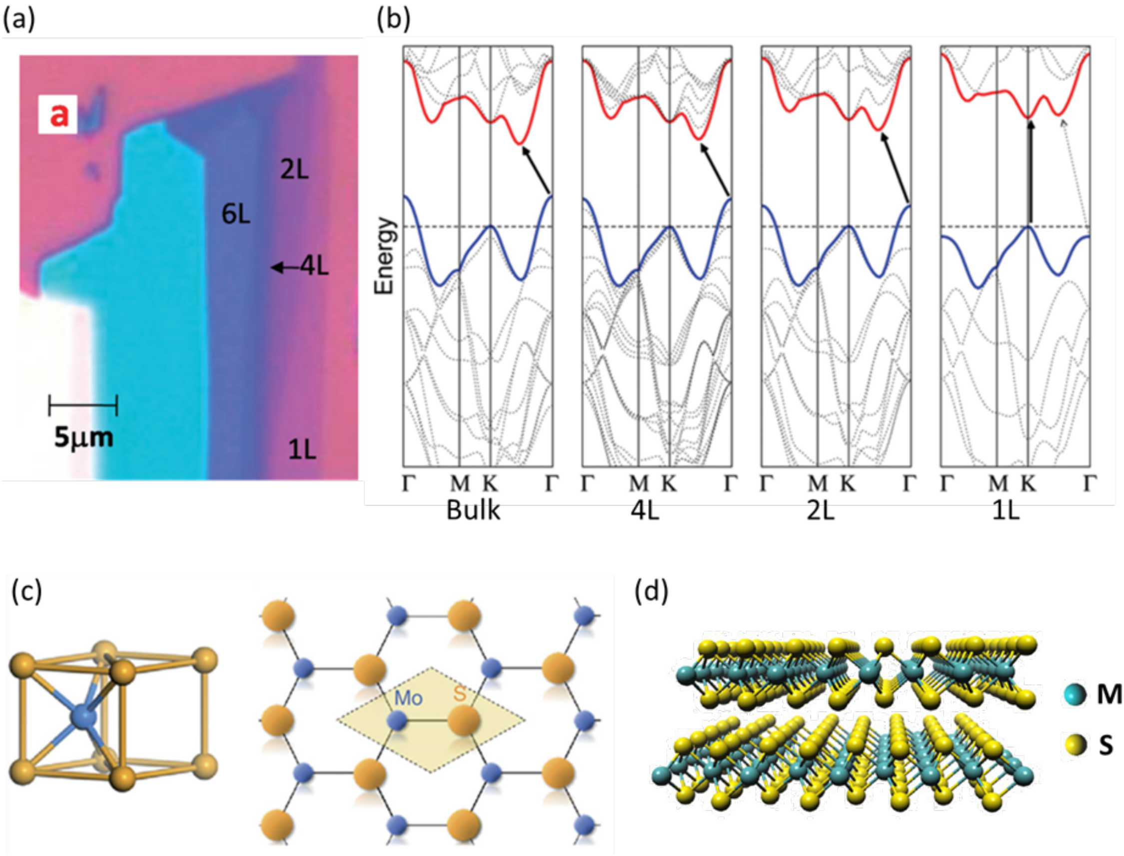

Figure 2

(a) Mechanically exfoliated few-layer MoS_2 flakes.[8] (b) Calculated band structures of MoS_2 as it thins from bulk to monolayer.[8] Schematic of (c) crystal structure[10] and (d) van der Waals stacking of layers in MoS_2.

MoS_2 and WS_2 have thus far been the most heavily studied members of the TMD family, with monolayers of these materials having reported maximum low-temperature mobilities of up to ~34,000 $cm^2\ V^{-1}\ s^{-1}$ and ~500 $cm^2\ V^{-1}\ s^{-1}$, respectively,[11-13] for hBN encapsulated devices. These mobilities, in combination with high on/off ratios of 10^8 and 10^6 for MoS_2 and WS_2, respectively,[11, 12] outline the promise these materials hold for future devices such as field effect transistors (FETs),[11] gas sensors,[14] or in optoelectronics.[11, 15-17] MoS_2 has also been suggested for use in devices such as biosensors, with ultrasensitive and specific protein sensing demonstrated with a sensitivity 74 times better than graphene,[18] and solar cells due to its high visible light absorption.[19, 20] It has been shown that a 1% efficient solar cell based on an MoS_2/graphene stacked vertical heterojunction can deliver a generated power per unit volume ~30 times greater than GaAs.[19] Similarly, efficiencies of up to 1.5% have been demonstrated for WS_2/MoS_2 vertical heterojunctions, with ultrahigh power densities similar to the MoS_2/graphene junction.[19]

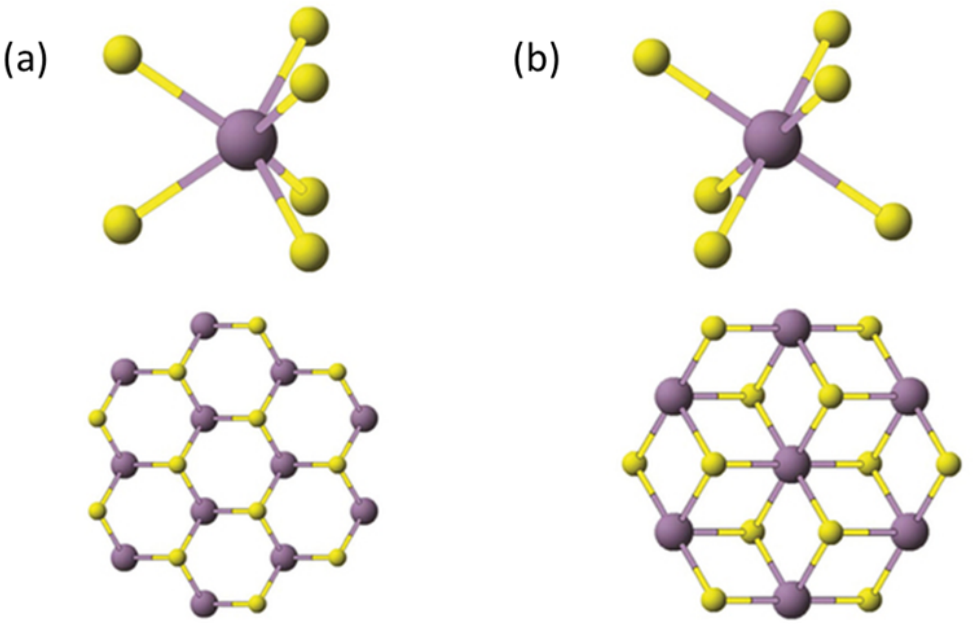

Figure 3

Layered TMDs typically exist in one of two main crystal structures, shown here from side-on and top-down, where chalcogen atoms are in yellow, and metal atoms in purple.[21] (a) The 2H/3R trigonal prismatic crystal structure. (b) The 1T octahedral crystal structure.

MoS_2 and WS_2 are both layered TMDs which exhibit a hexagonal crystal structure when found in nature, which has metal and chalcogen atoms in a trigonal prismatic coordination, as shown in the schematic in Figure 3(a). This can be present as a 2H or 3R polytype, depending on the stacking of chalcogen and metal atoms from layer to layer. However, MoS_2 can be phase-engineered[22] to a different polytype, the less stable 1T crystal. This metallic polytype has proven useful for applications in electronic device contacts[21] which minimise contact resistance to MoS_2, and as supercapacitor electrode materials.[23] The exfoliation and subsequent phase control[21, 22, 24] of MoS_2 by wet chemical methods has been shown to be effective for improving material quality.[21, 22] This phase engineering generally involves harsh chemical treatments, such as lithium ion intercalation, and the MoS_2 relaxes back to its trigonal prismatic coordination with time. However, certain TMDs exist naturally in a 1T crystal structure, such as HfS_2 and $PtSe_2$. These 1T layered materials also exhibit changes in electronic and optical properties with decreasing layer number, in a similar manner to 2H TMDs, and their optical and electronic properties merit further investigation.

1.2 Scope of Thesis

This thesis will investigate the properties of vapour phase synthesised TMDs, with a view towards their future integration into electronic devices. A brief introduction to the relevant background will be given at the start of each chapter to provide the reader with an appropriate context for these results with respect to literature reports. The current chapter serves as a general introduction to 2D materials, and motivation for their study. Chapter 2 will introduce 2D material production methods, and a background on Raman spectroscopy of TMDs. It will also describe the theory behind the experimental techniques used throughout this work. Chapter 3 will describe the synthesis methods developed for TMD layers, thermally assisted chalcogenisation (TAC) and chemical vapour deposition (CVD), and will include specific details of methods used to carry out the experiments described. Chapter 3 will also examine the performance of devices made from these materials. Chapter 4 will describe studies of the Raman spectrum of TAC grown platinum diselenide ($PtSe_2$), a previously little studied 2D TMD. Chapter 5 will examine the Raman spectrum of CVD-grown crystals of MoS_2, $MoSe_2$, WS_2 and WSe_2 in both the high-frequency and low-frequency regions. Chapter 6 will study the Raman spectrum of MoS_2 in more detail, examining the effects of suspending MoS_2 across holes to examine its properties without background or substrate perturbations. Chapter 7 will give a summary of the work contained herein, and offer suggestions for future work to be undertaken in this field.

2 Theory and Background

This chapter serves as background theory to the main production techniques used by researchers to fabricate 2D materials, and more specifically TMDs. It also serves as an introduction to the theory behind the experimental and characterisation techniques used to synthesise and analyse TMDs.

2.1 Synthesis Techniques

2.1.1 Mechanical Exfoliation

Monolayers of MoS_2 and WS_2 were first isolated *via* mechanical exfoliation of flakes from bulk crystals using Scotch tape,[7, 8, 11] which can give crystals of high structural and electronic quality, but of small lateral size. A schematic of a typical method of mechanical exfoliation of 2D crystals is shown in Figure 4. Scotch tape is applied to a bulk crystal of the material, and peeled away carefully, as illustrated in Figure 4(a) and (b). The tape is then applied to a desired deposition substrate, and peeled off slowly, as shown in Figure 4(c) and (d), resulting in a single monolayer left on the desired substrate. Often it may take multiple repetitions of steps (a) to (d) to result in a monolayer of suitable size and quality.

The mechanical exfoliation technique is a low-cost method for fabricating pristine monolayers or few-layers of many different 2D materials for initial studies. The monolayers can be used to test electronic and optical properties, and even material stability in ambient conditions. Efforts have been made to scale up the process of mechanical exfoliation in order to test these materials' suitability for applications in the electronics industry.[25] However, variables such as chemical supplier of bulk flakes and type of adhesive on the tape used can massively affect the resulting size and stability of the exfoliated monolayer, and could contribute to the spread in material properties reported in the literature.[26] Several reports on 2D TMDs use different tapes[1, 11, 27] with different adhesive strengths, such as blue Nitto and Scotch tape. This indicates that the choice of tape and adhesive may be important to consider when exfoliating materials with different interlayer strengths, and may assist in reducing residual organic contamination on the exfoliated layers.

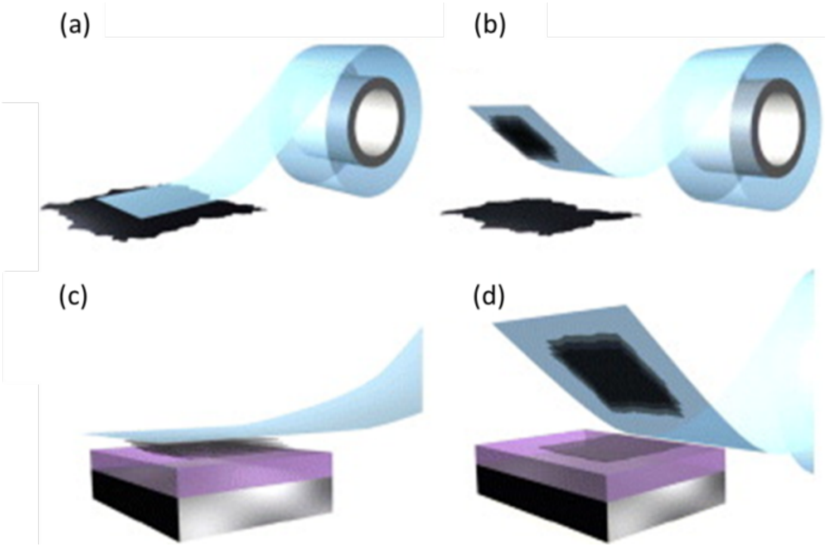

Figure 4

Schematic of mechanical exfoliation of 2D crystals.[28] (a) Scotch tape pressed onto thinned layered crystal, (b) Scotch tape peeled off, bringing multiple atomic layers with it, (c) Multilayers pressed onto desired substrate and (d) Tape peeled off again, leaving a single atomic monolayer behind.

2.1.2 Liquid-Phase Exfoliation

Sonication assisted Liquid-Phase Exfoliation (LPE)[2, 29-31] and shear mixing[32] can be used to produce large amounts of few-layer 2D material sheets, representing a huge scale-up of processing layered materials when compared to mechanical exfoliation methods. A schematic of a typical LPE process using sonication is shown in Figure 5(a). The starting layered material is dispersed into a solvent chosen to minimise the interfacial tension between the dispersed flakes and the solvent in the final solution, so the flakes remain dispersed and do not restack. The mixture is then sonicated, in order to provide energy to separate, or exfoliate, the layers, and finally centrifuged, in order to separate exfoliated flakes from unexfoliated material. Examples of dispersions of exfoliated flakes are shown in Figure 5(b). These few-layer flake dispersions have been shown to be useful for stability, dispersability and fundamental studies of few-layer flakes,[30, 33] as well as photodevice printing,[34] electromechanical sensors,[35] and composites,[36] and have been suggested for a range of future uses in additive manufacturing.

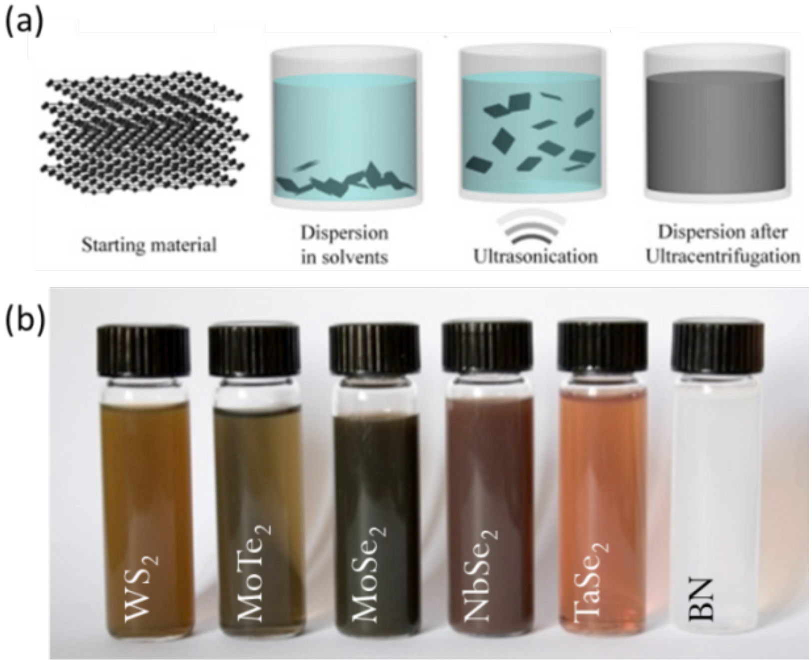

Figure 5
(a) Schematic of LPE of 2D materials from multi-layered crystals.[37] (b) Examples of 2D materials that can be readily dispersed in solution.[29]

Due to the variation in thickness and lateral size of the exfoliated flakes, mobilities measured over printed films consisting of many hundreds or thousands of flakes can often be too low to be considered for high-end electrical devices; this is often attributed to numerous interflake contacts diminishing the electrical performance. Problems can also emerge in the re-aggregation of monolayers into multilayers upon drying, resulting in the loss of desirable monolayer properties. Recent developments have aimed to address these issues, by using cascade centrifugation to enrich the production of monolayer content or to size-select exfoliated flakes.[38] Large-scale, low-cost preparation methods of films with improved crystallinity may be needed for these materials to be considered for industrial adoption for certain applications. Ongoing developments in printing of LPE nanosheets have shown that thin-film transistors with decent mobilities and performances can be manufactured from dispersed flakes.[39] Chemical exfoliation[24] by lithium ion intercalation has also been shown to be a viable method of isolating few-layer MoS_2 flakes, as it can result in higher production rates of monolayers. However, this involves harsh chemical treatments and can result in partial and unstable phase conversion of the lattice to a different crystal structure.[21, 23]

2.1.3 Thermally Assisted Chalcogenisation

One promising method of scaling up TMD film production has been to use TAC of metal films[14, 40-42] to fabricate thin polycrystalline TMD films. Briefly, a thin film of a transition metal or transition metal oxide is deposited on a substrate. This is then annealed in a chalcogen containing atmosphere at high temperatures (typically 400 – 1000 ^oC), until conversion to the corresponding TMD has occurred.[14, 41] The advantages of using techniques such as TAC include the high level of conformity and control in the final material, by controlling the deposition and thickness of the pre-deposited metal film, and also the ease of transfer of large-area films to arbitrary substrates.[42] The material properties can therefore be tuned, from behaving as a bulk film to thin films possessing significant monolayer character, by controlling the thickness of the initial metal or metal oxide film. Samples fabricated from thin metal films typically double in thickness after sulfurisation,[43] and have been shown to more than triple after selenisation,[44] likely due to the increased chalcogen size. It should be noted that those fabricated from thin oxide films do not show a significant increase in thickness.[45, 46] The extent of bulk or monolayer character present can be monitored by examining a property such as PL that is only present in few-layer, highly-crystalline stoichiometric films.[8, 41]

Films can also be pre-patterned by using shadow masking, photolithography, or e-beam lithography to facilitate device fabrication. Devices produced in this way have been used as high-performance gas sensors,[14, 41] photodetectors[42] and catalytically active electrodes for electrochemical hydrogen evolution.[47] Recent reports have demonstrated that the crystallinity of films can be increased through the use of highly-crystalline substrates such as sapphire;[48, 49] however without the use of highly ordered substrates TAC films remain polycrystalline with little long range ordering in the lattice, and therefore face many of the same issues as LPE with regards to industrial adoption. Therefore, while TAC films offer advantages in scalability, uniformity and thickness control of films, a different approach is necessary to fabricate high-quality single crystals on a large scale for future electronic devices.

2.1.4 Chemical Vapour Deposition

CVD is a widely used fabrication technique in materials science and the semiconductor industry. Far from being limited to thin film growth, which will be the focus in this work, CVD can also be used for the fabrication of nanoparticles, nanotubes, and bulk powders. It is formally defined as the formation of a solid film on a substrate by the reaction of vapour phase chemicals that contain the required constituents.[50] These vapour phase chemicals react on the substrate surface to produce the desired material, while by-products are removed from the CVD chamber by gas flow. The vapour phase chemicals can be activated by thermal, plasma or chemical means.[50] The final form of the material deposited relies on a number of parameters, including deposition temperature, pressure, gas flow and the growth substrate. The advantage of CVD over other thin film technologies, such as evaporation, molecular beam epitaxy, sputter coating or electroplating, is the high purity and control over film growth that can be obtained at a relatively economical cost. This has led to the application of CVD for the growth of epitaxial layers on crystalline substrates or films, and metallic, semiconducting and insulating layers in the microelectronics industry. It can also be used in the deposition of coatings of different materials with different protective qualities, such as wear resistant (TiC on cemented carbide cutting tools), decorative coatings (TiN on jewellery) and heat resistant coatings (Al_2O_3). Disadvantages of CVD include the possible by-products that can be formed during reactions, which could be potentially hazardous, or contaminate the final product.[51] Another major disadvantage is that CVD is generally carried out at high temperatures, restricting the substrates on which growth can occur. This could necessitate post-growth transfer of films to other substrates, which can cause damage and degradation.[51] The specific CVD reaction conditions used in this work will be detailed in the CVD film production section in Chapter 3.

Recently there have been significant advances using CVD[52-59] to produce high-quality TMD monolayer single crystals, a general schematic of which has been shown in Figure 6(a).[54] CVD of TMDs typically uses solid precursors, which are evaporated before the reaction and growth take place. This is in contrast to gaseous precursors that are generally used for CVD growth of thin films, and may be responsible for some of the limitations in TMD growth which have recently been realised. The solid precursors are evaporated and carried downstream to the growth substrate in the gaseous phase, where they react and deposit on the substrate. The advantages of CVD as a growth technique include its ability to be used in the fabrication of heterostacks and epitaxial layers, as well as the production of alloys by mixing precursors. Reproducibility and consistency across a single sample of MoS_2 synthesised in this manner remain as issues, as different sizes and densities of crystals have been reported along the length of a growth substrate;[60-65] particularly if a seeding promoter is also required in the reaction, as shown in Figure 6(b).[64] Typically, seeding promotors such as graphene oxides or PTCDA increase the nucleation density and overall coverage of MoS_2, but result in smaller crystallite sizes in the merged monolayer film compared to clean substrates.[63] In addition, many reports of TMD production *via* CVD require excess amounts of oxide precursors, which can result in oxisulfide and other contaminants.[54, 66] This is shown in Figure 6(c), with entirely different MoS_2 formation on different parts of the same substrate.[60, 63] This suggests that a more universal and reproducible approach is necessary that does not rely on the presence of excess oxides or seeding promoters in the growth.

Studies have also highlighted the impact of substrate on the growth of MoS_2. Epitaxial growth of MoS_2 on mica[62] and sapphire[67] has been demonstrated, resulting in controlled lattice orientation and reduced formation of grain boundaries when domains merge to form closed layers. The preferred orientation of MoS_2 triangles on these highly-crystalline surfaces was attributed to an epitaxial growth mechanism, whereby the MoS_2 is intrinsically strained due to lattice mismatch between mica and MoS_2.[62] These epitaxial growth methods can offer large-area, high-quality MoS_2 for a variety of applications in electronics, yet cost of growth substrates may be prohibitive for scaling-up towards industrial adaption. Device manufacture also typically requires transfer from sapphire or mica to SiO_2/Si substrates, which may introduce defects and contaminants into the material.

The most promising MoS_2 growth to date was carried out using metal-organic CVD (MOCVD) in the preparation of wafer-scale homogenous monolayer MoS_2.[53] This experimental setup was designed to combat the previously mentioned limitations of CVD-

MoS_2 growth, and incorporated a low growth rate over a time period of ~ 26 hours with low flow rates of gaseous precursors, including $Mo(CO)_6$ and $(C_2H_5)_2S$. This large-scale growth allowed wafer-scale processing of MoS_2 on diverse substrates, including SiN, HfO_2 and Al_2O_3, with measured mobilities of up to 30 $cm^2\ V^{-1}\ s^{-1}$.[53]

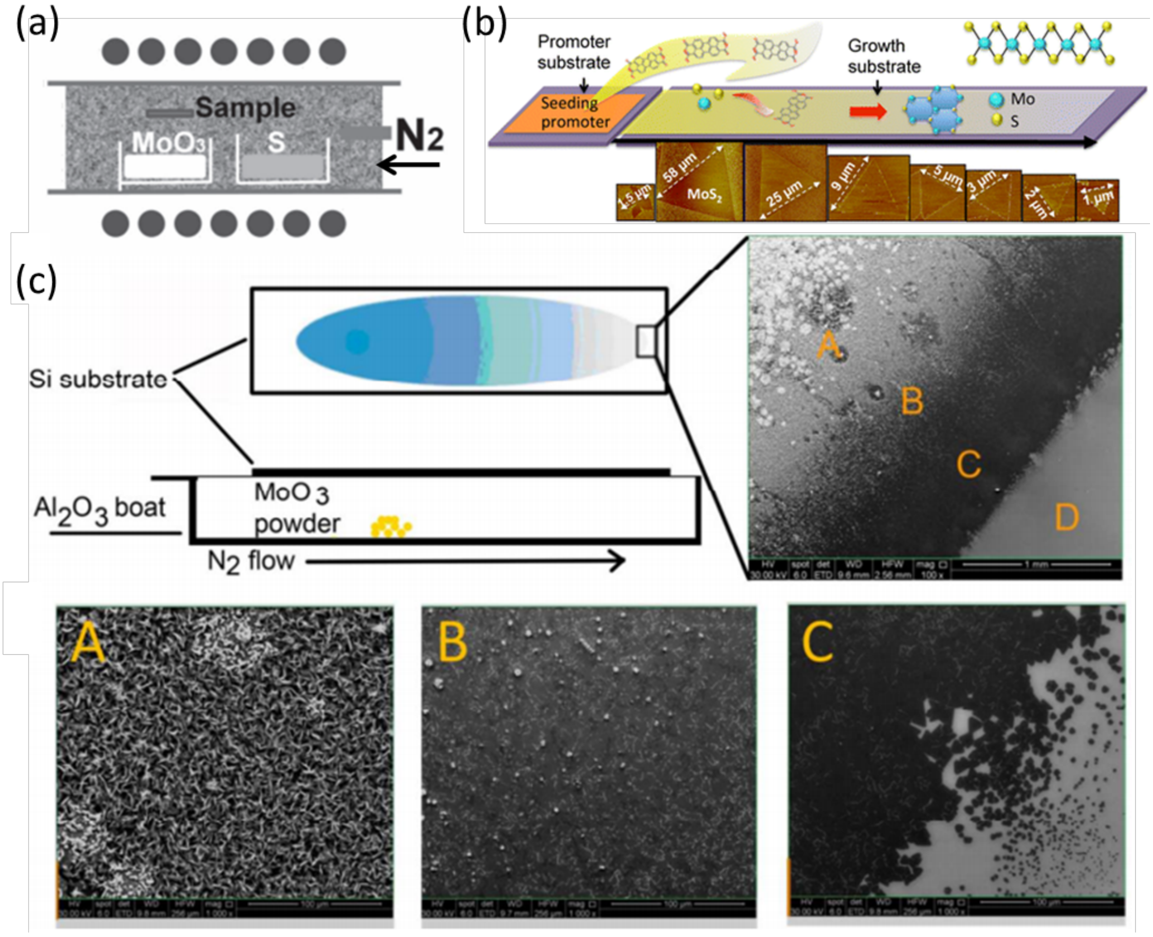

Figure 6
(a) Schematic of typical CVD growth setup, with growth wafers suspended over MoO_3 boat, downstream from evaporated elemental sulfur.[54] (b) Variable growth of MoS_2 single domains as distance from seeding promoter increases. (c) The variation in growth of MoS_2 crystals from bulk-like to monolayer with distance along the wafer.

2.2 Spectroscopic Techniques

2.2.1 Raman Spectroscopy

Raman spectroscopy is a powerful technique in the characterisation of thin films as it is typically non-destructive and structure-sensitive. Raman scattering with monochromatic laser light is widely used in materials science as both a characterisation technique and a tool to probe the fundamental properties of materials. It was discovered by Sir C.V. Raman, for which he was awarded the 1930 Nobel Prize in Physics.[68] When light interacts with a sample, it will be absorbed, reflected, or scattered. Most light is scattered elastically, in what is known as Rayleigh scattering. This type of light scattering is strong, with the same frequency, ω_0, as the incoming beam. The rest of the light is scattered weakly, in a process known as Raman scattering, with frequencies of $\omega_0 \pm \omega_q$, where ω_q is the vibrational frequency of a molecule. The $\omega_0 + \omega_q$ and $\omega_0 - \omega_q$ lines are known as the anti-Stokes and Stokes lines, respectively.[69]

In this thesis, Raman spectroscopy will be primarily used to study molecular vibrations in 2D materials. In the case of graphene, Raman spectroscopy has previously been used to investigate the number and relative orientation of individual atomic layers, and to provide information on defect levels, strain and doping.[70] Recent studies have shown that analogous information can be obtained for TMD samples, with each TMD having a characteristic Raman spectrum. MoS_2 is the most heavily studied TMD to date and numerous reports on its Raman characteristics, and their dependence on layer number, have emerged.[71, 72]

The frequency dependence of Raman scattering can be explained using a classical picture of light scattering from a molecule. The following is adapted from *"Confocal Raman*

Microscopy" by Dieing *et al.*[68] A molecular dipole moment μ, induced by an electric field E can be defined as:

$$\vec{\mu} = \tilde{\alpha}\,\vec{E}$$

where $\boldsymbol{\alpha}$ is the polarisability of the molecule, and describes how much the electric field E can perturb the electron density of the sample out of equilibrium. The electric field can be broken down into its amplitude in the direction of motion E_0 and its oscillation frequency ω_0, described by the following equation:

$$\vec{E} = \overrightarrow{E_0}.\cos\omega_0 t$$

The variables μ and E are vector quantities, and for clarity in the equations, this vector notation will be dropped from now on. The polarisability, $\boldsymbol{\alpha}$, is not a constant, and can be modified by nuclear motion, where the nuclear geometry changes in order to minimise the systems energy at any given stage.[68] This can be described using a Taylor series as follows:

$$\alpha = \alpha(Q) = \alpha_0 + \sum_{q=1}^{N}\left[\left(\frac{\partial\alpha}{\partial q}\right)_{q_0}.q + \frac{1}{2}\left(\frac{\partial^2\alpha}{\partial q\partial q'}\right)_{q_0 q'_0} - q - q' + O(q^3)\right]$$

where the polarisability has been expanded around the equilibrium nuclear geometry, Q_0. Here, Q represents the group of all individual normal modes q. For each normal co-ordinate q, oscillations with frequency ω_q can be excited, described by:

$$q = q_0.\cos(\omega_q t)$$

Combining previous equations gives:

$$\mu(t) = \alpha\,(Q).E = \alpha(Q).E_0\cos(\omega_0 t) = \left[\alpha_0 + \left(\frac{\partial\alpha}{\partial q}\right)_{q_0}.q_0.\cos(\omega_q t)\right]E_0\cos(\omega_0 t)$$

where in the Taylor series, the sum over all normal modes was reduced to a representative mode q and not considered after the first linear term in the series, in an approximation known as the electrical harmonic approximation. Using the following trigonometry formula for cosine products allows this to be written as a sum of 3 terms:

$$\cos A \cos B = \frac{1}{2}(\cos(A+B) + \cos(A-B))$$

Therefore, the previous equation can be modified as follows:

$$\mu(t) \ = \alpha_0 E_0 \cos(\omega_0 t) + \frac{1}{2}\left(\frac{\partial \alpha}{\partial q}\right)_{q_0} . q_0 . E_0 . \cos\left[\left(\omega_0 - \omega_q\right)t\right]$$
$$+ \frac{1}{2}\left(\frac{\partial \alpha}{\partial q}\right)_{q_0} . q_0 . E_0 . \cos\left[\left(\omega_0 + \omega_q\right)t\right]$$

The first term describes the previously mentioned Rayleigh scattering, where the light emitted vibrates at the same frequency as the light that excited the system. Notably, this term does not offer any information about the system under study – this term only involves the incident light on the system. The second term describes Stokes scattering, where light emitted is red-shifted with respect to the excitation light, and vibrates with a frequency equal to the difference between the light source that excited the system and the molecular normal mode frequency. The third term describes Anti-Stokes scattering, where light emitted is blue-shifted with respect to the excitation light, and vibrates with a frequency equal to the sum of the energy of light source that excited the system and the molecular normal mode frequency. This third term is identical to the Stokes scattering, and will be mirrored in position around the Rayleigh scattered light, however it will be much lower in intensity due to the Boltzmann factor that describes the population of thermally excited vibrational states. This results in it being more likely that the system will take energy from the light excitation than the system will give energy to it, as there are less initially excited vibrational states in the system to lose energy to the incident light than there are ground states to accept energy from the incident light.

Therefore, when a line appears on a Raman spectrum indicating the vibrational frequency of a molecule, it is actually showing the shift in vibrational frequency (ω_q) from that of the incident beam (ω_0),[69] as software built into Raman systems generally accounts for the wavelength of the incident laser light used. As the change in frequency of light is dependent on bonds and symmetry in the material, the Raman signals can act as a characteristic fingerprint, and therefore is of interest across many fields of science. A schematic of a Raman spectrum showing the Stokes, Anti-Stokes and Rayleigh scattering is shown in Figure 7(a).

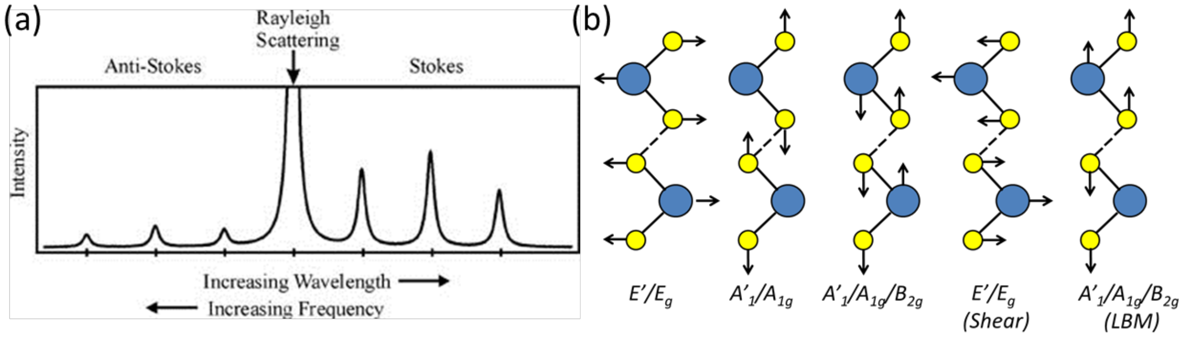

Figure 7
(a) Schematic of Stokes and Anti-Stokes Raman scattering, and their difference in intensities. (b) Various in-plane and out-of-plane Raman-active modes for multilayer MoS_2.

Each Raman-active vibrational mode in a molecule or system will therefore have a corresponding peak on a Raman spectrum, although some will appear more intense than others. Examples of vibrational modes in MoS_2 are shown in Figure 7(b). Certain vibrations are Raman-inactive, but they may be infrared (IR) active. This can be determined by selection rules. In molecules with a centre of symmetry, the principle of mutual exclusion determines that vibrations which are Raman-active are IR-inactive, and vice versa. In this sense, Raman and IR can be considered as complementary techniques, where each observes different vibrational modes. In materials that are more complex or have different symmetry, vibrations may be both Raman and IR active, or neither. As the work in this thesis is concerned with materials with a centre of symmetry, more complex cases will not be considered. Classically, these selection rules can be explained as follows. From the equation for $\mu(t)$, it is clear that the inelastically scattered light depends on the $\left(\frac{\partial \alpha}{\partial q}\right)_{q_0}$ term, which describes the electronic polarisability at the equilibrium position along the qth normal coordinate. Physically, this means that the electronic polarisability must change along the coordinates of the molecule, and must be changing at the equilibrium position, for the vibration to be Raman-active. An example of this is a symmetric stretching vibration in a linear triatomic molecule, as shown in Figure 8(a). As the internuclear distance increases, so does the polarizability, meaning $\left(\frac{\partial \alpha}{\partial q}\right)_{q_0} \neq 0$, and the vibration is Raman-active. The dipole moment also changes, but since the bonds that are stretching are opposite in sign, the result is a constant dipole moment along the normal coordinate, meaning $\left(\frac{\partial \mu}{\partial q}\right)_{q_0} = 0$ and the vibration is IR inactive. For the same molecule, consider anti-symmetric stretching as shown in Figure 8(b). Here, the dipole moment will change sign when the system passes through equilibrium, therefore $\left(\frac{\partial \mu}{\partial q}\right)_{q_0} \neq 0$ and the asymmetric vibration in IR active. However, while the polarisability also changes, these changes are symmetric around the equilibrium position, and therefore $\left(\frac{\partial \alpha}{\partial q}\right)_{q_0} = 0$ and the vibration is Raman inactive.

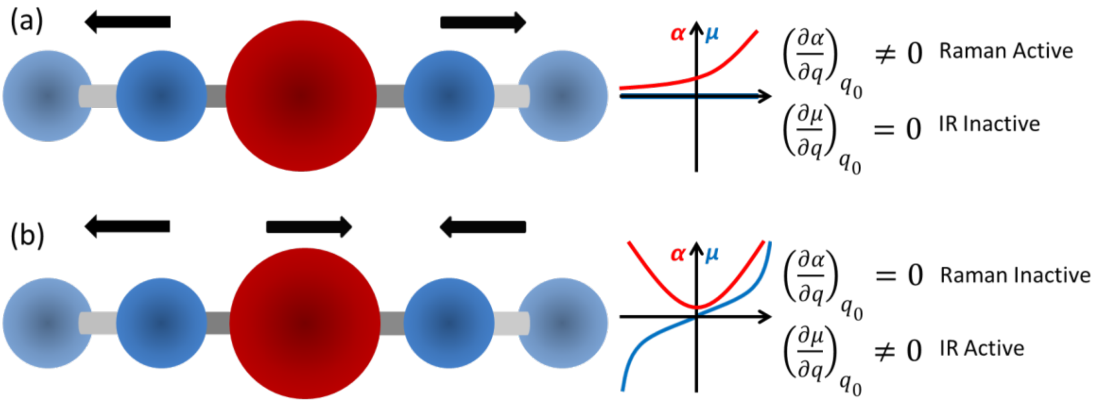

Figure 8
Schematic of vibrations in a triatomic molecule for (a) symmetric stretching and (b) anti-symmetric stretching. Schematic is adapted from Dieing *et al.*[68]

Examples of vibrational modes in MoS_2 are shown in Figure 7(b), where each unique vibration has a characteristic frequency appearing as a peak in a Raman spectrum. These modes can offer a vast amount of information, and are useful for distinguishing between similar molecules. The reason for differing intensity between different peaks in a Raman spectrum can be understood by considering the initial oscillating dipole moment, which for simplicity will be done here for the case of Stokes scattering. Beginning from the derived equation for molecular dipole moment above:

$$\mu^{Stokes}(t) \propto \left(\frac{\partial \alpha}{\partial q}\right)_{q_0} . q_0 . E_0 . \cos\left[\left(\omega_0 - \omega_q\right)t\right]$$

Each of the induced oscillating dipoles acts as an emitter of the secondary oscillations, which is known as a Hertzian dipole. Using a temporal average over the time oscillating part of $|\ddot{\mu}|^2 \propto \cos^2(\omega t)$, the power emitted from this dipole can be expressed as:[68]

$$P = \frac{|\ddot{\mu}|^2}{6\pi . \varepsilon_0 . c^3} = \frac{q_0^2}{12\pi . \varepsilon_0 . c^3} . \left(\frac{\partial \alpha}{\partial q}\right)_{q_0}^2 . \left(\omega_0 - \omega_q\right)^4 . E_0^2$$

Here, ε_0 is the permittivity of free space, and c is the speed of light in a vacuum. As the scattered intensity in a Raman experiment is proportional to the overall power emitted by the dipole moment, the intensity can be expressed as:

$$I_{Stokes} \propto \left(\frac{\partial \alpha}{\partial q}\right)_{q_0}^{2} . \left(\omega_0 - \omega_q\right)^4 . E_0^2$$

This equation shows the relationship between the Raman intensity on both sample and experimental parameters. In order for the mode to appear in the spectrum in the first place, it is clear that the $\left(\frac{\partial \alpha}{\partial q}\right)_{q_0}$ term must be non-zero. This means that $\boldsymbol{\alpha}$, the polarisability, must not be constant and needs to change along the normal mode, and have a non-zero gradient at the equilibrium geometry. Therefore, $\left(\frac{\partial \alpha}{\partial q}\right)_{q_0}$ determines the Raman scattering intensity. It should be noted that the equilibrium polarisability, $\boldsymbol{\alpha}_0$, is considered to be independent of the molecular species, and influences the Rayleigh scattering only. Therefore, $\left(\frac{\partial \alpha}{\partial q}\right)_{q_0}$ and ω_q can give information about the sample being studied, while ω_0 and E_0^2 (the laser frequency and power, respectively) are experimental parameters that influence the final Raman intensities observed. It is clear that an increase of laser power or frequency would lead to more intense Raman scattering. It is evident from the equation for molecular dipole moment, $\mu^{Stokes}(t)$, that the intensity of vibrational modes can be heavily modified by controlled experiments – for example, tuning the laser frequency to maximise the $\left(\frac{\partial \alpha}{\partial q}\right)_{q_0}$ term, resulting in resonant Raman scattering, as is the case in this report for WS_2, shown in Chapter 5 at a green laser wavelength of 532 nm. The sample under study could also be brought into close contact with a metallic surface, increasing the Raman scattering cross section by up to 15 orders of magnitude, due to a combination of field effect enhancement, E_0, and chemical enhancement from surface induced changes of the molecular polarisability, $\boldsymbol{\alpha}_0$.

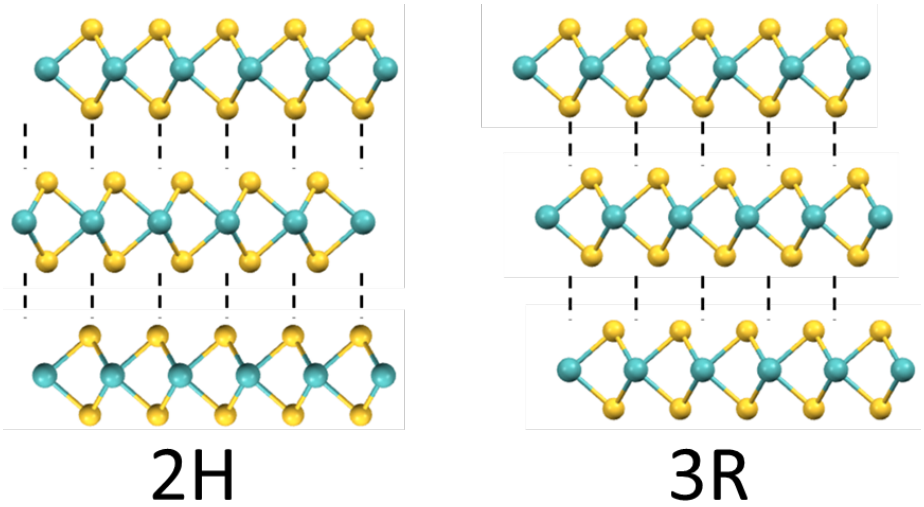

Figure 9
Schematic of 2H and 3R stacking patterns in hexagonal MoS_2.

MoS_2 can exist in a number of polytypes, including 2H, 1T and 3R. The 2H and 3R are trigonal prismatic crystals, with the difference between them being the relative stacking of the layers, while 1T MoS_2 is an octahedral crystal, typically formed *via* harsh chemical treatments.[21, 22, 24] The most common polytype, 2H, will be focused on here for the purpose of explaining the Raman modes used in the typical characterisation of MoS_2. The 3R polytype will be discussed in Chapter 5, and consists of layers of MoS_2 in the same lattice orientation per layer as 2H-MoS_2, but stacked in a different way. This is illustrated in Figure 9. The 2H-MoS_2 Raman spectrum displays two main characteristic Raman-active modes in non-resonant Raman conditions. In the case of bulk 2H-MoS_2, which belongs to the D_{6h} symmetry group, each layer is parallel to the next, with a rotation of $\pi/6$ from the previous layer, for a main rotational axis perpendicular to the parallel layers. The 6-fold symmetry in bulk MoS_2 occurs due to the S/Mo atoms in the layers not mapping onto each other directly, as they do in odd and even-numbered layers. While it is not intuitive that the S/Mo atoms map onto each other 6-fold, it can be visualised as a screw axis transformation. This means that a 60° rotation occurs, followed by a parallel translation along the rotational axis, resulting in the layers mapping onto each other fully. The unit cell consists of 6 atoms, leading to 18 vibrations, decomposing at the Γ point into the following irreducible representations:[72, 73]

$$\Gamma_{2H} = A_{1g} \oplus 2A_{2u} \oplus 2B_{2g} \oplus B_{1u} \oplus E_{1g} \oplus 2E_{1u} \oplus 2E_{2g} \oplus E_{2u}$$

A bilayer 2H-MoS_2 crystal has the same unit cell as the bulk case, with a different point group, as the main rotational axis can rotate 3 times, and not 6 as is the case in bulk. Therefore bilayer 2H-MoS_2 belongs to the D_{3d} point group, leading to less irreducible representations, as follows:[72]

$$\Gamma_{2L}^{MoS_2} = 3A_{1g} \oplus 3A_{2u} \oplus 3E_g \oplus 3E_u$$

All few-layered even numbered layers will have the same modes and terminology as 2L. For the case of monolayer 2H-MoS_2, or more correctly 1H-MoS_2, the unit cell consists of one Mo and two S atoms, in the D_{3h} symmetry. The modes described above for bulk can be described therefore as the following irreducible representation:[72]

$$\Gamma_{1L}^{MoS_2} = A'_1 \oplus E'' \oplus 2A''_2 \oplus 2E'$$

In the case of a monolayer MoS_2 crystal the main peaks generally used for characterisation are the E' peak at ~385 cm^{-1} (E_g in bilayer, E^1_{2g} in bulk), and the A'_1 peak at ~403 cm^{-1} (A_{1g} in bilayer and bulk).[74] These arise from in-plane vibrations of Mo and S atoms, and out-of-plane vibrations of S atoms in different directions only, respectively,[74] as shown previously in Figure 7(b). These peaks have been shown to shift in frequency with layer number,[75] allowing layer numbers to be identified easily and quickly. For example, in the case of MoS_2, as the layer number increases, interlayer van der Waals (vdW) forces suppress atomic vibrations meaning higher force constants are observed.[75] This means that the out-of-plane A'_1/A_{1g} mode becomes blue-shifted at higher layer numbers (~2 cm^{-1} from monolayer to bilayer), as the vibrations of this mode are more strongly affected by vdW forces between the layers. The in-plane $E'/E_g/E^1_{2g}$ mode in contrast shows a red-shift as layer number increases (~2 cm^{-1} from monolayer to bilayer). This is attributed to structural changes in the material or to an increase in long-range Coulombic interlayer interactions affecting the atomic vibrations.[74, 75] Additional modes can be observed in the low-frequency (<50 cm^{-1}) region of the Raman spectrum of TMDs, known as the shear modes (SMs) and layer-breathing modes (LBMs), e.g. the E^2_{2g} vibrational SM, as illustrated in Figure 7. These low-frequency vibrations occur due to relative motions of the planes themselves, either perpendicular or parallel to the atomically thin sheets, and can prove useful in the characterisation of 2D materials.

The Raman spectrum of TMDs can be influenced by a number of factors, and therefore is useful in studying a number of effects, including those of temperature, doping, disorder and strain.[76] For example, the $E'/E_g/E^1_{2g}$ mode in MoS_2 has previously been observed to split under strain, due to the isotropic in-plane symmetry breaking.[77] These modes have also been reported to blue-shift to higher wavenumbers with decreasing temperature,[78] which is attributed to thermal expansion causing the equilibrium positions of atoms to change. This in turn causes modification of the interatomic forces, leading to the observed shift in Raman peak position.[79] Doping of MoS_2 films can also affect its Raman spectrum. MoS_2 p-doped by selective Au nanoparticle decoration has been reported to show a blue-shift and increase in intensity in the A'_1/A_{1g} mode,[80] while n-doping results in a red-shift, broadening, and decrease in intensity in the A'_1/A_{1g} mode.[81] This has been attributed to strong electron-phonon coupling of the A'_1/A_{1g} mode, and has led to suggestions that the A'_1/A_{1g} mode may be useful in studying doping levels in 2D materials.[81] The effect of disorder on the MoS_2 spectrum has also been studied, by examining the effect of defects induced by ion bombardment.[82] Several defect-induced peaks can be observed in MoS_2, in particular the $LA(M)$ peak which was found to be proportional in intensity to the level of defects present in the lattice. The $E'/E_g/E^1_{2g}$ mode was also found to red-shift to lower wavenumbers with increasing defect levels, while the A'_1/A_{1g} mode blue-shifts to higher wavenumbers. Both peaks also broaden significantly with increasing disorder.[82]

The WS_2 Raman spectrum is similarly characterised *via* the first-order modes at the Brillouin zone (BZ) centre. These are the in-plane phonon mode E^1_{2g}, and the out-of-plane phonon mode A_{1g}, analogous to those described previously for MoS_2.[58] The spectra presented in this report were taken with a 532 nm excitation wavelength, which is close to resonance with the B exciton absorption peak for WS_2.[83] This gives rise to various resonant modes in the WS_2 Raman spectrum, including the $2LA(M)$ peak, which is the strongest second order Raman resonance of the longitudinal acoustic (LA) mode at the M point, and overlaps in position with the E^1_{2g} vibration. The ratio of $2LA(M)+ E^1_{2g}$ to A_{1g} has been shown to be indicative of layer number in WS_2,[58] which can be confirmed by the emergence of PL as decreasing layer number approaches monolayer, in an analogous way to MoS_2.

Raman spectroscopy was performed in this report, unless otherwise specified, using a Witec alpha 300R with a 532 nm excitation laser with a spectral grating of 1800 lines/mm and a 100× microscope objective (0.95 N.A., spot size ~0.3 μm). A laser power of <1 mW was used in order to minimise sample damage and/or heating. In Chapter 4, red laser Raman measurements were taken using a Witec alpha 300R with a 633 nm excitation laser, with a spectral grating of 1800 lines/mm and a 100× microscope objective (0.95 N.A., spot size ~0.3 μm). Blue laser and polarised Raman measurements were recorded using a confocal Renishaw InVia System microscope, with a 488 nm laser and a 100× microscope objective (0.7 NA, spot size ~0.7 μm). Further specifics on the Raman spectra of TMDs will be described in the experimental Raman chapters.

2.2.2 Photoluminescence Spectroscopy

Luminescence is a phenomenon that involves the absorption of energy by a material, followed by the emission of light. PL is where this energy is supplied by the absorption of photons. In semiconductor research, a typical PL measurement involves the material being excited with a laser light of higher energy than its bandgap. The photons from the laser are absorbed into the material, and form electrons and holes in the conduction and valence bands, as illustrated in Figure 10(a). Following absorption, the electrons and holes undergo energy and momentum relaxation towards the conduction and valence band minima respectively and eventually recombine and emit photons at the energy of the semiconductor bandgap.

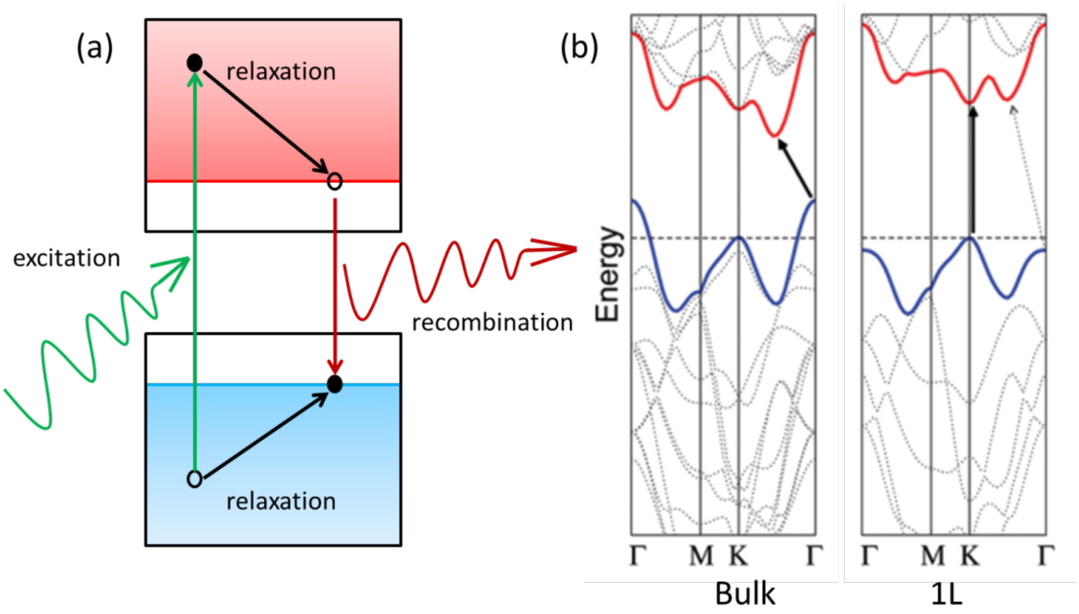

Figure 10
(a) Schematic diagram of a typical PL process in semiconductors (b) Band diagrams of bulk and 1L MoS_2 with arrows indicting bandgap in each case.[8]

It has been reported that the intensity of PL in layered TMDs like MoS_2 and WS_2 increases dramatically with decreasing layer number and that luminescence from a monolayer is the most prominent, while being absent in bulk material.[8, 57] This is because in bulk material, electronic states near the Γ point of the BZ and the point of the indirect bandgap (as shown in the calculated band diagrams in Figure 2(b) previously) come from a linear combination of d-orbitals on the transition metal atoms and anti-bonding p_z-orbitals on sulfur atoms. These states involved in the indirect transition therefore have a strong interlayer coupling, and depend significantly on the number of layers present. However, conduction band states at the BZ K-point are a combination of localised d-orbitals on molybdenum atoms, which have an intrinsic absence of interlayer coupling due to their location in the middle of the layer. This means that for mono- and few-layer MoS_2, enhanced absorption and PL bands at a direct bandgap of ~1.8 eV, as opposed to an indirect bandgap of ~1.3 eV in the bulk,[7, 8] can be observed, since recombination occurs at the K point for the reasons discussed. This results in two resonances that have been well established to be direct excitonic transitions, known as the A1 and B1 excitons,[8] found at ~1.85 and 1.98 eV, respectively. In the case of WS_2, the bulk material shows two direct transitions at the BZ K point due to the splitting of the valence band, allowing two transitions known as the A and B excitons, at ~ 1.95 eV and 2.36 eV respectively.[84, 85] This splitting, however, disappears in the case of a monolayer crystal;[57] meaning only one direct electronic transition and one PL peak is present. Due to its dependence on layer number and crystallinity, PL can be a valuable tool for characterisation and examination of 2D TMD materials. In this work, PL measurements were performed using a Witec alpha 300R with a 532 nm excitation laser, a 100× microscope objective (0.95 N.A., spot size ~0.3 μm) and a laser power of <1 mW, in order to minimise sample damage.

2.2.3 X-ray Photoelectron Spectroscopy

X-ray Photoelectron Spectroscopy (XPS) is a surface sensitive core level spectroscopy technique that uses the photoelectric effect,[86] illustrated in Figure 11, to analyse the properties of a material. The photoelectric effect is the emission of electrons from a sample after illumination by light or photons which exceed a given threshold energy. The energy of these emitted electrons is given by the difference in energy between the incident photons and the work function or binding energy of the material. Therefore, by using a monochromatic source to keep the energy of incoming photons constant, the work function of the material can be measured by analysing the kinetic energy distribution of the electrons emitted, according to the following equation:[87]

$$E_b = \hbar\omega_i - (E_k + \phi)$$

Here, E_b is the electron's binding energy, $\hbar\omega_i$ is the energy of the incident X-ray, E_k is the photoelectron's kinetic energy after emission, and ϕ is the workfunction of the spectrometer. In XPS, X-rays of known energy are absorbed by the first few nanometres of the sample's surface, causing electrons to be emitted. As E_b changes for different elements, it can be used as a characteristic tool to determine the exact composition of the elements, and their bonding configurations, present in a sample. The emitted electrons are from the top 1-2 nm of the material, as any electrons from atoms below this depth experience inelastic collisions with other electrons or atoms, preventing their escape. Due to this surface sensitivity, it is ideal for use in analysis of 2D materials and thin films. XPS can be used to identify the chemical composition of a material, as well as the oxidation states of its component elements and what chemical bonds they form. XPS was used in this thesis to serve as verification of chemical purity in synthesised materials.

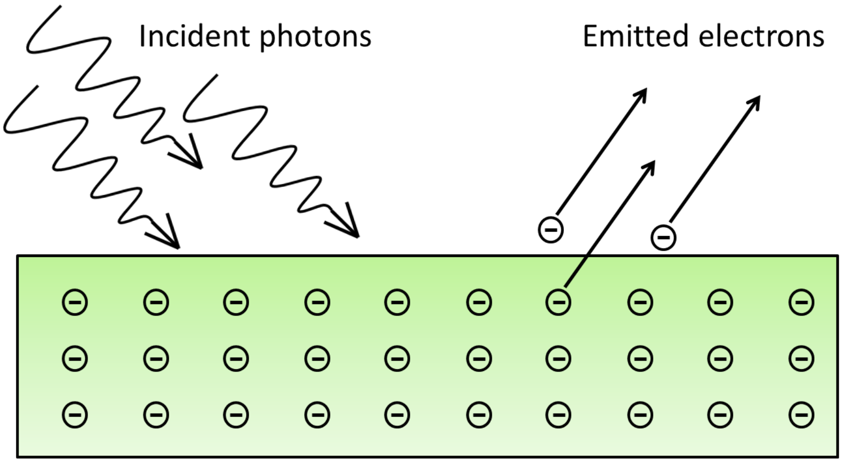

Figure 11

Schematic of the photoelectric effect.

XPS was performed in two different systems in this thesis. For the work concerning WS_2 synthesised with plasma assisted processing, XPS was performed by Dr. Rachel Morrish of the Colorado School of Mines, using a VG Scientific Escalab MKII system under ultra-high vacuum conditions using an Al Kα X-ray source (1486.7 eV). For all other samples, XPS was performed by Dr. Nina C. Berner in Trinity College Dublin. Spectra were acquired under ultra-high vacuum conditions ($<5 \times 10^{-10}$ mbar), using a monochromated Omicron XM1000 MkII Al Kα X-ray (1486.6 eV) source and an Omicron EA125 energy analyser.

2.3 Microscopic Techniques

2.3.1 Atomic Force Microscopy

Atomic Force Microscopy (AFM) is a type of scanning probe microscopy commonly used in nanoscience. It acquires images by rastering a sharp tip attached to a flexible cantilever across the surface of a specimen, which is then deflected by the forces between the surface and the sharp tip. The amount of deflection is measured by using a laser spot focused on the top surface of the cantilever that is reflected onto an array of photodiodes. AFM is used in this thesis in phase (tapping) mode. Phase mode monitors the difference in phase before and after the cantilever interacts with the sample.It can be used to highlight changes in the properties of a material across its surface, including adhesion and friction. Phase images can be measured simultaneously with topographic images, allowing direct comparisions to be made between the two measurement types. Phase imaging typically shows high lateral resolution in samples of different material properties, while topographic imaging shows variation in height across a sample. Used together, these measurements can give a wealth of information regarding 2D materials, and can serve as confirmation of layer number of 2D TMDs measured by Raman and PL. AFM measurements presented in this work were carried out using a Veeco Dimension 3100 in tapping mode, with 40 N/m probes from Budget Sensors with a tip radius of < 10 nm and a resonant frequency of 300 kHz. Measurements in this work were taken with the assistance of Dr. Toby Hallam.

2.3.2 Transmission Electron Microscopy

Transmission Electron Microscopy (TEM) is a microscopic technique whereby a beam of electrons interacts with and passes through a specimen, and is elastically or inelastically scattered in the process. Apertures and detectors are used in order to collect a certain fraction of scattered electrons, allowing an image to be formed of the specimen being examined.

TEM is commonly used as a characterisation tool for 2D materials,[2, 29, 88] due to its ability to image nanomaterials down to atomic resolution, and provide information about long-range crystallinity through the analysis of electron diffraction patterns. TEM can give other useful information on nanomaterials, including shape, composition, crystal structure and level of defects. Some difficulties in TEM can include the small sampling size possible at a given time, electron beam damage to the sample, the possible misinterpretation of images, and image distortion due to aberrations. Aberrations in TEM can limit the resolution that is obtainable, and can cause points to appear blurry on an imaged object. Aberrations can be spherical, meaning they arise due to the lens geometry, or chromatic, meaning they arise due to the inability of the lens to focus electrons of different energies to the same focal plane. Recent advances in microscopy have led to the development of aberration correctors, which can be incorporated into TEM hardware, allowing higher resolution limits to be achieved.[89] Aberration effects are negated by using correctors that produce negative spherical aberration, reversing the spherical aberrations caused by the lens, and by using electron sources with minimal energy spread, in order to refract all beams and focus them to the same focal plane, reducing chromatic aberration effects.

A microscope is generally operated in two principal modes - parallel beam or convergent beam, as illustrated in Figure 12. Parallel beam mode allows the acquisition of High Resolution TEM (HRTEM) images. HRTEM analysis was performed in an FEI Titan transmission electron microscope at an acceleration voltage of 300 kV. Convergent beam mode allows Scanning TEM (STEM) images to be recorded, where a focused beam of electrons is rastered across a sample to generate an image of it. Atomic-resolution images in Chapter 4 on $PtSe_2$ were obtained by collaborators in the University of Vienna, with a Nion UltraSTEM 100, using a high angle annular dark field (HAADF) detector, operated at 60 kV. Where images were taken by collaborators, this will be clearly stated.

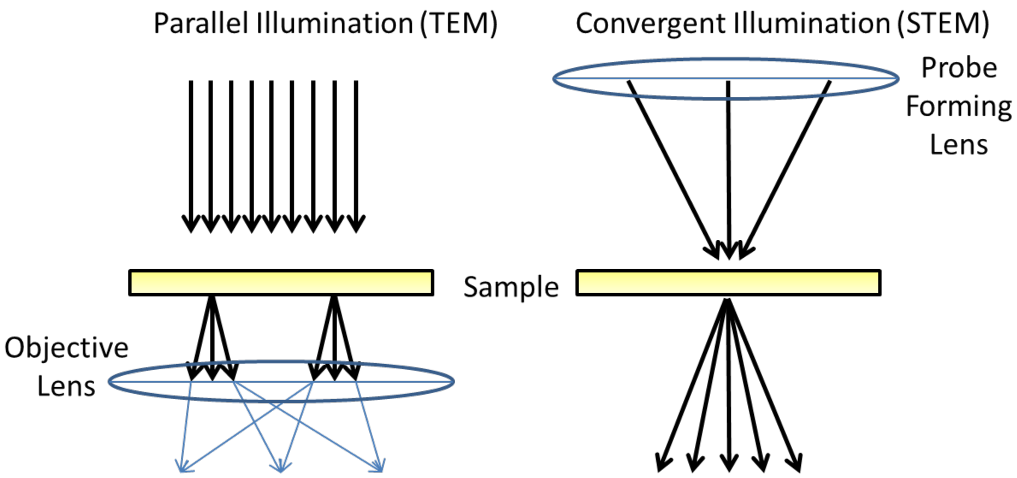

Figure 12
Schematic of a TEM, outlining the principles of parallel and convergent operating modes.

2.3.3 Scanning Electron Microscopy

Scanning electron microscopy (SEM) is a microscopic technique whereby a beam of electrons rasters over a sample, causing multiple interactions to occur. A schematic of an SEM is shown in Figure 13. A schematic is also shown in Figure 13 of the various interactions that arise due to electron beam interaction with the sample, including backscattered electrons, secondary electron and Auger electron emission, and X-Ray emission. The different interactions are then analysed by detectors in the SEM. Backscattered electrons are those which are produced by the scattering of the incident electrons in the sample, and can be used to provide information on the chemical composition of a material by the contrast in the SEM image. Secondary electrons originate from the surface or a few nm into the sample. This means that secondary electron detection, using an InLens detector, can highlight topographical features. When analysing topographical features, low voltages are used in order to only image the surface features. In the results presented in this work, SEM was used to examine the uniformity and topography of synthesised materials. SEM images were acquired using a Zeiss Ultra Plus

SEM and an InLens detector at a low accelerating voltage of 1 kV, in order to increase sensitivity to surface features.

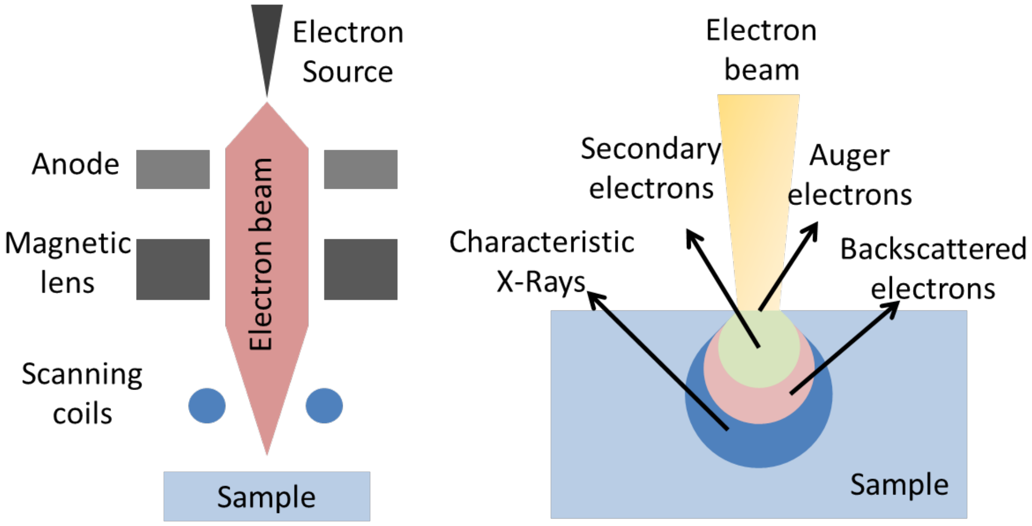

Figure 13
Schematics of an SEM and its electron beam interaction with a sample.

3 Vapour Phase Synthesis of Transition Metal Dichalcogenides

This chapter serves to provide specific experimental details on how the materials studied in the following chapters were produced. Some of the results presented in this chapter were published in the journals "*Scientific Reports*"[90] and "*Chemical Physics Letters*".[91]

3.1 Thermally Assisted Chalcogenisation of Pre-Deposited Films

As mentioned in Chapter 2, large-scale, high-quality TMD films are of interest for both fundamental research and for incorporation into industrial processes. TAC, as introduced previously, offers a method of achieving large-scale uniformity in TMD thin films. A TAC method described previously[14, 42] was used to synthesise MoS_2 films of different thicknesses. Mo films of varying thickness were deposited on SiO_2/Si substrates using a Gatan Precision Etching and Coating System (PECS), where the Mo film deposition rate and thickness were monitored with a Quartz Crystal Microbalance (QCM). The sputtered films were placed in quartz tube furnaces in a zone which was heated to 750 ^{o}C and annealed for 30 minutes at a pressure of ~1 Torr under an argon (Ar) flow of 150 sccm (standard cubic centimetres per minute). Sulfur powder was heated to its melting point (113 ^{o}C) in the inlet zone of the furnace, upstream of the Mo samples, and the generated sulfur vapour was supplied to the Mo films, where it reacted to produce MoS_2. A schematic of this is shown in Figure 14.

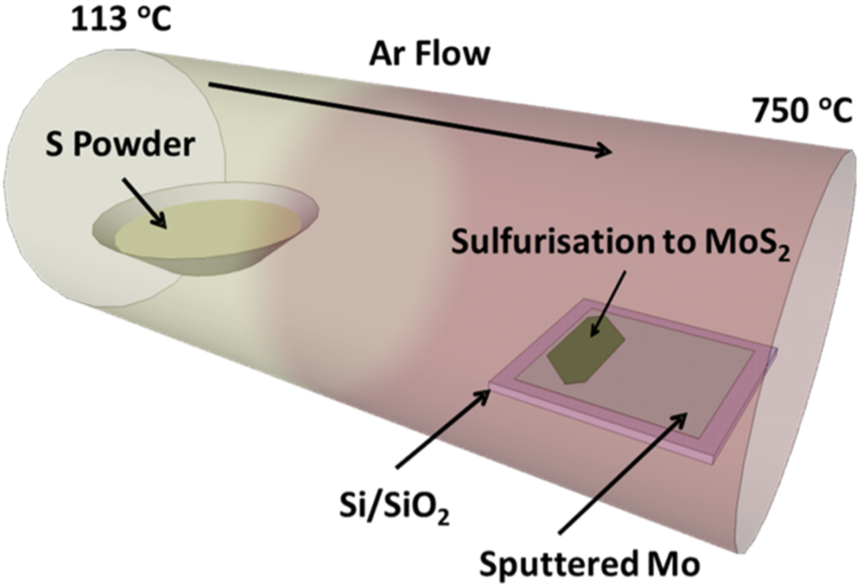

Figure 14
A schematic of the TAC growth process.

This technique yielded a continuous multilayer of MoS_2, with thicknesses verified by Dr. Chanyoung Yim using spectroscopic ellipsometry.[42, 92] Average Raman spectra of the different MoS_2 thicknesses are shown in Figure 15(a), where the E^1_{2g} and A_{1g} peaks are labelled, corresponding to the in-plane and out-of-plane vibrational Raman modes of MoS_2, respectively as discussed in Chapter 2. The separation of the E^1_{2g} and A_{1g} peaks is uniform in the thicker films, with a magnitude of ~25 cm^{-1} that corresponds to previously reported literature values for bulk MoS_2. A slight blue-shift is observable in the E^1_{2g} peak for the thinnest film. This indicates a deviation from bulk behaviour, and the presence of few-layer crystals. The broadening of the peaks indicates the films are more disordered than pristine mechanically exfoliated MoS_2, suggesting that they are polycrystalline in nature.[93] The intensity ratio of A_{1g}/E^1_{2g} indicates the presence of a multilayer film.[71] Using a polymer supported transfer technique the as-grown films could then be transferred onto a variety of substrates, such as pre-defined diode substrates for electrical characterisation,[42] or onto TEM grids for further analysis, as shown in the schematic in Figure 15(b). TEM and diffraction patterns were recorded with the assistance of Mr. Clive Downing in the

Advanced Microscopy Laboratory in Trinity College. A HRTEM image of a representative MoS_2 film transferred onto a TEM grid is presented in Figure 15(c). This confirmed the presence of a polycrystalline film with small average crystal sizes, with certain areas showing hexagonal lattice characteristics as expected for MoS_2. A diffraction pattern shown in Figure 15(d) confirmed the polycrystalline nature of the films, with crystalline domains arranged randomly with respect to each other. This is evident from the rings present in the pattern, instead of spots that would be present for single crystals.

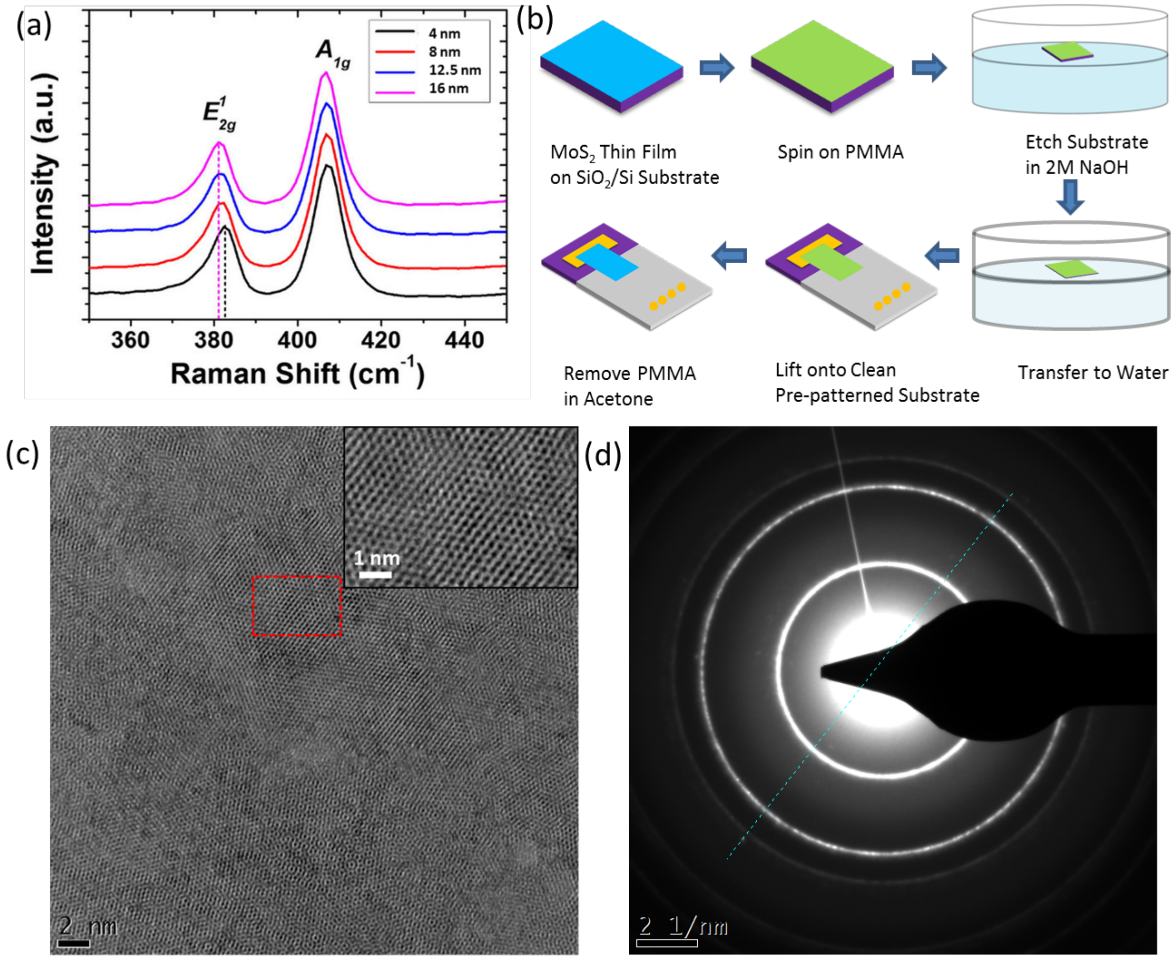

Figure 15
(a) Average Raman spectra of varying thicknesses of MoS_2.[42] (b) Schematic of the wet transfer process for TMD films. (c) HRTEM image of an 8.26 nm thick polycrystalline MoS_2 film. Inset shows highly ordered hexagonal lattice of MoS_2. (d) Diffraction pattern of 8.26 nm film.

While high temperature TAC of metals creates large area uniform TMDs, TAC of metal oxide[46] films has also been suggested as a route towards the manufacture of wafer-scale 2D materials. This has been proposed to increase the crystallinity and performance of the final material synthesised[59] and to allow sulfurisation of thicker films without the significantly higher temperatures required to overcome kinetic limitations.[94, 95] Between transition metal oxides (TMOs) and transition metal sulfides, there is a low difference in densities and specific volumes of the materials[45] leading to a lower expected degree of expansion in the synthesised film.[96]

In collaboration with Dr. Rachel Morrish in the group of Prof. Colin Wolden in School of Mines, Colorado, plasma-assisted chalcogenisation of TMOs was shown to be possible at temperatures as low as 500 °C using plasma-assisted processing with a H_2S/Ar gas mixture.[91, 96] A schematic of this process is shown in Figure 16(a). Briefly, tungsten oxide (WO_3) films were sputtered from a MaTeck WO_3 sputter target using a Gatan PECS onto 15 mm × 15 mm p-type silicon (Si) substrates with 300 nm dry thermal silicon dioxide (SiO_2). Metal shadow masks were used to define the selective channel area, and the thickness of the films deposited was monitored by a QCM. The sputtered films were exposed to an atmosphere whereby an Inductively Coupled Plasma (ICP) was used to activate a mixture of H_2S/Ar (10:90 %). The plasma was generated in a 1 inch quartz tube using a copper coil attached to a 13.56 MHz power supply and associated match network, with an rf power of 80 W applied. An exposure time of 60 min at a temperature of 500 °C was used to convert the WO_3 to WS_2. The sulfurised films were contacted by sputtering Ti/Au (20/80 nm) contacts with a Gatan PECS using a metal shadow mask to define the electrode area. An optical image of the devices is shown in Figure 16(e), where the changing colour of the films with thickness can be seen.

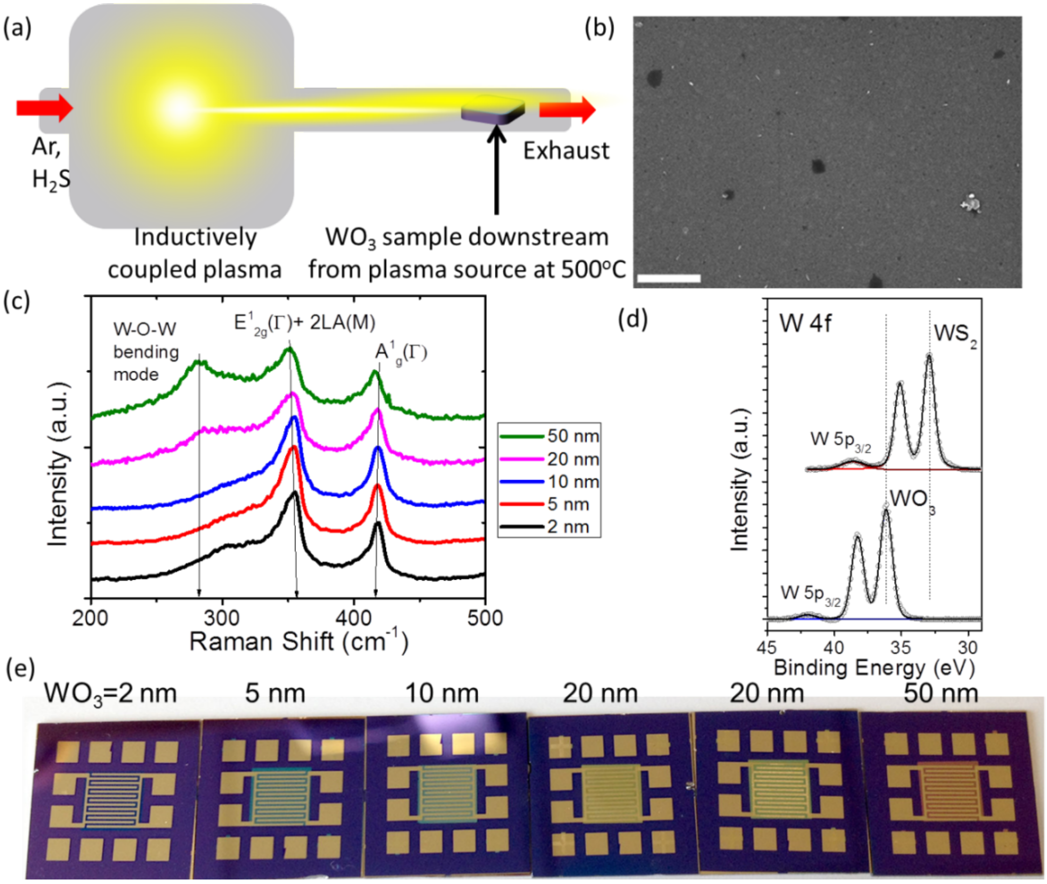

Figure 16
(a) Schematic of furnace used for plasma-assisted chalcogenisation of WO_3. (b) SEM image of 2 nm sample. Scale bar is 1 μm. (c) Raman spectra of each WS_2 film. (d) XPS spectra of 20 nm sample before and after sulfurisation fitted with W 4f spectra. (e) Optical image of contacted devices of varying thicknesses.

SEM images of the films, as shown in a representative image in Figure 16(b), indicated a high degree of uniformity, which was consistent across the entire surface of the sulfurised film. Characteristic WS_2 peaks are seen in the Raman spectra shown in Figure 16(c). The 417 cm^{-1} peak corresponds to the out-of-plane phonon mode, A_{1g}, while the 353 cm^{-1} peak corresponds to a combination of the in-plane phonon mode, $E^{1}_{2g}(\Gamma)$ and the *2LA(M)* peak, which is the strongest second order Raman resonance of the longitudinal acoustic mode at the M point. The Raman spectrum of WS_2 will be discussed in further detail in Section 3.4, where the changes with layer number are more sensitive and clear. The spectra shown here indicate the successful conversion of WO_3 in to WS_2. However, as the films get thicker, a peak emerges below 300 cm^{-1}. This can be assigned to the W-O-W bending mode,[97] which could be due to residual unconverted oxides or a slight reoxidation of the films. It is probable that higher temperatures and/or longer sulfurisation times could be used to fully sulfurise thicker films.

XPS spectra of the 20 nm sample before and after plasma-assisted sulfurisation, taken by Dr. Nina Berner and Dr. Rachel Morrish, are shown in Figure 16(d). The W 4f core-level spectrum for pristine WO_3 shows no component other than the W $4f_{7/2}$ and W $4f_{5/2}$ doublet associated with WO_3. The binding energy values found are in close agreement with values from literature for tungsten (VI) trioxide, where W is in an oxidation state of W^{6+}.[98, 99] This confirms the purity of the deposited films as there is no bonding of W to other elements. The spectra acquired after plasma-assisted sulfurisation show one (detectable) component in the W 4f spectrum, meaning all the tungsten on the surface is sulfurised, with no oxide observed in the W region. The positions of the W $5p_{3/2}$, W $4f_{7/2}$ and W $4f_{5/2}$ peaks are consistent with previous reports in literature of tungsten in an oxidation state of W^{4+}, as is the case for WS_2.[99, 100]

Chalcogenisation of metal or metal oxide films can offer a route towards the manufacture of TMDs in combinations not readily accessible by mechanical or liquid-phase exfoliation due to material availability limitations, or by CVD due to complicated chemical precursor requirements. TAC remains a useful synthesis technique, and has potential applications in areas where high crystallinity is not a limiting factor, such as catalysis or in electrochemical cells. However, the fact remains that films produced using these methods are typically polycrystalline which will limit their electrical performance and in turn their potential use in high-end device applications. As discussed in the following section, true “bottom-up” chemical vapour phase synthesis methods can be used to grow single crystals on large scales with a high degree of order and crystallinity in the lattice.

3.2 Chemical Vapour Deposition of TMDs in a Two Zone Furnace

CVD of MoS_2 was initially carried out by adapting a method previously described in the literature.[54] The setup used is shown in the schematic in Figure 17(d). Briefly, blank SiO_2 substrates were placed facedown above a ceramic boat containing ~1 mg MoO_3 powder and placed in the centre of the hot zone of a quartz tube furnace. The furnace was then ramped to 650 °C under 150 sccm Ar flow. At 650 °C, sulfur was evaporated and carried downstream by Ar gas for 15 minutes, after which the furnace was cooled to room temperature. For the growth of MoS_2, the reaction mechanism has been proposed to be the following stepwise reaction:[101, 102]

$$MoO_3 + \frac{x}{2}S \rightarrow MoO_{3-x} + \frac{x}{2}SO_2$$

$$MoO_{3-x} + \left(\frac{7-x}{2}\right)SO_2 \rightarrow MoS_2 + \left(\frac{3-x}{2}\right)SO_2$$

The sulfur acts as a reducing agent to form a volatile MoO_{3-x} oxide,[103] before further reaction with sulfur vapour to produce MoS_2. For a value of $x = 1$, the reaction therefore proceeds as follows:[102]

$$MoO_3 + \frac{1}{2}S \rightarrow MoO_2 + \frac{1}{2}SO_2$$

$$MoO_2 + 3S \rightarrow MoS_2 + SO_2$$

where MoO_2 is an intermediate phase formed during the reaction.[54] Sulfur dioxide (SO_2) gas is present as a by-product in the reaction and is carried downstream by an inert carrier gas after formation. Due to the formation of volatile MoO_{3-x} oxides,[103] such as MoO_2, it is possible that undesired oxisulfide side products may be formed. Possible suggested reaction mechanisms for the production of oxisulfides are as follows. Beginning from MoO_2:

$$MoO_2 + (y - x)S \rightarrow MoO_{2x}S_{y-1} + (1 - x)SO_2$$

For example, for y = 3 and x = 0.5, these become:

$$MoO_2 + \frac{5}{2}S \rightarrow MoOS_2 + \frac{1}{2}SO_2$$

Beginning from MoO_3:

$$MoO_3 + (x + y)S \rightarrow MoO_{3-2x}S_y + xSO_2$$

For example, for y = 2 and x = 1, these become:

$$MoO_3 + 3S \rightarrow MoOS_2 + SO_2$$

Other various stoichiometries of oxisulfide contaminants may occur during the CVD reaction, however these were not studied in detail in this work.

MoS_2 single crystal domains were formed, as shown in Figure 17(a), which could quickly be identified by their characteristic triangular shape, which reflects the internal lattice orientation.[63, 104] Raman maps taken over the area of the red box in Figure 17(a), are shown in Figure 17(b) and (c) for *E'* and *A'$_1$* peak maxima respectively. The average Raman spectrum for this area is shown in Figure 17(e). While the Raman spectrum indicates the formation of monolayer MoS_2 by the presence of the characteristic *E'* and *A'$_1$* peaks and a separation of ~19 cm^{-1}, the intensity ratio of *A'$_1$* to *E'* suggests a high level of p-doping in the film,[105] likely due to the presence of dopants/defects, or excess oxides. This can further be seen in the PL in Figure 17(f), where the relatively diminished and broadened PL peak[7, 63] could be indicative of a lack of crystallinity. Nevertheless, the single crystals shown here represent progress in TMD monolayer growth, as the size of the single crystal monolayers grown is similar to that which can be obtained by mechanical exfoliation, but with a much higher throughput.[7, 11] The single crystals shown here are also thinner, and larger in lateral dimensions, than those typically obtained by LPE, which can have a range of sizes and thicknesses in solution.[30]

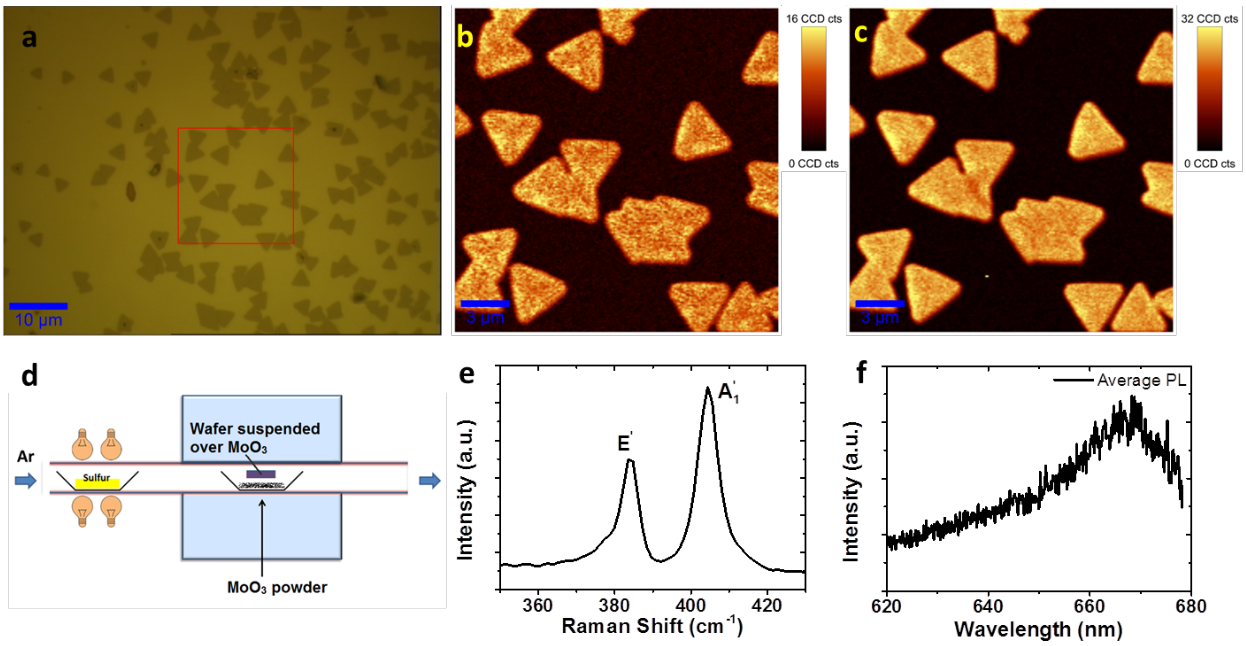

Figure 17

(a) Optical micrograph at 100X magnification of MoS_2 formed by CVD. (b) Map of *E'* Raman peak intensity maximum. (c) Map of A'_1 Raman peak intensity maximum. (d) Schematic of furnace used for CVD of MoS_2. (e) Average Raman spectrum. (f) Average PL spectrum.

However, it was observed that other parts of the same sample, as well as samples made during subsequent growths, consisted of molybdenum oxisulfide (MoO_xS_y) diamond shaped flakes, as shown in Figure 18(a). An average Raman spectrum was taken which confirmed that $MoOS_2$ peaks were present[66] as labelled by red triangles in Figure 18(b). Similar features have been reported at low sulfur concentrations during MoS_2 CVD.[66, 106] SEM images of these MoO_xS_y diamond-like geometric flakes are shown in Figure 18(c) and (d). The formation of MoO_xS_y in lieu of MoS_2 is likely due to the large amounts of excess oxides present in the CVD reaction in comparison to sulfur concentration available.

The presence of residual MoO_3 was also identified by a small shoulder on the average Raman spectrum, as labelled by the black triangle in Figure 18(b). Peak intensity maps were generated for the area marked with a red square in Figure 18(a). Raman intensity maps of the $MoOS_2$ peak at ~200 cm^{-1} and the MoO_3 peak at ~280 cm^{-1} are shown in Figure 18(e) and (f) respectively. Figure 18(e) confirms that the peak at ~200 cm^{-1} belongs to the geometric crystals. The intensity of this mode at ~200 cm^{-1} does not appear to have a direct correlation with the optical contrast of the crystals in the optical image in Figure 18(a). The intensity map of the peak at ~300 cm^{-1} in Figure 18(f) confirms the localised presence of MoO_3 in areas. The peak at 300 cm^{-1} is from the SiO_2/Si substrate.

The CVD method presented here has a number of disadvantages. These include lack of reliability of growth over a single substrate, lack of versatility in the system with regards to other TMD growth, and poor reproducibility of MoS_2 growth in subsequent attempts, due to tube poisoning with the oxides used. It is suggested that these factors may contribute to the varying reports of MoS_2 CVD in the literature, which were discussed in Section 2.1.4 in Chapter 2. It was clear that a different synthesis technique was required for reliable, reproducible growth.

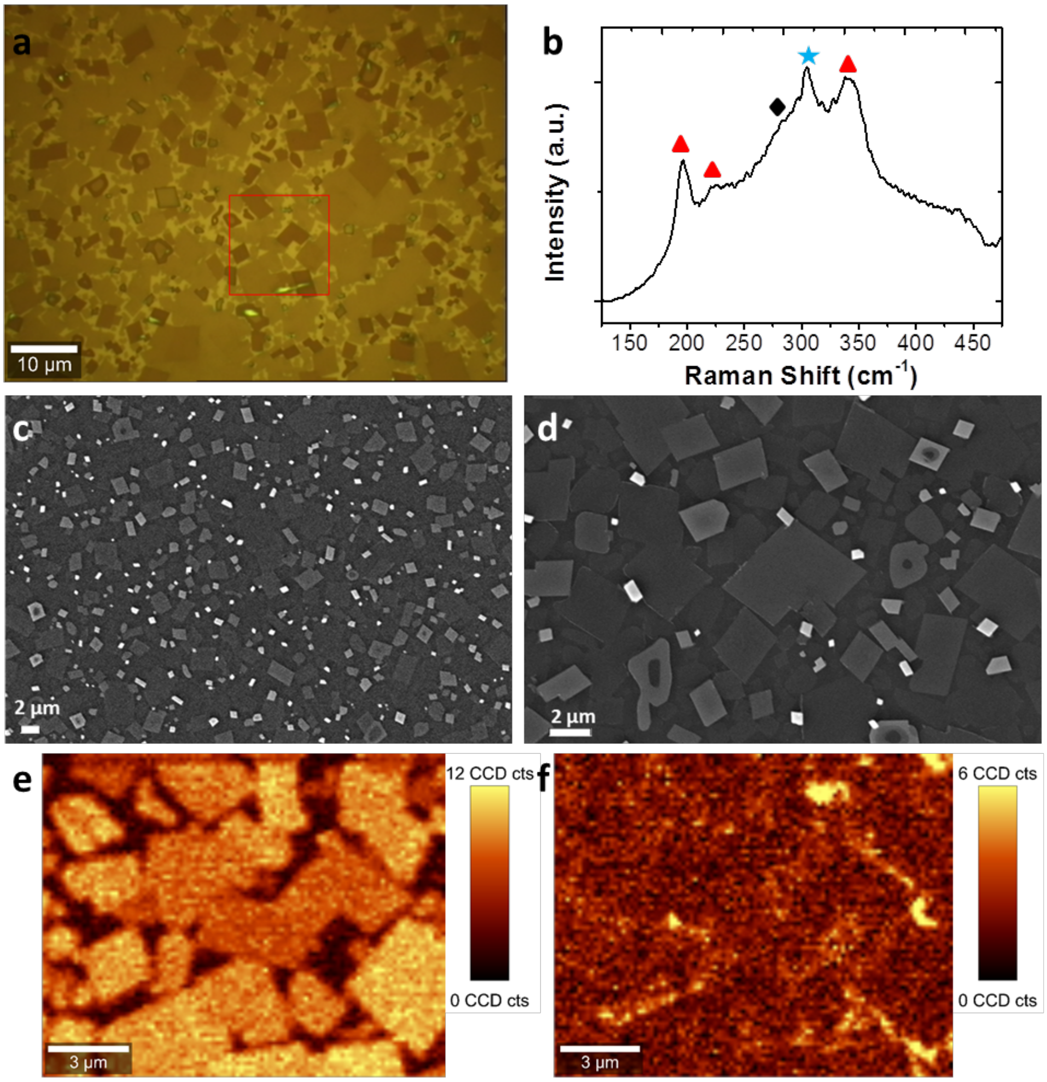

Figure 18

(a) Molybdenum oxisulfide (MoO_xS_y) contaminants on CVD samples. (b) Average Raman spectrum from MoO_xS_y flakes. The peaks which correspond to previous reports of $MoOS_2$ are labelled with red triangles and the peaks corresponding to MoO_3 are labelled with a black triangle. Si substrate contributions are labelled with a blue star. (c) Low magnification SEM of MoO_xS_y flakes. (d) Higher magnification SEM of MoO_xS_y flakes. (e) Raman intensity map of the $MoOS_2$ peak at ~200 cm^{-1} (f) Raman intensity map of the MoO_3 peak at ~280 cm^{-1}.

3.3 Chemical Vapour Deposition of MoS_2 in a Microreactor

Previous studies on the CVD growth of graphene[107, 108] have indicated that the use of a microreactor leads to an “improved” growth environment, with the resultant formation of large-area single crystals. For graphene, such a microreactor is created by folding the copper foil growth substrate back onto itself, creating an enclosure. In contrast to the growth of MoS_2, graphene CVD uses a hydrocarbon feedstock with hydrogen gas for growth, which is advantageous in that all the precursors are in the gaseous phase, and do not have to be melted and evaporated. In MoS_2 growth, as the precursors are typically solid phase molybdenum oxide and sulfur powders, there is an additional difficulty with microreactor setups in that both precursors need to be evaporated and reacted in a thermodynamically and kinetically optimal method. Placing one precursor in a microreactor while flowing the other over it in the gas phase could achieve this. MoO_3 nanoflake dispersions were chosen as the Mo source due to their well-defined length and thicknesses[109] and high purity. A controlled amount of MoO_3 dispersion was drop cast on a piece of 300 nm SiO_2 on Si. This acted as the Mo source, or seed substrate, during CVD growth. Another piece of SiO_2 on Si, which served as the growth substrate, was placed face down on top of this. This results in a microreactor being formed between the substrate with TMO precursor (the seed substrate) and the growth substrate, as depicted in Figure 19(a) and (b). It should be noted that an excess of sulfur is provided into the reaction chamber at elevated temperatures, making the oxide seed diffusion process the limiting step in this growth process. Reproducibility of precursor amounts can be achieved by using the same MoO_3 nanoflake dispersion in identical volumes and concentrations each time, with an identical spacing between the seed and growth substrate.

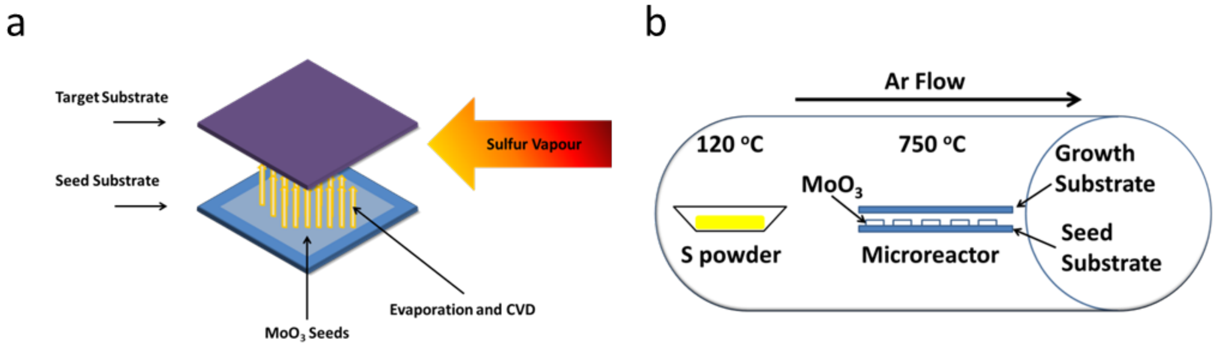

Figure 19
(a) Schematic of CVD microreactor formed between the seed and target substrates, where sulfur reacts with MoO_3 nanosheets to form MoS_2 layers on the top substrate. (b) Schematic of furnace setup. Sulfur powder is melted downstream and flowed through the microreactor.

MoO_3 nanosheet exfoliation was carried out by Dr. Damien Hanlon and Mr. J. B. Boland, as described previously,[109] to a concentration of ~0.63 mg/mL. Precursor layers of MoO_3 were made by dropcasting ~20 μL of an isopropanol (IPA) dispersion of MoO_3 nanoflakes onto commercially available silicon dioxide (SiO_2, ~290 nm thick) substrates, which were thermally grown on top of ⟨100⟩ oriented crystalline silicon (Si) wafers. The wafers were then placed on a hot plate at 150 °C until IPA had evaporated. The MoO_3 seed films were placed face up in a ceramic boat with a blank SiO_2 on Si substrate face down on top of them, in order to direct growth onto the top, blank substrate, as shown in Figure 19(a). For a typical MoO_3 concentration of ~0.63 mg/mL (0.63 g/L), the solution was diluted to 20% in IPA before dropcasting. The amount of MoO_3 used for a 20 μL deposition on the seed substrate gives ~2.5 μg of MoO_3 per substrate in each furnace run, in comparison to ~14 mg used per boat by standard recipes in the literature.[63] The boat was then placed into the centre of a quartz tube furnace and subsequently heated to 750 °C. Sulfur vapour was then produced by heating sulfur powder (MaTecK, 99%) to ~120 °C in an independently controlled upstream heating zone of the furnace, and transported to the samples using Ar gas as a carrier at a flow of 150 sccm for 20 minutes, in a similar manner to that described for TAC previously. A schematic of this is shown in Figure 19(b). After sulfurisation, the samples were annealed for 20 min at 750 °C in Ar carrier gas in order to ensure the reaction had completed fully, and then cooled down to room temperature. This is necessary as previous reports have shown that if a reaction time is too short, the sulfurisation process will not complete, and intermediate products can be formed. MoO_2 is the most common intermediate product, as it is one of the most stable molybdenum oxides[110] but intermediates such as $MoOS_2$ have also been observed for incomplete reactions,[66, 106] as discussed and characterised in Section 3.2. To avoid formation of these undesired products, an excess of sulfur was always used in the reaction. For TEM studies, the films were transferred to grids using a polymer support technique. Polymethyl methacrylate (PMMA 950K, MicroChem) was spin-coated onto the MoS_2, which were then floated on 2 M NaOH at room temperature until etching was completed, and the MoS_2/PMMA films were left floating on the surface.[42, 90] After cleaning in deionised water the films were transferred onto 300 mesh lacey carbon copper TEM grids (Agar Scientific). The PMMA layer was then dissolved by immersion in acetone at room temperature for 20 minutes.

In Figure 20(a) an optical image of a large scale MoS_2 monolayer film is shown. A scratch has been introduced here to allow contrast with the bare SiO_2 substrate underneath, emphasizing that the film is essentially homogenous over the visible area of approximately 300x250 μm. This uniform large-area deposition represents a significant improvement in TMD film growth when compared to the small, discrete triangles discussed previously. An SEM image of a typical as-grown film is shown in Figure 20(b). The visibility of grains and grain boundaries is clear using the topographically sensitive InLens detector at a low accelerating voltage of 1 kV, highlighting the homogeneity of the almost featureless surface over the depicted area of approximately 120 μm^2. The surface is predominantly flat and closed, with grain boundaries showing a slightly darker contrast. To investigate crystallinity of the films, HRTEM studies were undertaken, with the assistance of Mr. Clive Downing in the Advanced Microscopy Laboratory in Trinity College. A HRTEM image, shown in Figure 20(c), revealed a perfect hexagonal lattice, characteristic of highly-crystalline MoS_2. This was confirmed by the hexagonal diffraction pattern obtained, shown in the inset of Figure 20(c). XPS was used to characterise the films, with spectra taken by Dr. Nina C. Berner. A high resolution XPS spectrum of the Mo 3d core-level region of the monolayer film is shown in Figure 20(d). The position of the Mo $3d_{5/2}$ peak at ~230 eV is in agreement with the expected values for molybdenum in an oxidation state of Mo^{4+}, as is the case for MoS_2.[111] It should be noted that only very small amounts of sub-stoichiometric Mo(III) and MoO_3 were detected, indicating the high quality and uniformity of the studied areas.[111]

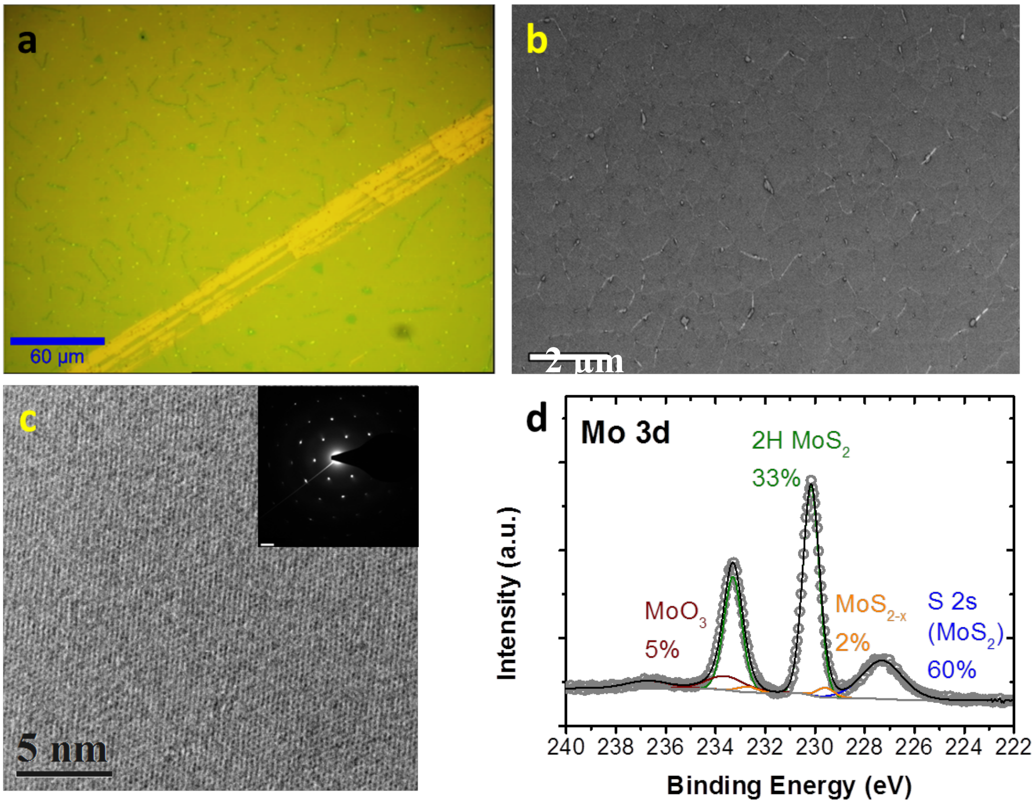

Figure 20
(a) Optical micrograph image of an MoS_2 layer at 20X magnification. A scratch has been introduced to show contrast of the mostly homogenous film with the underlying SiO_2 layer. (b) InLens SEM image showing the presence of grain boundaries. Scale bar is 2 µm. (c) HRTEM image of highly-crystalline monolayer MoS_2, showing hexagonal crystal symmetry. Diffraction pattern inset, scale bar for diffraction pattern is 2 nm^{-1}. (d) XPS spectrum of the Mo 3d core-level of a large area monolayer MoS_2 film.

Figure 21(a) shows a magnified optical image of an area of MoS_2 monolayer over which PL and Raman maps were obtained. The average PL spectrum is shown in Figure 21(c) with the relevant PL intensity map shown in Figure 21(b). This map shows the emergence of PL peaks expected for monolayer MoS_2,[7] verifying the high crystallinity and monolayer nature of the material. Raman spectroscopy was also used to evaluate the quality of the as-grown material. The maps of E' in Figure 21(d) and A'_1 in Figure 21(e) show little variation in intensity over the entire area, apart from in the presence of grain boundaries. The average Raman spectrum for the scanned area in Figure 21(f) shows peak positions of ~385 and 403 cm^{-1} for E' and A'_1, respectively, for non-grain boundary areas.[74, 75] This gives a peak to peak separation of 18 cm^{-1}, typical of monolayer MoS_2.[74, 75] In the vicinity of the grain boundaries, the *A'₁* mode intensity, and the peak separation between *E'* and *A'₁*, decreases. This can be explained by correlating the Raman peak change to the PL map. The decrease in intensity at grain boundaries of the PL map suggests they are molybdenum rich, and therefore n-doped,[63] quenching the PL. Previous reports show that n-doping also results in softening of the *A'₁* phonon, as seen here, meaning a decrease of relative intensity and peak frequency difference between *E'* and *A'₁* Raman modes.[81, 105]

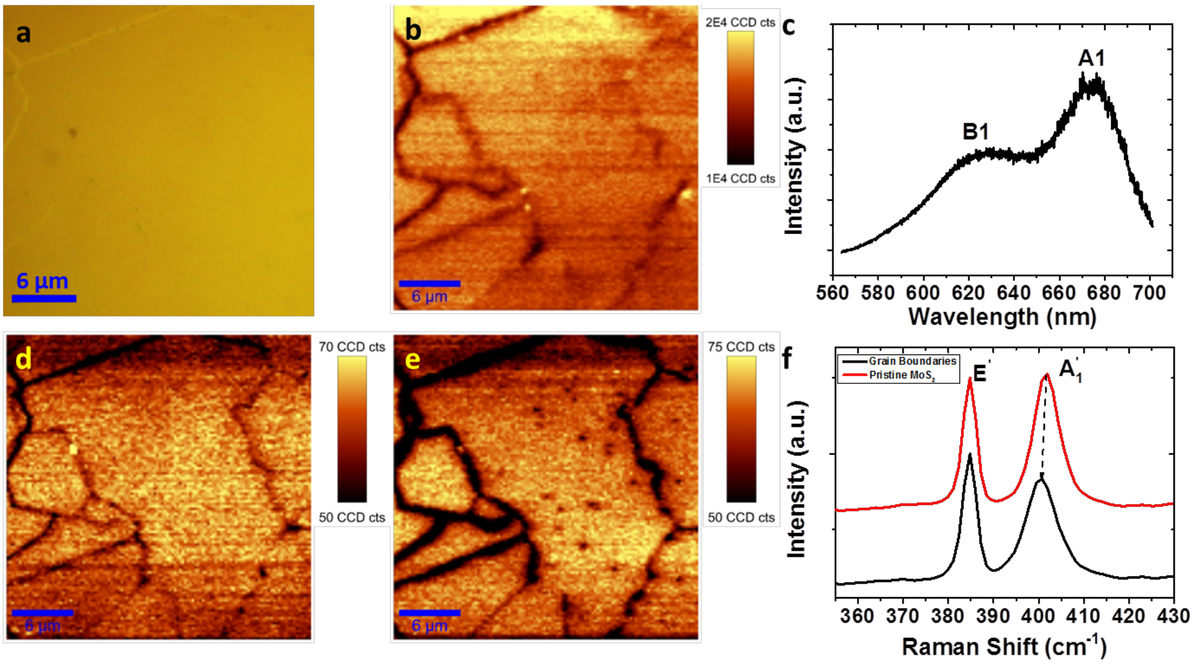

Figure 21

(a) Optical image of an MoS_2 film. Scale bar is 6 µm. (b) Map of PL intensity of the same area as in (a). The dark areas show a decrease in PL intensity in the vicinity of grain boundaries. (c) Average PL spectrum over the scanned area of 14,400 individual point spectra. (d) Map of *E'* Raman peak maximum intensity. (e) Map of *A'₁* Raman peak maximum intensity. (f) Average Raman spectra over grain boundary and non-grain boundary regions.

In order to further analyse the grain boundaries formed when MoS_2 layers stitch together, MoS_2 samples were studied as part of a collaboration with the group of Prof. Jani Kotakoski in Vienna.[112] Their studies showed that grain boundaries can result in bilayers or nanopores upon the merging of the grains of MoS_2. Stitched grain boundaries were found to be decorated by nanopores in samples made using the microreactor method described above, and these regions of nanoporous MoS_2 were suggested to have potential applications in DNA sequencing and water desalination.[112]

3.4 Patterned CVD Growth in a Microreactor

CVD microreactor growth was extended to the *in-situ* CVD patterning of MoS_2 by pre-patterning the MoO_3 seed layer before synthesis, as shown in the schematic in Figure 22. This was done by sputtering MoO_3 layers of 10 nm thickness from a solid target (MaTecK GmBH) through a metal shadow mask, consisting of arrays of squares 100 µm in size, using a Gatan PECS. The patterns were deposited onto commercially available silicon dioxide (SiO_2, ~290 nm thick) substrates, which were thermally grown on top of ⟨100⟩ oriented crystalline Si wafers. The oxide deposition rate and thickness were monitored using a QCM. Growth setup and conditions were identical to those described using MoO_3 exfoliated flakes previously.

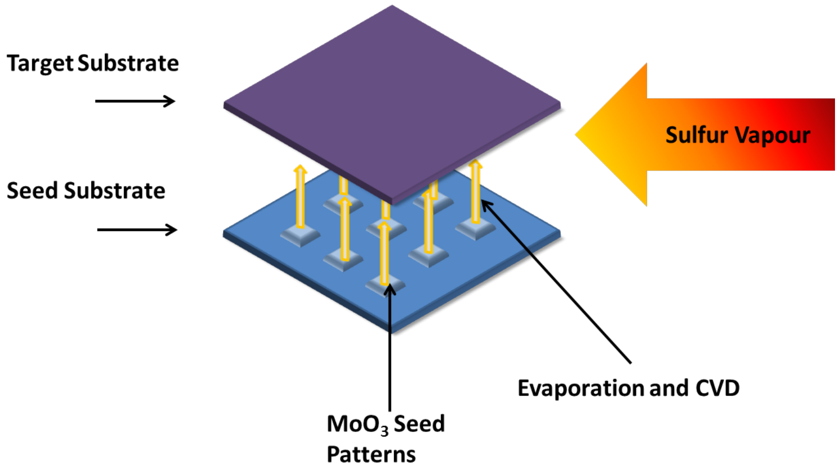

Figure 22
Schematic of patterned microreactor growth process.

This resulted in patterns of MoS_2 monolayers that can be grown directly on a target substrate. The features demonstrated here are circles of closed MoS_2 films with a diameter of approximately 100 µm as shown in Figure 23(a). The resulting patterns are of approximately the same diameter as the original square patterns, with some loss of square structure due to the initial spread of material during sputtering, and then the subsequent evaporation into a vapour source followed by re-deposition as MoS_2. This patterned growth is possible due to the close proximity of the TMO precursor. These patterned monolayers have the same high quality as the larger scale films shown previously in Figure 23(a). Although the resolution of the process is limited by a slight spread in growth, as shown in Figure 23(b), the method can produce multiple patterns without having to expose the monolayers to additional processing steps. This methodology could potentially be used to fabricate channels and other device components without the need for post growth processing steps.

Figure 23(c) shows the area over which Raman and PL scans were taken. Figure 23(d) and (e) show the corresponding respective intensity maps for the A1 and B1 exciton PL. The A1 intensity is far greater than B1 in all areas, further signifying the presence of highly crystalline monolayers.[7] Interestingly, there are small islands with enhanced PL that show no obvious change in the corresponding Raman maps. The average PL spectrum, as well as those from areas 1 and 2 as marked in Figure 23(d), is shown in Figure 23(f). One possible reason for this variation in PL intensity across the sample is that these patterned samples were synthesised using sputter deposited MoO_3 samples. These may not evaporate as readily as liquid-phase dispersed MoO_3 nanoflakes for a number of reasons. As it is patterned growth, there will be less total material deposited on the seed substrate, and therefore less material available to react. The nanoflake films are deposited over larger areas, and are rougher with a higher surface area allowing more material to be available to react. Also, sputtered MoO_3 has been reported to form the sub-stoichiometric compound, MoO_{3-x}[113] which has a higher melting point that $MoO_{3.}$ These factors could lead to inconsistencies in evaporation rate and therefore growth rate of monolayers, causing enhanced strain/doping to already grown monolayers as other growth begins to seed and join it. Raman analysis was used to evaluate the quality of the patterned CVD films. The maps of E' in Figure 23(g) and A'_1 in Figure 23(h) show little variation in intensity over the entire area, apart from in the presence of grain boundaries. The average Raman spectrum for the scanned area in Figure 23(i) shows peak positions of ~385 and 403 cm^{-1} for E' and A'_1, respectively,[74, 75] giving a separation of 18 cm^{-1} as expected for monolayer MoS$_2$.[74, 75] The high relative intensity of A'_1 in Figure 23(h) in comparison to E' in Figure 23(g) may be attributed to p-doping effects, which have previously been reported to cause an increase in the A'_1 mode intensity.[105, 114]

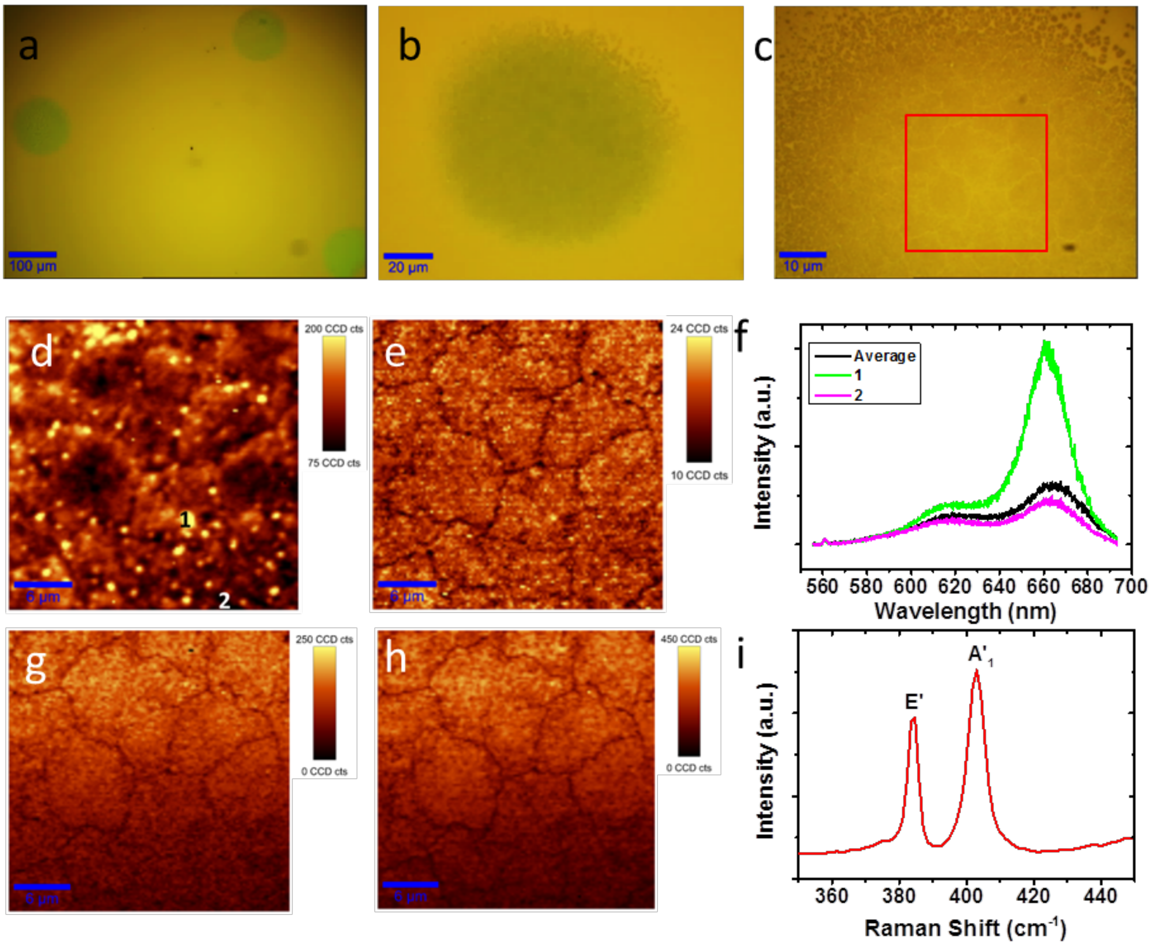

Figure 23

(a) Optical image of as-grown CVD monolayer MoS$_2$ dots at 10X magnification. (b) Optical image at 20X magnification of a MoS$_2$ continuous layer grown by the pattern transfer technique with no observable subsequent island growth on the terminated monolayer. (c) Optical image at 100X magnification of the area shown in (b), where the red box shows the entire area over which Raman and PL scans were taken. (d) A1 exciton maximum PL map. (e) B1 exciton maximum PL map. (f) PL spectra at points 1 and 2 as indicated in (d), and the average spectrum over the entire scanned area, consisting of 14,400 individual point spectra. (g) Map of E' Raman peak sum. (h) Map of A'_1 Raman peak sum. Scale bar is 6 µm for all Raman and PL maps. (i) Average Raman spectrum over

14,400 points taken in the scanned area the film, showing a peak separation of 18 cm^{-1}, which is in agreement with literature reports for monolayer MoS_2.

As it is possible to investigate the same features with AFM and Raman spectroscopy, the grain boundaries in the films can be analysed. In Figure 24(d), an optical image of the same area shown in Figure 23 is shown. The image is rotated 90^{o} in order to orient itself correctly with the AFM scans, which were taken over the area marked in red. AFM was carried out by Dr. Toby Hallam. The AFM phase mode and topography mode imaging scans in Figure 24(a) and (b), respectively show that the film is flat over the area of the scan, and consists of individual grains that grow together. The phase map, which has better lateral resolution in samples of different material properties, shows a higher response in the vicinity of the grain boundaries, as seen by comparison with the optical image, while the topography map indicates all the grain boundaries are slightly elevated in comparison with the rest of the film. Various height profiles over raised grain boundaries, as indicated by the dark blue lines in Figure 24(b), are shown in Figure 24(c). The height in each case was observed to be ~2.2 nm. This suggests that the areas shown are not gaps in the film, but rather buckled MoS_2 which forms as the grains grow together and upwards from different crystal lattice orientations. Similar features have previously been observed for CVD-graphene.[115, 116]

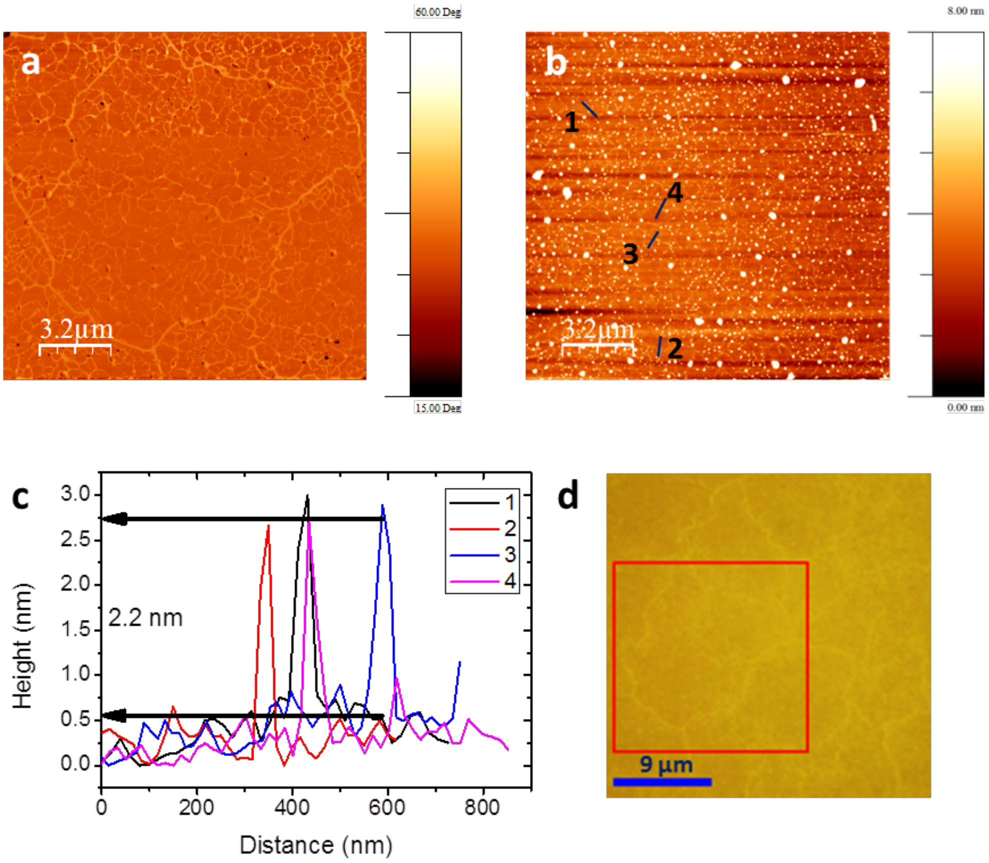

Figure 24
(a) Phase mode AFM image. (b) Topography mode AFM image of the same area. (c) Height profiles over dark blue lines shown in (b). (d) Enhanced optical image of the area analysed by Raman and PL in Figure 23. This optical image is rotated 90° from Figure 23 in order to orient correctly with AFM scans in (a) and (b). The area over which AFM scans were taken is marked by the red box.

The PL map in Figure 23(d) also interestingly shows enhanced and diminished PL at different areas of the grain boundaries of the MoS_2 monolayers. Previous reports have linked an increase in PL intensity with p-doping[63] which suggests that these regions are sulfur rich. This agrees with the previous observation of an increase in the A'_1 mode intensity indicating p-doping in the films.[105, 114] A decrease in PL intensity can similarly be attributed to n-doped molybdenum rich regions,[63] as discussed previously. The grain boundary observations also confirm that the monolayer films are continuous, while possessing boundaries and defects that have also been observed in other 2D materials.[117]

3.5 Chemical Vapour Deposition of WS_2 in a Microreactor

To test the suitability of the aforementioned CVD microreactor technique for the synthesis of other 2D materials, WS_2 was grown in an analogous method as a proof of concept. WO_3 powder was sonicated in IPA and dispersed onto SiO_2 wafers in a similar way to that described previously for MoO_3. For patterned growth, WO_3 patterns of 10 nm thickness were sputtered from a MaTecK target through a metal shadowmask, consisting of arrays of squares 100 μm in size, using a Gatan PECS. The patterns were deposited onto commercially available silicon dioxide (SiO_2, ~290 nm thick) substrates, which were thermally grown on top of ⟨100⟩ oriented crystalline Si wafers. The oxide deposition rate and thickness were monitored using a QCM. The CVD processing conditions were identical to those described for MoS_2.

Figure 25(a) shows an optical micrograph of a typical WS_2 film. As WO_3 is not a layered material in its anhydrous form,[118] the dispersed particles cannot be exfoliated in a well-controlled manner, and high concentrations of WO_3 nanoparticles of controlled size cannot easily be dispersed in solution. Hence the areas of large monolayer growth correspond to areas of good coverage of small WO_3 particles on the seed substrate. Figure 25(b) and (c) show maps of PL intensity and $2LA(M) + E^1_{2g}$ Raman intensity. Average PL and Raman spectra of the films are shown in Figure 25(d) and (e) respectively. The WS_2 Raman spectra of films shown here are in close agreement with the literature for WS_2 trends of Raman and PL as WS_2 tends from bulk to monolayer. Namely, the $(2LA(M)+E^1_{2g}):A_{1g}$ intensity ratio is much greater than 1, and impressive PL intensity is shown, indicating that exclusively monolayer WS_2 is being probed. The intense PL response is attributed to the 532 nm laser used, which is in resonance with WS_2,[58] as well as the overall higher quantum efficiency in WS_2 compared to MoS_2.[57]

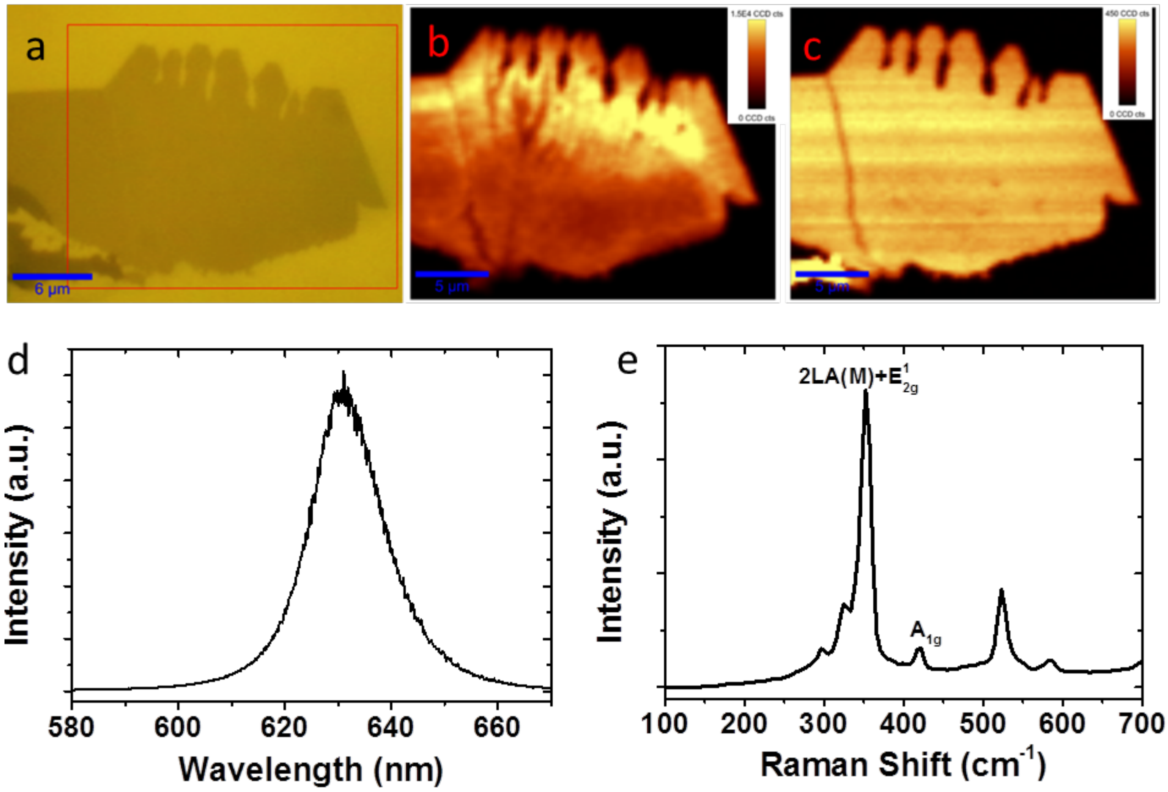

Figure 25

(a) Optical micrograph of a CVD-grown WS_2 monolayer. The red box indicates the area over which Raman and PL maps were taken. (b) Map of maximum PL. (c) Map of maximum $E^1_{2g}+2LA(M)$ Raman intensity. (d) Average PL spectrum, showing a bandgap of ~1.97 eV. (e) Average Raman spectrum.

Figure 26(a) shows an optical micrograph of a typical as-grown WS_2 layer synthesised from a patterned sputtered WO_3 seed precursor, with a red box indicating the area over which Raman and PL scans were taken. An increase in Raman peak intensity can be seen in multilayer regions of the sample, as shown in Figure 26(b). As this multilayer growth was minimal, the average Raman spectrum over the area, shown in Figure 26(c), shows predominantly monolayer WS_2 due to the relative peak intensities, as discussed above. The PL map in Figure 26(d) shows localised PL intensity enhancement in areas, likely for analogous reasons to those discussed for MoS_2. The position of the maximum PL of the WS_2 monolayer is centred around ~630 nm with some localised displacement, as shown in Figure 26(e). The average PL spectrum in Figure 26(f) indicates an optical bandgap of ~1.97 eV.

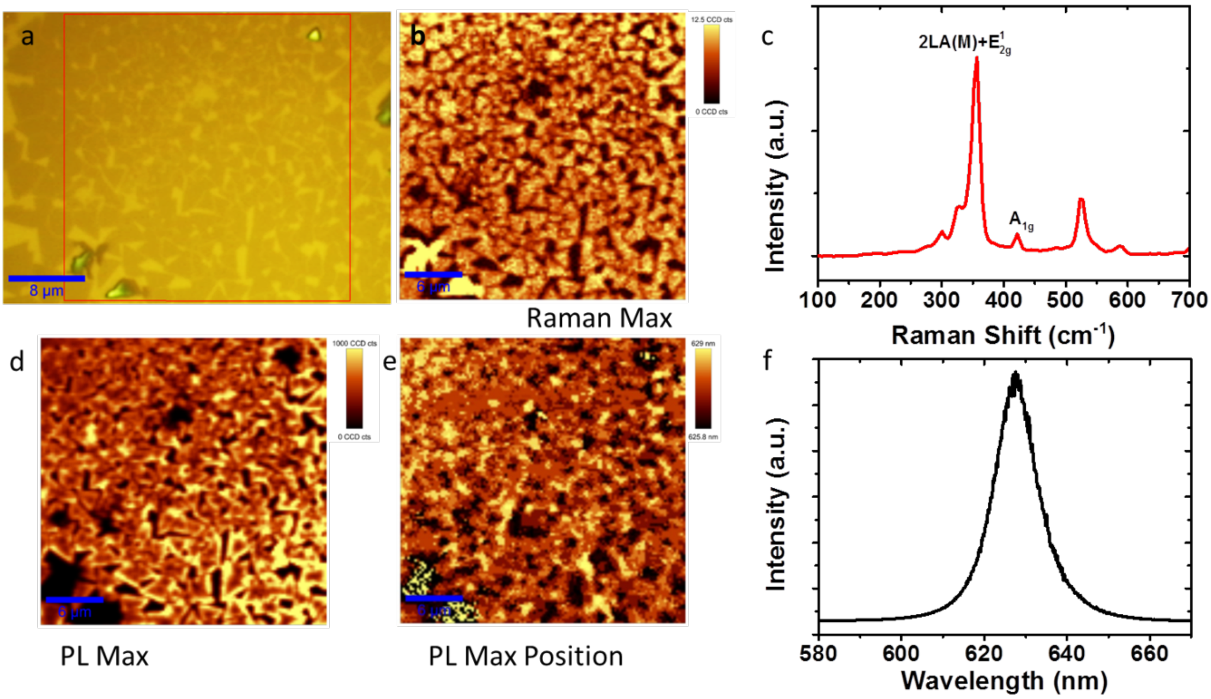

Figure 26

(a) Optical micrograph of CVD-grown WS_2 monolayer from sputtered WO_3 seed. The red box indicates the area on which Raman and PL maps were taken. (b) Map of maximum Raman peak intensity. (c) Average Raman spectrum. (d) Map of maximum PL intensity. (e) Map of maximum PL position (f) Average PL spectrum, showing a bandgap of ~1.97 eV.

3.6 Electrical Measurements on TMDs

3.6.1 Gas Sensing Response of Plasma Synthesised WS_2

The gas sensing capabilities of a 2 nm WS_2 film made with plasma-assisted synthesis, in collaboration with Prof. Colin Wolden's group as discussed previously, were tested by Dr. Kangho Lee by monitoring the change in resistivity of the WS_2 films upon NH_3 gas injection. The 2 nm sample with 20/80 nm Ti/Au sputtered contacts was loaded into the sensing chamber at N_2 atmosphere and subjected to a low vacuum treatment at 12.1 mbar. This was done to remove adsorbates from atmosphere, such as water vapour, from the surface of the film. A typical gas sensor response curve for a 2 nm device for 1 to 5 ppm of NH_3 gas is shown in Figure 27(a). It showed immediate response towards NH_3 molecules, but the relatively high volume of the gas-sensing chamber limits the response time; thus, the observed device resistance change continues for a few seconds directly after gas injection or interruption. This increase in conductivity as NH_3 donates charge to the WS_2 indicates that the WS_2 thin films presented here are n-type semiconductors, similar to bulk WS_2. An experimental limit of detection of 1.4 ppm NH_3 at room temperature was achieved, demonstrating the potential of WS_2 for sensing applications.

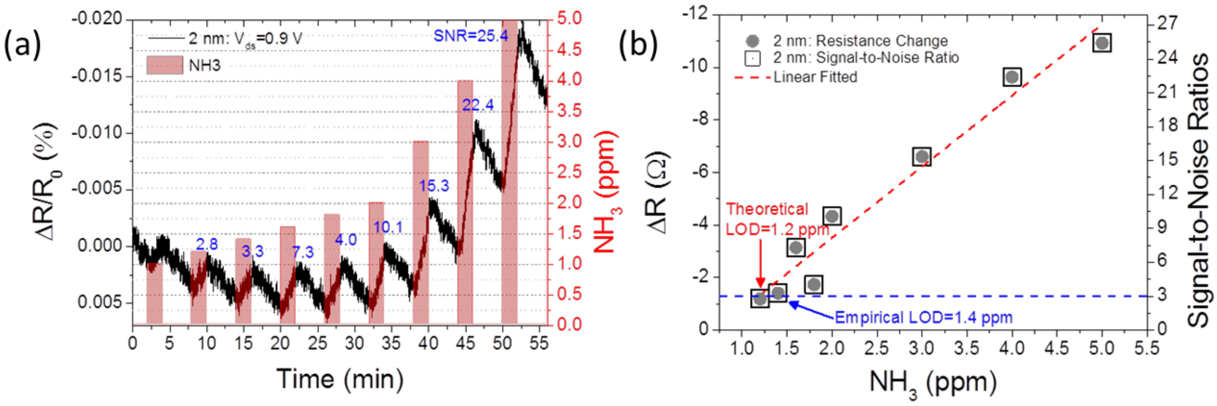

Figure 27

(a) Plot of 2 nm WS_2 device response to NH_3. (b) Plot of relative resistance change and signal-to-noise ratios plotted against NH_3 gas injection.

As shown in Figure 27(b), the sensor response, in terms of relative resistance change, was found to be linearly proportional to the concentration of NH_3 injection in this range. The films are also seen to recover in pure N_2 flow, but recovery is incomplete at room temperature. The baseline of resistance change gradually shifts during consecutive gas injections. Tight-bonding between WS_2 and NH_3 molecules may be responsible for this low recovery speed, as commonly observed in nanomaterial-based sensors at low working temperature. Annealing or ultra-violet (UV) illumination has previously been shown to assist in device recovery,[119-121] and could be used in future to assist in the recovery process.

In future, selective sensing in WS_2 based sensors could potentially be achieved by the use of binders or adsorbed molecules with functional groups that selectively react with and target specific analytes. Sensors derived from 2D materials have an active component which is all surface, meaning that they are generally very sensitive as the conductivity of the channel can be effectively modulated by adsorbates.

3.6.2 Electrical Transport Measurements of CVD Microreactor Grown MoS_2

Electrical transport measurements were performed across large channel areas that consisted of multiple grains. The electrodes were patterned by Dr. Hye-Young Kim using electron beam lithography with PMMA A3 and subsequent evaporation of Ti/Au=10/30 nm contacts. The sample was annealed in a vacuum at 120 °C for 140 minutes for removal of adsorbates.[122] Electrical characterisation was carried out by Dr. Hye-Young Kim, Dr. Kangho Lee and Dr. Toby Hallam with a Keithley 2602 source meter unit and a Keithley 2400 source meter with JANIS probe station at room temperature under vacuum. The measurements were performed immediately after the annealing step without exposing the device to ambient conditions. Figure 28(a) shows drain current vs. drain voltage (I_{ds} vs. V_{ds}) characteristics of the device from a two-terminal measurement with no applied back gate voltage, *i.e.* $V_{gs} = 0$ V. Slightly asymmetric contacts can be observed from the source-drain electrodes, which can be attributed to the presence of contact resistance. Figure 28(b) shows the transfer characteristics (I_{ds} vs V_{gs}) of the device for different source-drain voltages ranging from 0.5 to 2 V in increments of 0.5 V. The transfer curve shows strong n-type behaviour, and the current on/off ratio exceeds 10^3 for all values of source-drain voltage. Furthermore, the off-state of the device has the same level for all the applied source-drain voltages, as shown in Figure 28(c), meaning distinct on/off states can be observed. The field-effect mobility was estimated from the following equation:

$$\mu_{FE} = \frac{1}{C_{ox}} \cdot \frac{dI_{ds}}{dV_{ds}} \cdot \frac{L}{W} \cdot \frac{1}{V_{ds}}$$

where L is the channel length (~ 17.5 μm), W is the channel width (~ 145 μm), C_{ox} is the gate capacitance (~ 11.5 nF), and V_{ds} is the source-drain voltage. The maximum value of the slope, dI_{ds}/dV_{ds}, was used for calculations. For a bias voltage of 2 V, the field-effect mobility was estimated to be approximately 1.15 cm^2 V^{-1} s^{-1}, which is in line with or superior to values which had previously reported for both CVD-grown MoS_2[54, 55, 63] and mechanically exfoliated MoS_2, in the absence of high-K dielectric encapsulation layers.[11, 123] This is a relatively modest mobility value, but nonetheless it shows that large area CVD-grown MoS_2 is potentially viable for electronic devices despite the presence of grain boundaries.

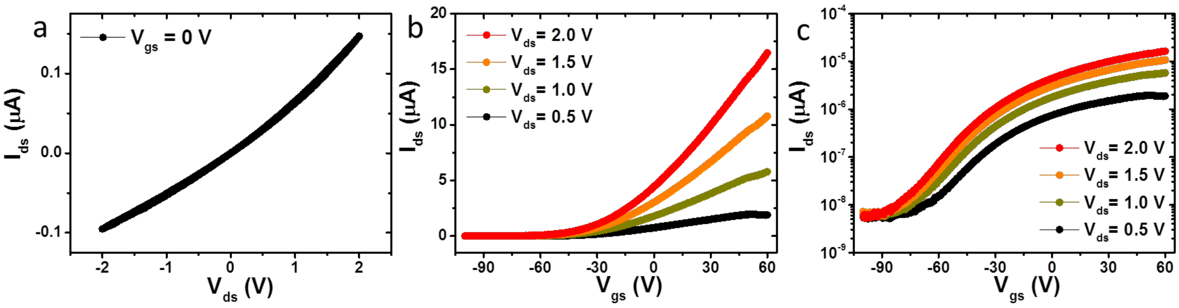

Figure 28

(a) Two terminal I_{ds}-V_{ds} characteristics of the device for V_{gs} = 0. (b) Transfer characteristics (I_{ds} vs V_g) of the device recorded for varying values of V_{ds}. (c) Transfer characteristics from (b) plotted on a logarithmic curve.

While the mobility values in the device reported here indicate the potential MoS_2 holds for device applications, reports of superior performance devices have also emerged in the literature. Multilayer MoS_2 transistors with scandium contacts and a 15 nm encapsulating layer of Al_2O_3 have been reported to achieve high effective mobilities of 700 cm^2 V^{-1} s^{-1}.[124] This high room-temperature mobility was attributed to the removal of contact resistance, which has limited MoS_2 devices in the past. Ionic liquid top-gating of FETs has been reported to successfully demonstrate mobilities of up to 220 cm^2 V^{-1} s^{-1}, which has been attributed to the reduction of the Schottky barrier at the source and drain electrodes.[125] It should be noted that simulations have shown that while MoS_2 mobilities may not be as high as state-of-the-art III-V semiconductors, MoS_2 transistors theoretically can obtain on/off ratio of $>10^{10}$, and may be useful in the future for low power applications.[126] Studies of the fabrication process of MoS_2 FETs showed that annealing the device after fabrication can affect the threshold voltage and dielectric leakage,[127] changing the performance of the device significantly. A record-high mobility of 34,000 $cm^2\ V^{-1}\ s^{-1}$ has been reported for 6L MoS_2 at low-temperatures in a van der Waals heterostructure device setup,[128] indicating that reduction of extrinsic scattering is crucial to achieve the high theoretical mobilities predicted for MoS_2. The van der Waals heterostructure was fabricated using graphene contacts and top and bottom encapsulation with hBN. The use of dielectrics to encapsulate 2D materials is a crucial step towards reliable device performance. Recent studies have explored using molecules such as perylene derivatives as anchors to seed and facilitate atomic layer deposition of high-K dielectrics such as Al_2O_3.[129]

3.7 Summary

A method for the scalable production of TMD thin films by TAC of pre-deposited transition metal films was presented. This TAC method produces thin films with few-layer character, and is ideal in potential applications in areas where high crystallinity is not a limiting factor, such as catalysis or in electrochemical cells. A method for low temperature synthesis of polycrystalline TMD thin films has also been presented using plasma-assisted chalcogenisation of metal oxide films. The quality of the films was assessed using XPS, Raman and SEM. These WS_2 thin films were used to demonstrate the first gas sensing response for WS_2, with highly sensitive detection towards NH_3.

A method for reliable production of TMD monolayers was presented, by use of liquid-phase exfoliated TMO nanosheet precursors in a close proximity microreactor setup for CVD growth. The quality of the as-grown layers was demonstrated using XPS, SEM and

TEM. Raman and PL spectra were used to further probe the quality of the layers and the properties of the grain boundaries present. Electrical transport results showed decent carrier mobilities, indicating that the grain boundaries do not strongly deteriorate the transport properties of the films. This process was extended to the growth of patternable TMD monolayers, by directly transferring patterns made with precursor layers to a growth substrate. This is an important result in the field of 2D materials, as it combines size-selectable, liquid dispersed nanosheets with chemical vapour deposition. This is a new pathway which could potentially lead to the development of patterned CVD monolayers for the production of future device components.

4 Raman Spectroscopy of $PtSe_2$

This chapter focuses on the Raman spectrum of $PtSe_2$ produced *via* the TAC method described in Chapter 3. The properties of bulk $PtSe_2$ have been studied since the 1960s,[130] but it remains to date a little studied group 10 layered TMD. Previous work on $PtSe_2$ includes theoretical calculation of its band structure,[131, 132] the use of $PtSe_2$/graphene hybrid materials in catalysis,[133] and the synthesis of $PtSe_2$ on single crystal platinum.[134] Some of the work in this chapter was published in the journal "*2D materials*".[135]

4.1 Introduction

In MoS_2, as discussed previously, the atomic layers typically consist of two hexagonal planes of sulfur atoms arranged around an interstitial hexagonal plane of Mo atoms in a trigonal prismatic, or 2H, arrangement. Other less studied layered TMDs have been shown to possess different crystal structures, known as the CdI_2 or 1T structure. Examples of these include ZrS_2, HfS_2, SnS_2, PtS_2 and $PtSe_2$. The properties of these 1T-type layered materials in their few-layer form have not been extensively experimentally studied to date, however recent computational reports have emerged that they may be suitable for emerging applications in photocatalysis[136] and optoelectronics.[132]

Initial reports have emerged on the epitaxial growth of $PtSe_2$ on a highly-crystalline Pt substrate under ultra-high vacuum (UHV) conditions.[134] This study identified a transition from semi-metallic to semiconducting behaviour with a reduction in layer number to bi- or monolayer, suggesting potential for an array of applications in electronics. Recent reports demonstrated that $PtSe_2$ can also been synthesised by CVD[137] and chemical vapour transport (CVT),[138] and is extremely air-stable in FETs.[138] Additionally, $PtSe_2$ has previously been synthesised by chemical means for use in graphene hybrid materials.[133] $PtSe_2$ films synthesised by low-temperature selenisation of Pt films have been shown to act as high-performance gas sensors with short response and recovery times.[139] They have also been integrated with Si to fabricate photodiodes and photovoltaic cells, establishing $PtSe_2$ as a strong candidate for future sensors and optoelectronic devices.[139] While Raman spectroscopy is used extensively for the facile, non-destructive characterisation of TMDs and other nanomaterials, the Raman characteristics of $PtSe_2$ have not been extensively investigated. Here, the synthesis of $PtSe_2$ films of controllable thickness by direct selenisation of predeposited Pt precursor layers *via* the TAC method described in Chapter 3 is presented and the evolution of Raman spectra with thickness is studied. This demonstrates the usefulness and practicality of the TAC synthesis method and Raman spectroscopy in the synthesis and analysis of 2D materials.

4.2 Experimental Analysis - Synthesis, Materials and Methods

$PtSe_2$ thin films were fabricated by Dr. Niall McEvoy using a similar process to that previously described for other TMDs in Section 3.1, and as illustrated in Figure 29.[41, 42, 55] Briefly, Pt thin films of varying thicknesses were sputtered from a MaTeck Pt target using a Gatan PECS onto silicon (Si) substrates with 300 nm dry thermal oxide (SiO_2). The deposition rate and film thickness were monitored with a QCM. These films were then placed in the centre of a quartz-tube furnace and heated to a growth temperature of 450 ^{o}C under 150 sccm of 10% H_2/Ar flow. Selenium (Se) vapour was then produced by heating Se powder (Sigma Aldrich, $\geq$ 99.99%) to ~220 ^{o}C in an independently-controlled, upstream heating zone of the furnace, and carried downstream to the Pt films for a duration of 2 hours, after which the furnace was cooled to room temperature. A schematic of the furnace is shown in Figure 29. As discussed previously, films synthesised by TAC have been reported to show a threefold expansion in thickness following selenisation of the metal film.[44] For clarity, films will be referred to by their starting Pt thickness. Raman spectroscopy was performed using a WITec Alpha 300R with 532 nm and 633 nm excitation lasers with a spectral grating of 1800 lines/mm and a 100× microscope objective (0.95 N.A., spot size ~0.3 μm). Spectra were taken with a laser power of < 300 μW in order to minimise sample heating. Polarised Raman measurements were conducted by Dr. Jian-Yao Zheng with a confocal microscope (Renishaw InVia System), in which a 100× (0.7 NA) microscope objective was used to focus the laser beam and collect the scattered light. An excitation line of 488 nm with a spot size of ~ 0.7 μm was used. Density functional theory calculations were performed by Dr. Carlo Motta with the all-electron code FHI-aims,[140] giving the local density approximation (LDA) and the generalised gradient approximation (GGA). The "tight" basis set was employed, and an 8×8 k-points grid was used to sample the in-plane BZ. All the geometries were optimised with a force tolerance of 0.001 eV/Å. Long-range van der Waals interactions were included with the Tkatchenko-Scheffler scheme.[141] Phonon spectra were computed with the Phonopy code[142] with finite displacements of 0.001 Å. XPS spectra were recorded by Dr. Nina Berner under UHV conditions ($<10^{-8}$ mbar) on a VG Scientific ESCAlab MkII system using Al K_α X-rays and an analyser pass energy of 20 eV. After subtraction of a Shirley background, the core-level spectra were fitted with Gaussian-Lorentzian and Doniach-Sunjic (for the metallic Pt 4f component) line shapes using the software CasaXPS. For the STEM analysis, an as-grown $PtSe_2$ thin film of 0.5 nm starting Pt thickness was transferred onto a holey carbon TEM grid. A polymer support technique was employed for the transfer process, whereby polymethyl methacrylate (PMMA, MicroChem) was spin-coated onto the as-grown sample and baked in atmosphere at 150 °C for 5 min. The films were then floated on 2 M NaOH at 80 °C until the $PtSe_2$/PMMA films were left floating on the surface. After cleaning in deionised water the films were transferred onto grids and dried in a desiccator. The PMMA support layer was then dissolved in acetone and the films baked prior to STEM measurements. Atomic-resolution images were obtained by Prof. Dr. Jani Kotakoski and his group with a Nion UltraSTEM 100 operated at 60 kV, using a high angle annular dark field (HAADF) detector.

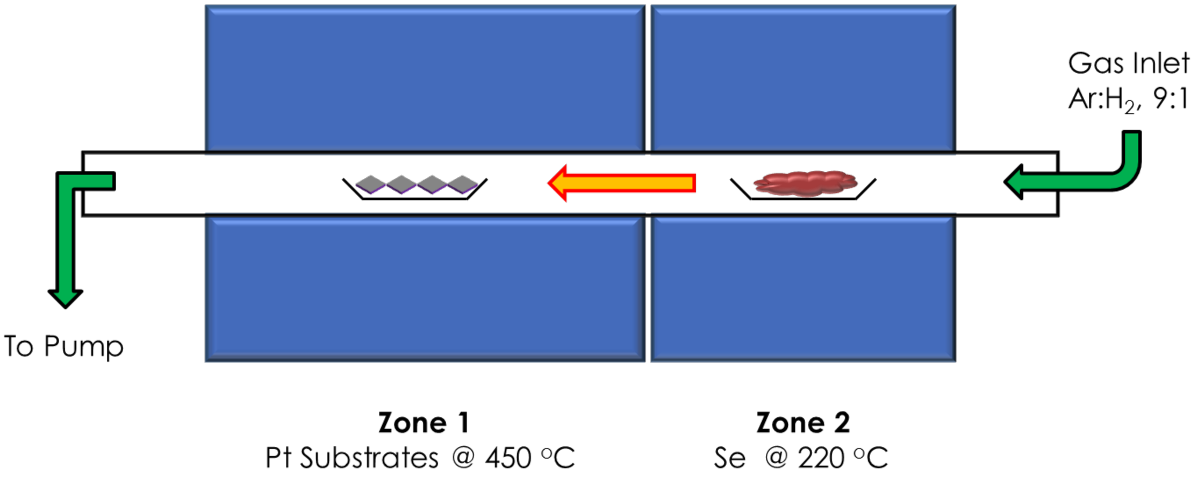

Figure 29

A schematic of the furnace setup described in the experimental procedures for fabrication of the $PtSe_2$ thin films.

4.3 Results and Discussion

4.3.1 Structural and Chemical Characterisation of $PtSe_2$

In Figure 30(a), a HAADF STEM image of $PtSe_2$ grown from 0.5 nm Pt is presented. This allowed the determination of the crystal structure of suspended $PtSe_2$, free of substrate interactions or epitaxial growth influences. Previous studies revealed $PtSe_2$ to have an octahedral, or 1T, type crystal structure,[134] more commonly known as the CdI_2 crystal group. While harsh chemical treatments are required to convert 2H MoS_2 and other group 6 TMDs to their 1T phase,[21, 143] group 10 TMDs such as $PtSe_2$ are most stable in the 1T phase. This has been known since the 1960s[130] but only observed at the atomic level recently.[134, 135] The results presented here in Figure

30(a) show regions of different thicknesses and crystal orientations, similar to what has been observed in previous reports on the production of TMDs by TAC.[47, 144, 145] It was possible to identify monolayers and bilayers of $PtSe_2$ in the CdI_2 crystal structure in the HAADF STEM image in Figure 30(a), where the crystal structure is also shown in the schematic. The overlay of theoretical and experimental structure is also shown for clarity in Figure 30(a). Image simulations of monolayer and bilayer $PtSe_2$ performed with QSTEM software[146] are presented in Figure 30(b), which confirm the interpretation of layer thicknesses when compared to the experimental image in Figure 30(a). XPS spectra were recorded on a $PtSe_2$ thin film synthesised from a starting Pt film thickness of 0.5 nm. The Pt 4f core-level spectrum for each film shows primarily peaks associated to $PtSe_2$. The Pt 4f can be deconvoluted into three contributions, the main one at ~72.3 eV attributed to $PtSe_2$ and two smaller ones at ~74 eV and ~71 eV to oxides and unreacted Pt metal, respectively. The relative atomic percentages are shown in Figure 30(c). The Pt $5p_{3/2}$ peak also lies in the same region, but has not been used for analysis. The Se 3d peak is shown in Figure 30(d), and can be deconvoluted into two contributions, one from $PtSe_2$ and another one at higher binding energies from edge or amorphous Se.

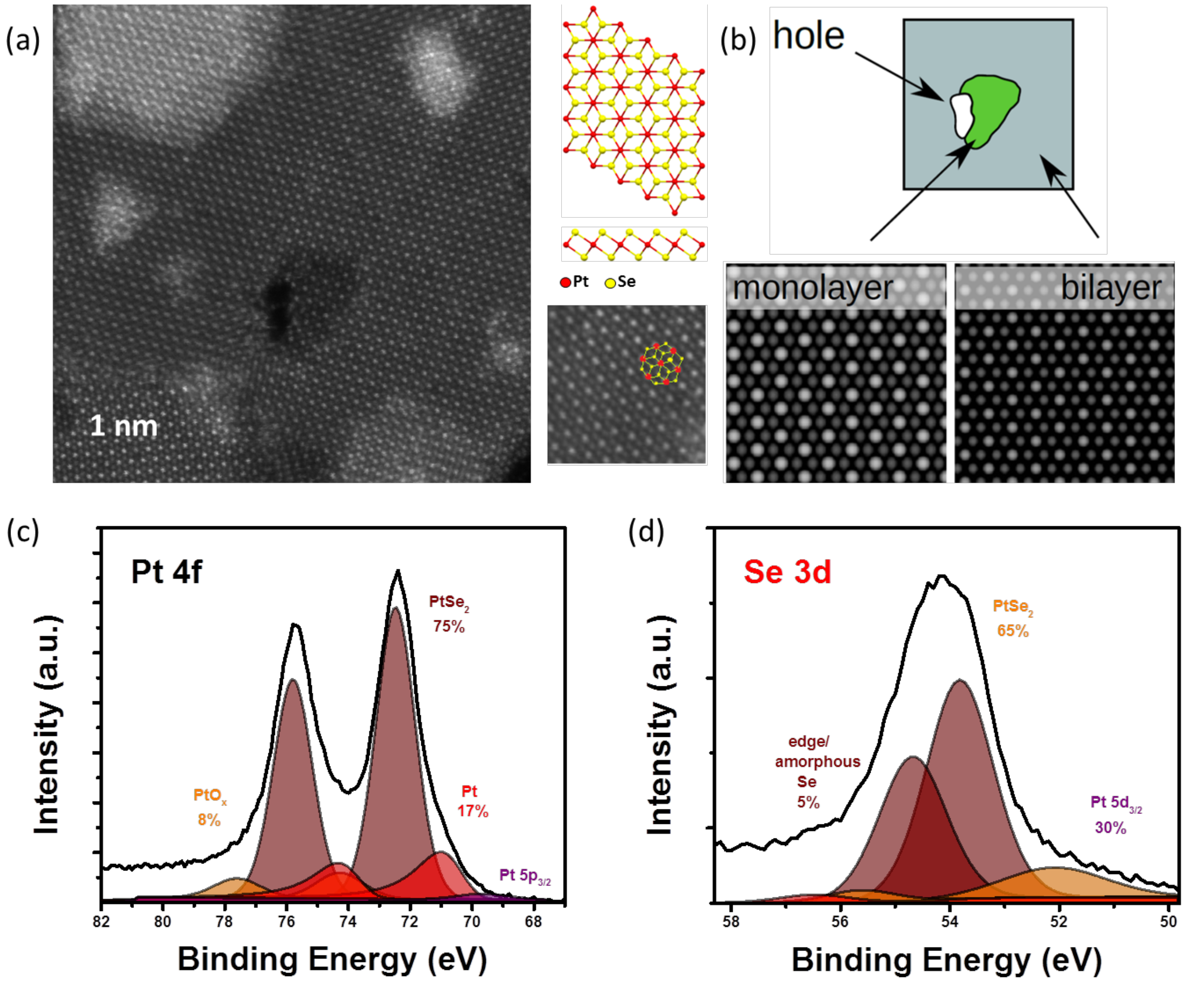

Figure 30

(a) HAADF STEM of PtSe$_2$ displaying regions of varying layer number, with crystal structure overlaid on PtSe$_2$ HRTEM monolayer (b) Image simulations with QSTEM software for mono- and bilayer structures of 1T phase of PtSe$_2$. (c) XPS spectrum of 0.5 nm PtSe$_2$ film showing the Pt 4f peak. (d) XPS spectrum of same 0.5 nm PtSe$_2$ thin film showing the Se 3d peak.

4.3.2 Raman Spectroscopy of PtSe$_2$

The Raman spectra of layered TMDs are generally characterised by two main peaks corresponding to the in-plane and out-of-plane motions of atoms. The CdI$_2$ lattice type configuration of PtSe$_2$ layers results in a D_{3d} point-group symmetry with 3 atoms in a unit cell. The D_{3d} symmetry results in the following irreducible representations of modes at the centre of the BZ:

$$\mathit{\Gamma} = A_{1g} + E_g + 2A_{2u} + 2E_u$$

The two Raman-active modes are labelled as A_{1g} and E_g, while the IR active modes are A_{2u} and E_u.

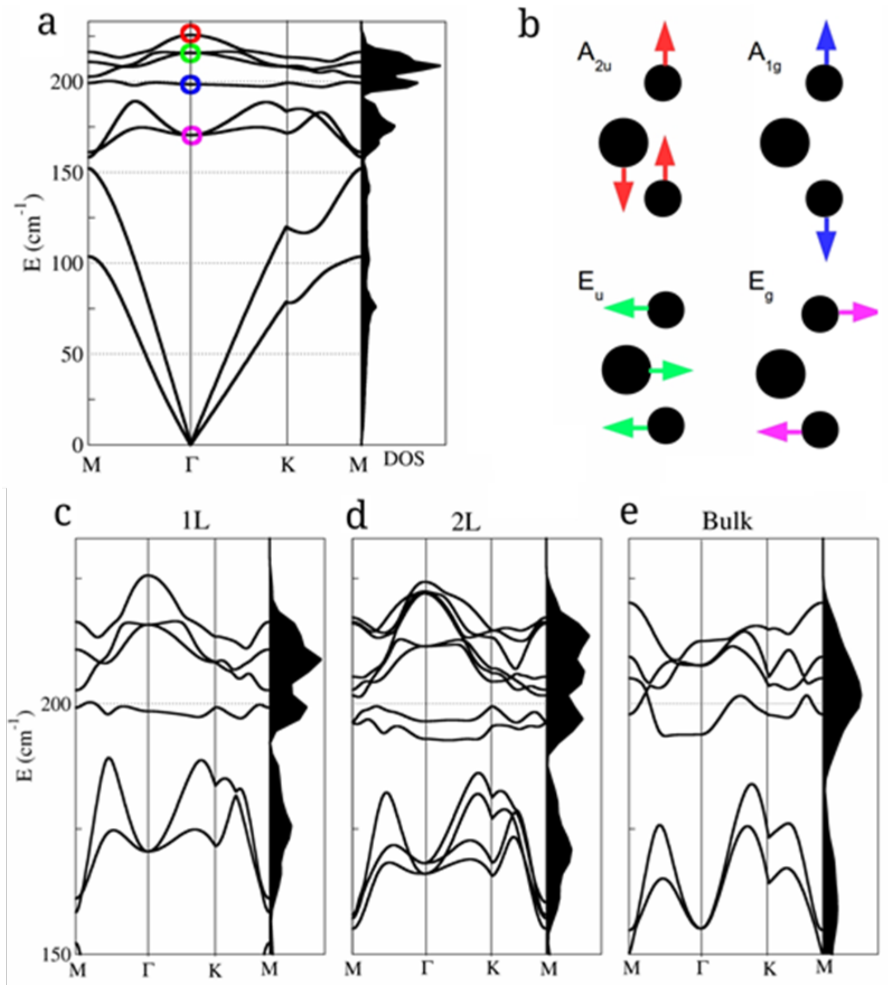

Figure 31

(a) Calculated phonon dispersion and DOS of monolayer $PtSe_2$. (b) Schematic diagrams of vibrational modes in $PtSe_2$ layers. Large spheres are Se atoms; smaller spheres are Pt atoms. The colours associate each mode with its energy in the bandstructure. (c, d, e) Calculated phonon dispersion curves of monolayer, bilayer and bulk $PtSe_2$.

In Figure 31(a), the calculated phonon-dispersion curves of monolayer $PtSe_2$ are presented with the corresponding density of states (DOS) shown beside them. A schematic of the vibrational modes in $PtSe_2$ is shown in Figure 31(b), with arrows drawn as guides to show the origin of each mode on the phonon dispersion curve. These include the in-plane E_g mode, describing the in-plane vibration of selenium atoms in opposite directions within a single layer, and the A_{1g} mode describing the out-of-plane vibration of selenium atoms.

The calculated phonon dispersion curve allows a theoretical prediction to be made about the frequencies of both Raman and IR active vibrations. It should be noted that GGA usually underestimates the phonon frequencies as a result of a tendency to overestimate the equilibrium volume[147]. Nevertheless, as shown in the results in Table 1, it was possible to calculate phonon frequencies for all Raman and IR vibrational modes as predicted by symmetry considerations. Phonon dispersion curves for monolayer, bilayer and trilayer $PtSe_2$ that focus on the region of interest (~150-250 cm^{-1}) are shown in Figure 31(c), (d), and (e).

Table 1 - Calculated phonon frequencies for $PtSe_2$.

Mode Prediction	**LDA (rel. cm^{-1})**	**GGA (rel. cm^{-1})**
E_g	183.11093	170.48864
E_g	183.15949	170.49728
A_{1g}	200.78692	198.51035
E_u	233.23271	215.76595
E_u	233.40321	215.78960
A_{2u}	237.92582	225.62144

The electronic bandstructures of monolayer and bilayer $PtSe_2$ have also been calculated, and are shown in Figure 32. For the monolayer, the bandgap was found to be indirect, with a magnitude of ~1.6 eV. This decreases significantly in the bilayer, where the gap reduces to ~0.8 eV. The bandgap transitions are indicated by black arrows in Figure 32. Previous reports have noted the difference in calculated electronic bandgap for monolayer $PtSe_2$ for different calculation approaches, ranging from 1.2 eV to 2.1 eV.[134, 136] The value of 1.6 eV reported here is close to values calculated using similar generalised gradient approximation approaches.[136] Other approaches, including many-body approaches, have been reported to underestimate the experimental bandgap.[136, 148] Experimental bandgaps measured using angle-resolved photoemission spectroscopy have a high level of agreement with quasiparticle bandgap calculations,[134, 136] while exciton binding can cause those measured by optical spectroscopy to be reduced.[136] However, all calculation methods reported to date agree with the trend of decreasing bandgap with increasing layer number of $PtSe_2$. Bulk $PtSe_2$ is shown here to have a semi-metallic band structure, in agreement with previous predictions.[134] Such radical change in the band structure upon changing the number of layers is common in 2D materials, due to changes in the dielectric screening of long-range Coulombic forces between layers as the layer number decreases.[147] The emerging bandgap in $PtSe_2$ thin layers suggest that the material may be of high interest for future electronic and optoelectronic applications. In theory, it could allow seamless metal-semiconductor-metal contacts in devices where each component is fabricated from a different thickness of the same material. A similar structure using PdS_2 to realise a single-material logical junction with negligible contact resistance has been theoretically modelled.[149]

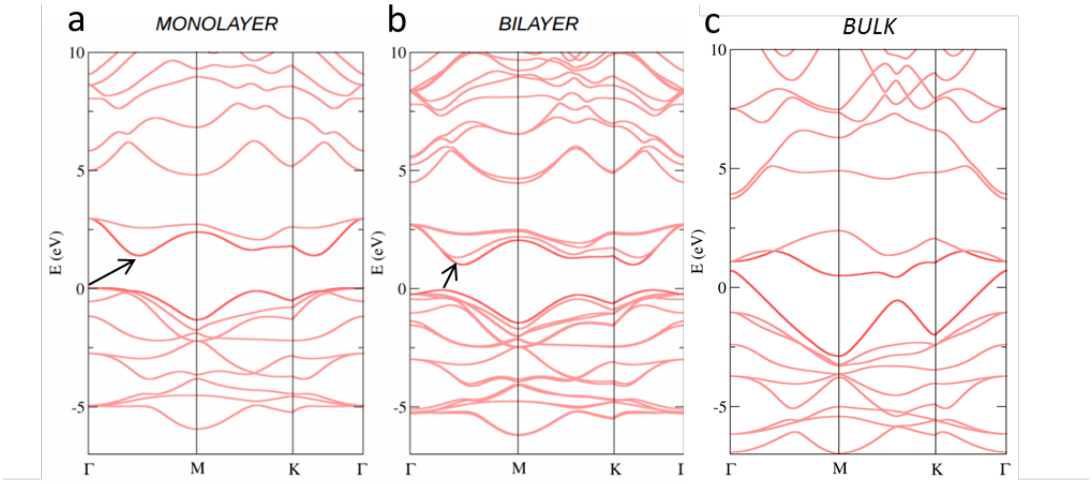

Figure 32

Calculated electronic bandstructures of (a) monolayer (b) bilayer and (c) bulk $PtSe_2$.

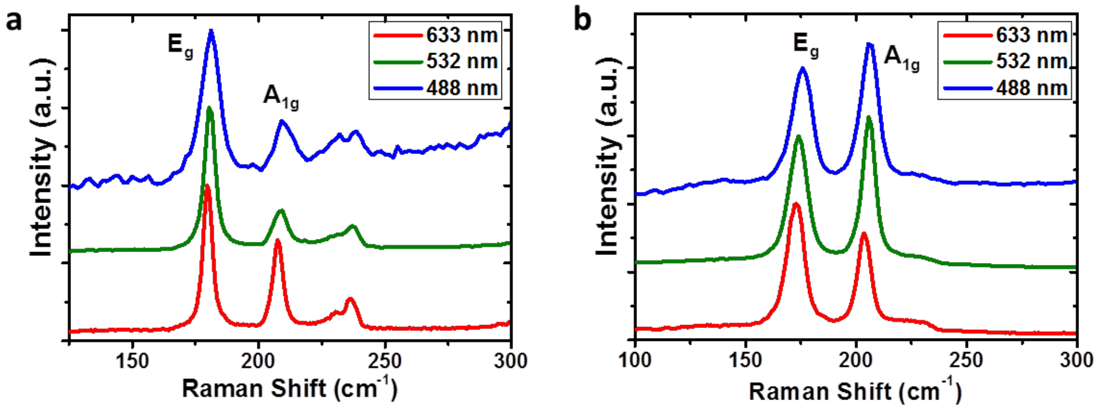

Figure 33

Raman spectra of $PtSe_2$ films taken using blue (488 nm), green (532 nm) and red (633 nm) excitation wavelengths. (a) 0.5 nm thickness spectra (b) 5 nm thickness spectra. These spectra have been normalised to the E_g mode at ~175 cm^{-1} for clarity.

Experimental Raman spectroscopy measurements were taken on as-synthesised $PtSe_2$ thin films. In Figure 33(a) and (b), Raman spectra of $PtSe_2$ layers from starting Pt thicknesses of 0.5 and 5 nm respectively are shown for 488, 532 and 633 nm excitation wavelengths. Two prominent vibrational modes are visible, at ~175 and ~205 cm^{-1}, with a less intense contribution at ~230 cm^{-1}. By comparison with the phonon frequency predictions for perfect crystals in Figure 31, the peaks at 175 and 205 cm^{-1} are assigned to E_g and A_{1g} modes, respectively. The differences between theoretical and experimental Raman frequencies are attributed to previously discussed GGA estimation errors and the fact that the thin films studied here do not consist solely of pristine layers of definite thicknesses. The less prominent feature at ~230 cm^{-1} is assigned to an overlap between the A_{2u} and E_u modes, which are longitudinal optical (LO) modes involving the out-of-plane and in-plane motions of platinum and selenium atoms respectively. These modes are visible in IR spectroscopy and resonance Raman spectroscopy. A_{2u} and E_u modes have previously been observed for layered materials with similar symmetry to $PtSe_2$, including as HfS_2[150] and CdI_2.[151] The relative intensity of this A_{2u} and E_u contribution is strongest for the 0.5 nm film where it is evident that it stems from two separate peaks at ~230 cm^{-1} and ~237 cm^{-1}.

These modes are much less intense for the 5 nm film and manifest as a broad feature centred at ~ 230 cm^{-1}. A schematic of the A_{2u} and E_u mode vibrations is shown in Figure 31(b).

Polarisation-dependent Raman studies using a 488 nm excitation laser were carried out to support the peak assignment detailed above. Porto's notation *A(BC)D* is used to describe the Raman geometry and polarisation, where A and D represent the wavevector direction of the incoming and the scattered light, respectively, while B and C represent the polarisation direction of the incoming and scattered light[152]. In this experiment, [100], [010] and [001] axes are labelled X, Y and Z respectively. Figure 34(a) shows spectra of a 1 nm $PtSe_2$ thin film. For the $Z(YY)\bar{Z}$ polarisation, both E_g and A_{1g} peaks can be observed. When in the $Z(YX)\bar{Z}$ polarisation, there is a clear decrease in the intensity of the A_{1g} mode, confirming the out-of-plane nature of this mode. In Figure 34(b) spectra of a 5 nm $PtSe_2$ thin film are shown. Similar to the 1 nm film, when in the $Z(YY)\bar{Z}$ polarisation, both E_g and A_{1g} peaks can be observed. Note that the A_{1g} peak is larger in the 5 nm film due to increased out-of-plane interactions between more layers in thicker samples, similar to previous reports for MoS_2.[153] For the $Z(YX)\bar{Z}$ configuration, there is a clear decrease in the intensity of the A_{1g} mode, further confirming the out-of-plane behaviour of this mode, but it does not disappear completely. This can be attributed to the polycrystalline nature of the sample, as shown in the STEM analysis. The crystal grains in the film are small (with lateral dimensions on the order of a few nm) and randomly oriented, which leads to A_{1g} contributions that are diminished but not entirely absent in the thicker samples, where more edge-on orientation of films could be present.[40]

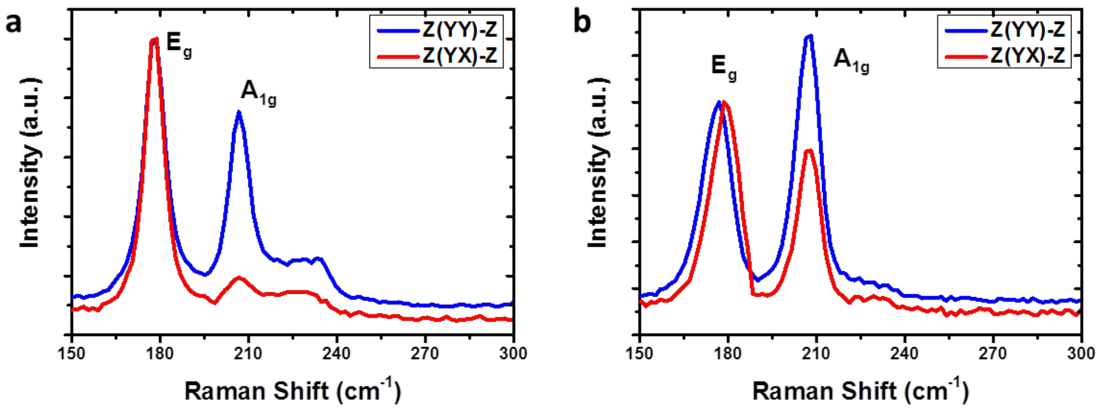

Figure 34

Polarisation response in Raman spectra of $PtSe_2$ films taken using the blue (488 nm) wavelength laser excitation (a) 1 nm thickness spectra (b) 5 nm thickness spectra.

Figure 35(a) shows Raman spectra of $PtSe_2$ layers of a variety of thicknesses in the 100-600 cm^{-1} region. The characteristic Si peak, observed at ~520 cm^{-1}, decreases in relative intensity as the $PtSe_2$ layer increases in thickness. When normalised to the E_g peak at ~176 cm^{-1}, as highlighted in Figure 35(b), the intensity of the A_{1g} peak at ~205 cm^{-1} shows a clear change in relative intensity with changing thickness, as the thicker films show a dramatic increase in relative intensity in comparison to thinner films. A *LO* peak attributed to an overlap of A_{2u} and E_u is also observable at ~235 cm^{-1}, as discussed above, which consistently decreases in relative intensity with increasing film thickness. This is supported by the Raman analysis of commercially-available, bulk $PtSe_2$ crystals, grown by CVT, in Figure 37, where this peak is effectively absent for bulk samples. Comparison of the Raman analysis of CVT-grown $PtSe_2$ crystals with the $PtSe_2$ films synthesised here serves as confirmation of successful $PtSe_2$ growth. To further analyse the relationship between the A_{1g} mode and the thickness, Figure 35(c) shows the extracted thickness/intensity ratio of the A_{1g} mode in $PtSe_2$, showing a dependence similar to that previously observed in the out-of-plane Raman modes in other TMD thin films with increasing thickness,[58, 71] and reflecting the increased van der Waals interactions between the layers with high layer numbers. Figure 35(d) shows rescaled spectra highlighting the red-shift of the E_g mode with increasing thickness, similar to the red-shift observed in the E^1_{2g} mode in TMDs such as MoS_2 with increasing layer number. This indicates that $PtSe_2$ in a 1T structure behaves similarly to other layered materials in 2H structures, where stacking-induced structural changes and long-range Coulombic interactions dominate the changing atomic vibration.[71] The red-shift of the E_g mode with increasing thickness is also predicted by theoretical calculations. Neglecting the monolayer case, which does not match with the experimental realisations presented here, the bilayer and bulk predicted Raman shifts from Figure 31(d) and (e) can be compared here to experimental measurements. In the calculated Raman shifts, the A_{1g} mode remains pinned at 193 cm^{-1}, while the E_g mode shifts from 166 cm^{-1} to 155 cm^{-1} from bilayer to bulk $PtSe_2$ respectively. This energy shift of ~10 cm^{-1} is in agreement with the magnitude of the shift observed here by Raman scattering. Experimentally, a small red-shift in the A_{1g} mode is observed with increasing thickness which this is less pronounced than the shift in the E_g mode.

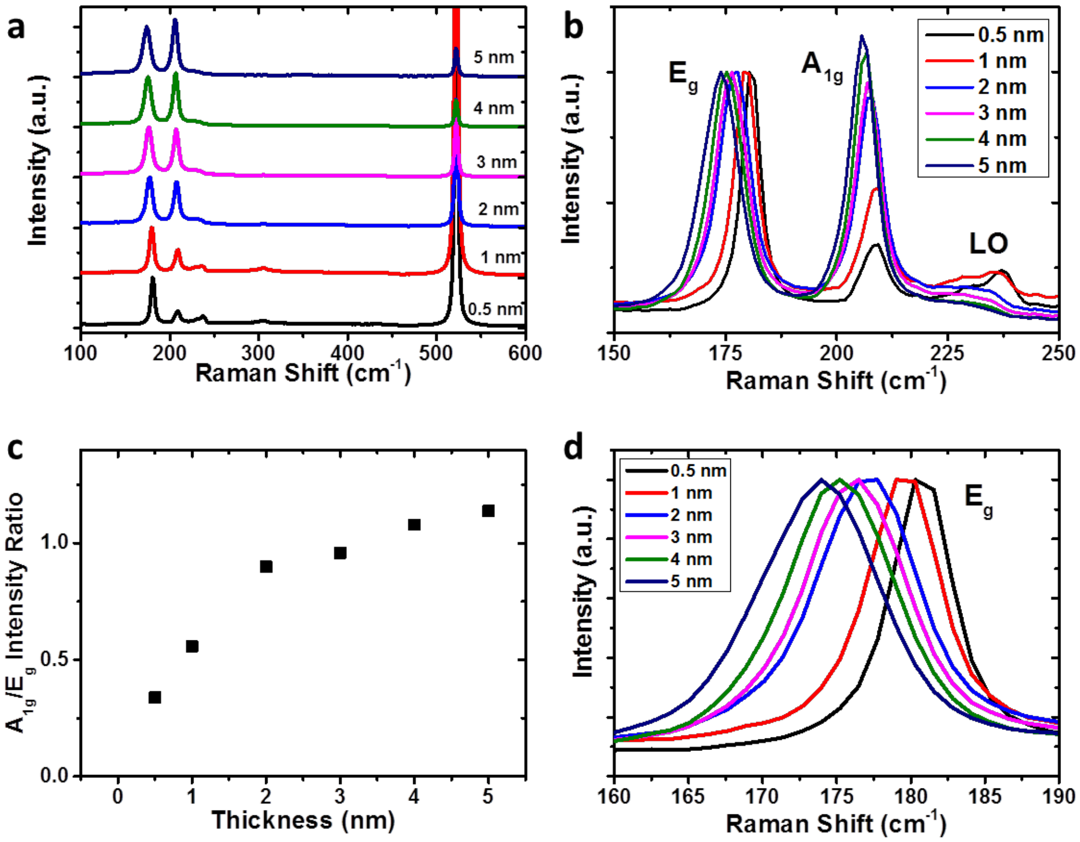

Figure 35

Thickness dependent Raman spectra of $PtSe_2$ films taken using a 532 nm laser (a) Raman spectra of $PtSe_2$ films from 100 to 600 cm^{-1}. (b) Raman spectra of $PtSe_2$ films in the 150 to 250 cm^{-1} region (c) Analysis of thickness dependent behaviour of the A_{1g} mode with starting Pt thickness (d) Raman Spectra from 160 to 190 cm^{-1} highlighting the red-shift of the E_g mode with increasing thickness.

It should be noted that a general increase in signal intensity was observed for both modes with increasing film thickness, which is to be expected for thin film samples where there is more material for incoming light to interact with. Above a certain thickness, it is anticipated that increased light scattering and less reflectance from the substrate would contribute to a lower Raman intensity, which has been previously reported for MoS_2.[75] An increase in the linewidth of the E_g mode as the film thickness increases is also evident in Figure 31(d), and merits further investigation. Similar broadening has been observed for the E^1_{2g} mode of disordered MoS_2[82] and the effect observed here could be due to increased disorder with increasing layer thickness. This is supported by the broadening of the E_g mode observed at edge sites of CVT crystals, as shown in Figure 37. Additional Raman spectra of the TAC synthesised samples were acquired using a 633 nm excitation laser, and further emphasise the discussed trends in spectral characteristics with changing thickness. These spectra are presented in Figure 36.

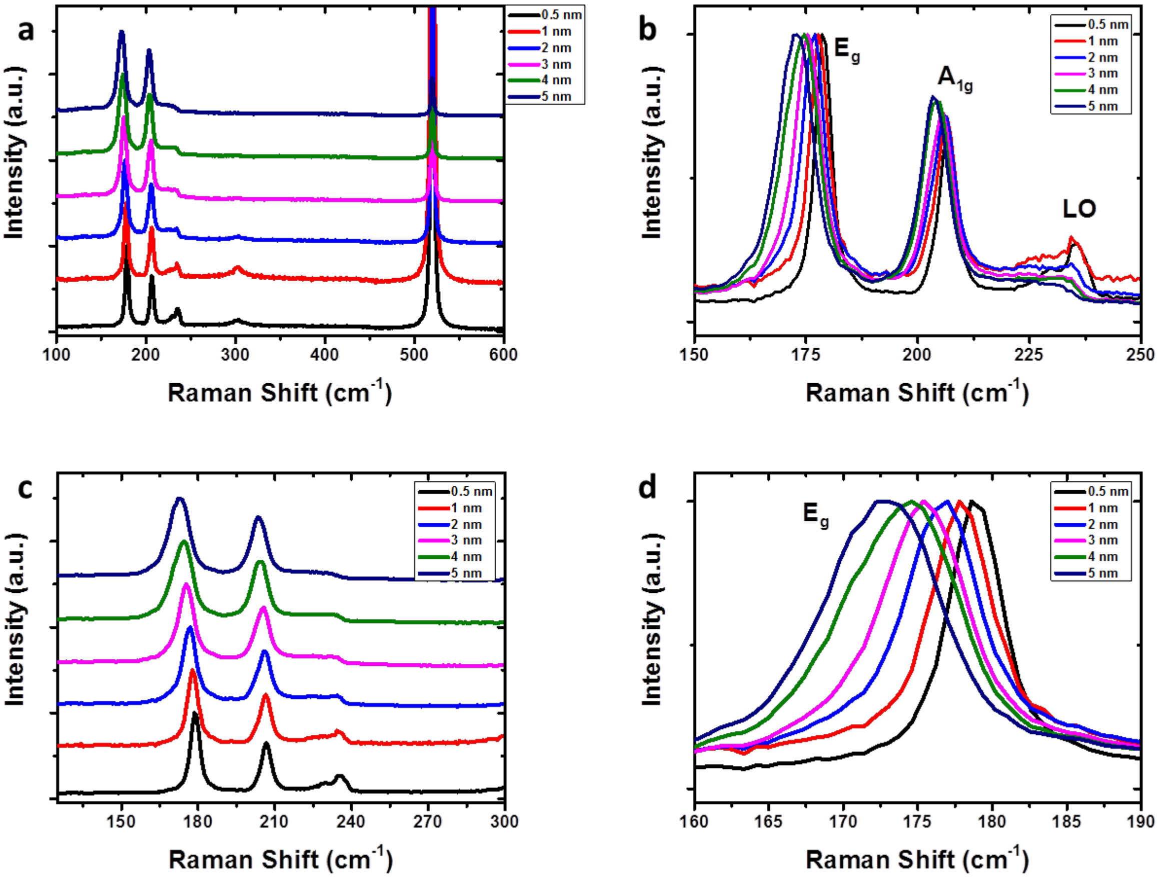

Figure 36

(a-d) Raman spectra of the same samples probed in Figure 35, acquired using a 633 nm excitation laser, with various areas enhanced to facilitate comparison.

A bulk CVT-grown $PtSe_2$ crystal was used as a reference sample for Raman analysis. Optical micrographs of this crystal are shown in Figure 37(a, b) in which edge and basal planes are evident. Much like the films grown by TAC of predeposited Pt, the CVT crystal displays clear E_g and A_{1g} modes in its Raman spectrum. Analysis of this crystal allowed for observations to be made on the differences in Raman spectra between edge and basal plane sites. Representative Raman spectra, normalised to the E_g mode intensity, extracted from these edge and basal plane sites are shown in Figure 37(c). The spectrum of a basal plane site is similar to that of the thickest films examined above, albeit with a lower relative A_{1g} mode intensity, and can be considered representative of bulk-like $PtSe_2$. The intensity of both Raman modes is greater in the edge sites, as shown in the maps in Figure 37(d, e), which are taken over the area marked by the red box in Figure 37(b). This is probably due to the greater sample interaction volume in these areas due to the exposed edges. Interestingly, the relative intensity of the A_{1g} mode is considerably greater in the edge site regions, as shown in the map of A_{1g}/E_g relative intensity in Figure 37(f). This is most likely due to the greater contribution from out-of-plane modes in this region. Similar trends have been seen previously for crystals of MoS_2.[153] The high relative intensity of the A_{1g} mode in the Raman spectra of the thicker TAC $PtSe_2$ films discussed previously can be attributed to the polycrystalline nature of the samples. A broadening of the E_g mode is also observed at edge sites. Similar broadening of the E_g mode was observed with increasing film thickness as previously shown in Figure 35 and Figure 36.

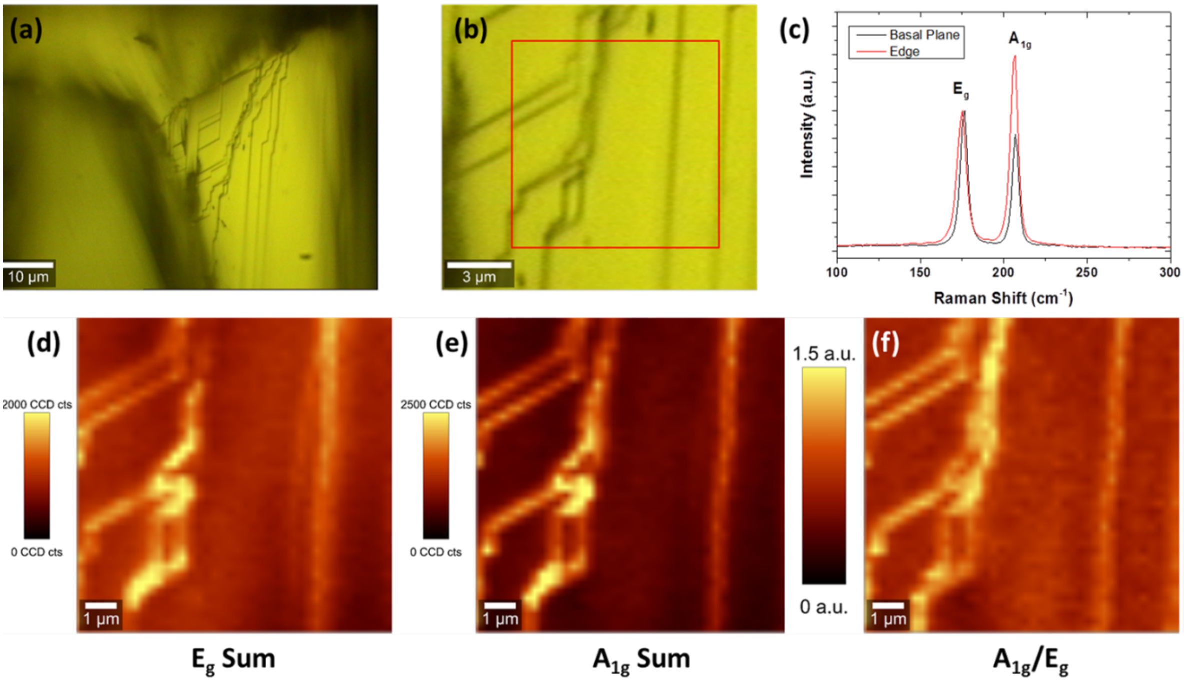

Figure 37

(a, b) Optical micrographs of CVT-grown $PtSe_2$ crystal. (c) Raman spectra extracted from basal plane and edge regions. (d, e) Raman maps of the peak sum of the E_g and A_{1g} modes from the area marked by red box in (b). (f) A_{1g}/E_g peak sum ratio map from area marked in (b).

4.4 Summary

$PtSe_2$ thin films of controllable thickness have been synthesised by direct selenisation of predeposited Pt layers. STEM studies confirm that the crystal lattice is 1T, allowing the Raman spectrum of $PtSe_2$ to be analysed and interpreted. A detailed analysis of the Raman-active modes in $PtSe_2$ has been presented. The A_{1g} and E_g out-of-plane and in-plane modes, respectively, have been identified using a variety of different laser wavelengths, and these assignments have been confirmed using polarisation-dependent measurements and theoretical modelling. Furthermore, the thickness dependence of these modes has been investigated. The results presented in this chapter will expedite further research into the synthesis and characterisation of exotic TMDs, and further build upon recent reports of high-performance electronic devices based on $PtSe_2$ thin films.[139]

5 Low-Frequency Raman Spectroscopy of TMDs

In this chapter, CVD-grown TMD monolayer and few-layer crystals are studied by Raman spectroscopy. Low-frequency Raman spectra and mapping of shear and layer-breathing modes of MoS_2, WS_2, $MoSe_2$ and WSe_2 are presented. The changing behaviour of these modes is correlated with layer number in the materials, and it was possible to examine unusual stacking behaviour in the selenides that had not previously been observed in exfoliated crystals. Some of the results presented in this chapter were published in the journal "*Scientific Reports*".[154]

5.1 Introduction

As discussed previously, the interest in 2D materials beyond graphene emerged following the reports of Mak *et al.*[7] and Splendiani *et al.*[8] in 2010, which demonstrated that MoS_2 showed extraordinary PL in its single layer form, indicating a significant change in the electronic structure of MoS_2 with layer number. Recent reports have suggested that transition metal diselenides such as $MoSe_2$ may be more attractive for use in electronic devices than transition metal disulfides. Compared to MoS_2, $MoSe_2$ has a narrower bandgap of 1.5 eV with a similarly high mobility,[155] tunable excitonic charging effects[156] and a 10-fold narrower linewidth,[157] indicating that it could be useful both in device applications and as a platform for studying fundamental physics in the 2D limit.[157] It is imperative that the composition, quality and thickness of all these materials are assessed before they can be considered for use in applications. Techniques such as AFM and TEM are useful in the characterisation of layer number and crystalline quality, but suffer from low sample throughput and laborious sample preparation. Recent studies have shown that Raman spectroscopy can provide information on defect levels, strain and doping in TMDs. Additionally, Raman modes can be observed in the low-frequency (<50 cm^{-1}) region of the Raman spectrum of TMDs, known as the shear modes (SMs) and layer-breathing modes (LBMs) and recent reports have demonstrated the practicality of studying these modes.[74] These low-frequency modes occur due to relative motions of the planes themselves, either perpendicular or parallel to the atomic layers, and can prove useful in the characterisation of 2D materials. The layer number sensitivity of low-frequency Raman modes of these materials means they could act as a simple verification of layer number and crystallinity for these materials. While many reports on Raman of TMDs focus on the high-frequency Raman modes in these materials, technological limitations previously prevented Raman mapping of low-frequency modes to show layer number, uniformity, single crystals and grain boundaries due to their Raman shift position appearing in the ultra-low-frequency region beyond the filter cut-offs for most commercial Raman spectrometers. Ongoing developments in the use of components such as multiple notch filters[158] can now allow measurement of the low-frequency peaks with low excitation powers and short acquisition times.

Herein, a systematic study of the low-frequency Raman peak positions and intensities of CVD-grown TMDs, including MoS_2, $MoSe_2$, WSe_2 and WS_2 is presented. The efficacy of low-frequency Raman mapping to probe the symmetry, quality, and layer number in CVD-grown 2D materials is demonstrated.

5.2 Experimental Techniques

5.2.1 Experimental details of CVD growth of TMDs

MoS_2 and WS_2 growth was carried out as described in Chapter 3. For $MoSe_2$ and WSe_2 growth, precursor layers of MoO_3 and WO_3 were liquid-phase exfoliated and dispersed onto commercially available silicon dioxide (SiO_2, ~290 nm thick) substrates as described for MoS_2 growth in Chapter 3. The precursor substrates were then placed in a quartz boat with a blank 300 nm SiO_2/Si substrate face down on top of them, creating a microreactor. This was then placed in the centre of the heating zone of a quartz tube furnace, and ramped to 750 ^{o}C under 150 sccm of forming gas (10% H_2 in Ar) flow at a pressure of ~0.7 Torr. Se vapour was then produced by heating Se powder to ~220 ^{o}C in an independently controlled upstream heating zone of the furnace, and carried downstream to the microreactor for a duration of 30 minutes after which the furnace was cooled down to room temperature.

While the described growth procedures can produce large-area monolayer coverage,[90] areas consisting of crystals with a variety of layer thicknesses were specifically chosen to highlight the capability of low-frequency Raman mapping for layer-number and stacking-orientation investigation.

5.2.2 Experimental details of Raman and PL Analysis

Raman and PL spectroscopy were performed using a Witec alpha 300R with a 532 nm excitation laser and a laser power of <500 μW, in order to minimise sample damage. The Witec alpha 300R was fitted with a Rayshield Coupler to detect Raman lines close to the Rayleigh line at 0 cm^{-1}. A spectral grating with 1800 lines/mm was used for all Raman spectra whereas a spectral grating with 600 lines/mm was used for PL measurements. The spectrometer was calibrated to a Hg/Ar calibration lamp (Ocean Optics) prior to the acquisition of spectra. Maps were generated by taking 4 spectra per μm in both x and y directions over large areas. AFM measurements were carried out by Dr. Toby Hallam.

5.3 Results and Discussion

As mentioned in Chapter 1, TMDs can exist in 3 main polytypes, depending on the co-ordination of chalcogen atoms around the metal atoms, and the stacking order of the layers. The octahedral 1T phase is the most stable phase for certain layered materials, such as $PtSe_2$ which was discussed in Chapter 4. However, since the 1T polytype of common group 6 TMDs, such as MoS_2 and $MoSe_2$, is metastable and not found in nature,[159] it will not be discussed here. The more common 2H and 3R polytypes are semiconducting, with trigonal prismatic coordination, with similar properties but differing stacking orders of metallic and chalcogen atoms. For example, 2H has a stacking order of AbA BaB AbA BaB, where capital letters indicate chalcogen atoms and lower-case letters indicate metal atoms, while 3R has a typical stacking order of AbA BcB CaC AbA, or the inverted AbA CaC BcB AbA.[159] The layers can also adopt a mixture of these stacking configurations, whereby, for example in a 3L sample, layers 1-2 obey 2H stacking, and layers 2-3 obey 3R stacking.[160] This means that a 3L 2H-3R sample could have the stacking configuration AbA BaB CbC, or AbA BaB AcA. The properties of 2H and 3R TMDs have been reported to be almost identical,[159] with little observable change in the high-frequency region of the Raman spectrum. However, recent reports indicate slight differences in band structures and absorption spectra between the two stacking types.[161, 162] This shows that further investigation into the identification and properties of these stacking configurations is important both for fundamental studies of these materials and for future studies in the emerging field of van der Waals heterostructures[3] where the stacking order of two dissimilar layers could change the electronic and optical properties[163, 164] of mechanically-assembled[165] or as-grown[166] heterostacks. In this thesis the stacking of the layers is 2H, unless explicitly stated otherwise.

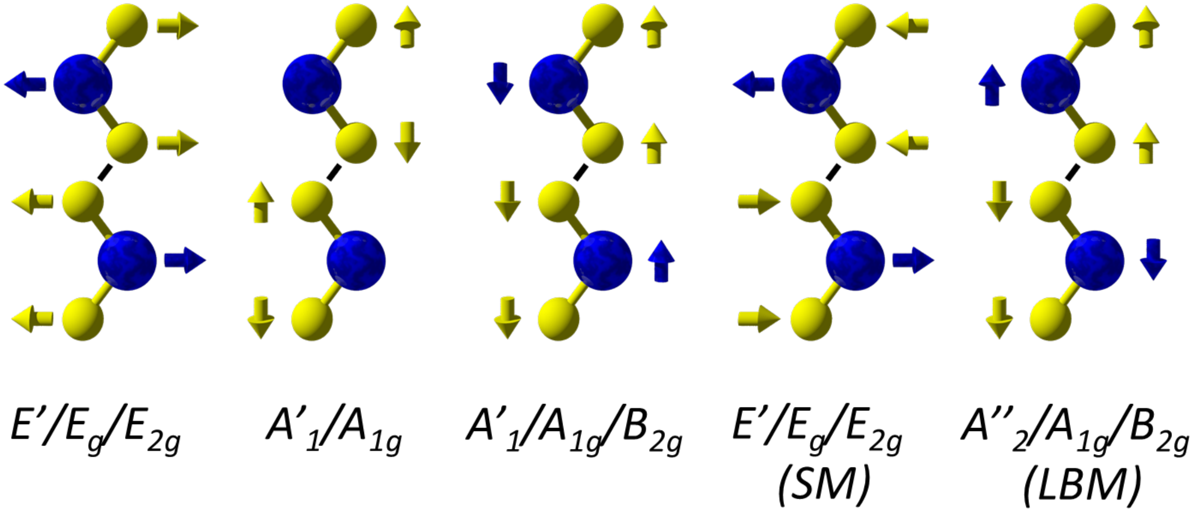

Figure 38
Schematic representation (ball and stick model) of Raman-active modes in TMDs with the relative odd/even/bulk symmetry label indicated for each mode. Blue balls represent transition metal atoms; yellow balls represent chalcogen atoms, with arrows showing direction of motion.

The Raman spectra of 2H and 3R semiconducting TMDs generally display two main characteristic vibrational modes, as discussed previously in Chapter 2, which are the $E'/E_g/E^1_{2g}$ and A'_1/A_{1g} first-order modes at the BZ centre, shown in Figure 38, that result from the in-plane and out-of-plane vibrations, respectively, of metal (M) and chalcogen (X) atoms.[72, 167, 168] As detailed in Chapter 2, different peak labels are used for different layer numbers due to the changing symmetry of the point group from D_{3h} (odd layer number) to D_{3d} (even layer number) to D_{6h} (bulk). These Raman-active modes have been shown to shift in position with number of layers,[58, 71, 75, 169] allowing mono- and few-layer MoS_2 and WS_2 crystals to be identified. However, for the transition metal diselenides, such as $MoSe_2$ and WSe_2, these changes in frequency for different layer numbers are not as dramatic (e.g. a shift of ~1 cm^{-1} in the A_{1g} peak from 2 to 3L $MoSe_2$),[169, 170] and may be below the instrumental spectral resolution of standard equipment. Furthermore, crystallite size,[82] doping and strain have been shown to significantly alter the Raman spectra of

TMDs. Previous reports have shown a red-shift and broadening of the A'_1/A_{1g} peak in MoS_2 with n-doping[81] and a blue-shift and enhancement of the A'_1/A_{1g} peak with p-doping.[105, 114] The Raman spectrum of MoS_2 is also highly sensitive to strain with the application of uniaxial strain resulting in the degeneracy of the $E'/E_g/E^1_{2g}$ mode being lifted,[171] whereas the introduction of localised wrinkles and folds has been shown to cause a red-shift of both A'_1/A_{1g} and $E'/E_g/E^1_{2g}$ modes.[172]

Investigation of the low-frequency SM and LBM has been suggested as a universal method of layer number determination in TMD materials,[74] due to the fact that the LBM vibrations are themselves out of plane and vary significantly as a function of layer number.[173] The relative atomistic motions of the SMs and LBMs in TMDs are illustrated in Figure 38, whereby the SM involves the in-plane motion of metal and chalcogen atoms, and the LBM involves the out-of-plane motion of metal and chalcogen atoms.[72] These SMs and LBMs are not present in single layers, but show a characteristic blue and red-shift, respectively as layer number increases from 2L to bulk.[158] Full measurement and analysis of these modes is desirable for a more comprehensive understanding of the mechanical and electrical properties of TMDs.[174]

The low-frequency SMs and LBMs have been extensively studied in graphene[158, 173] and have been reported for a number of mechanically exfoliated TMDs.[74, 174, 175] Unlike graphene, which consists of single atomic layers of carbon, TMD monolayers consist of three atomic layers of chalcogen/metal/chalcogen, resulting in a richer and more complex Raman spectrum. Therefore, a complete study on the low-frequency modes in TMDs is desirable to fully understand their properties and interlayer interactions.

5.3.1 MoS_2 Raman Mapping

In Figure 39(a), an optical image of CVD-grown MoS_2 on SiO_2/Si is shown. Multiple distinct layers are present, as indicated by the change in contrast. The layer numbers as determined following Raman characterisation are indicated in the image. In MoS_2, the in-plane ($E'/E_g/E^1_{2g}$) and out-of-plane (A'_1/A_{1g}) Raman peaks occur in the vicinity of ~385 and ~403 cm^{-1}, respectively. Figure 39(d) shows the evolution of Raman spectra (normalised to A'_1/A_{1g} peak intensity) extracted from 1-5L MoS_2, which display a characteristic red and blue-shift of the $E'/E_g/E^1_{2g}$ and A_1'/A_{1g} modes, respectively as the layer number increases.[71, 75] Peak intensity maps are presented in Figure 39(b) and (c), showing an increase in intensity of A'_1/A_{1g} and $E'/E_g/E^1_{2g}$ peaks as layer number increases from 1-5 layers, with a subsequent decrease as layer number increases towards bulk, attributed to optical interference occurring for the excitation laser and emitted Raman scattering.[71] The peak position maps for A'_1/A_{1g} and $E'/E_g/E^1_{2g}$ are shown in Figure 40, with Figure 40(a) and (b) showing clearly the red- and blue-shift in $E'/E_g/E^1_{2g}$ and A'_1/A_{1g} peaks, respectively, as layer number increases, allowing an initial assessment of layer number to be made. The plot of Raman shift position as a function of layer number is shown in Figure 40(c), to further emphasise the changes in Raman spectra with thickness. This assessment is supported by PL intensity maps of the same area, shown in Figure 39(e) and Figure 39(f), showing a maximum intensity of A1 excitons in monolayer regions, and an enhancement of B1 exciton intensity in multilayer regions respectively. The corresponding shift in PL position as layer number increases, reflecting the changing bandgap of MoS_2 with layer number, is illustrated in the peak position maps in Figure 40(d) and (e), which show the position of the A1 and B1 exciton. The extracted corresponding spectra in Figure 40(f) show the A1 and B1 excitonic peaks at ~680 and ~640 nm respectively, consistent with previous reports for CVD-MoS_2.[54, 90] The enhanced intensity in monolayers is due to their direct bandgap compared to few-layer flakes. The inset in Figure 40(f) shows the PL normalised to the maximum signal for each layer number, to further emphasise the changing PL (reflecting the changing electronic properties) with layer number. This highlights the evolution in peak position and change in A1:B1 exciton intensity ratio with changing layer thickness.

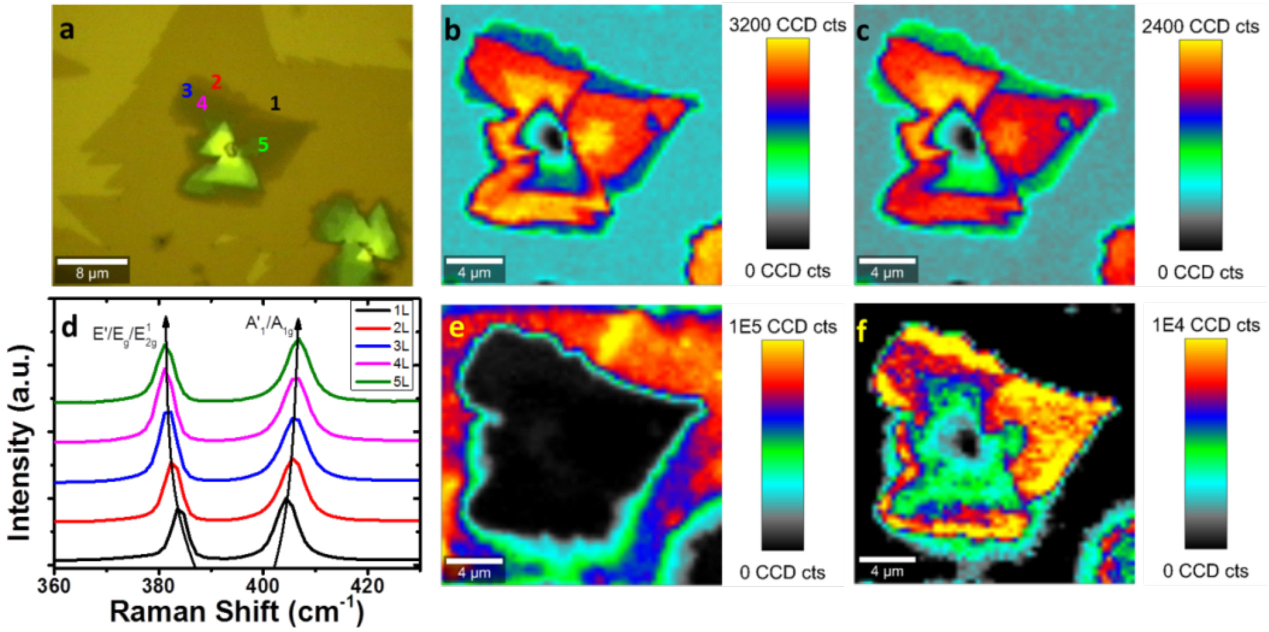

Figure 39

(a) Optical image of CVD-grown MoS_2 with layer numbers labelled (b) Peak intensity map of A'_1/A_{1g} (~403 cm^{-1}) high-frequency Raman mode (c) Peak intensity map of $E'/E_g/E^1_{2g}$ (~385 cm^{-1}) Raman mode (d) Raman spectra of 1-5L MoS_2 (e) Peak intensity map of A1 exciton PL peak (f) Peak intensity map of B1 exciton PL peak.

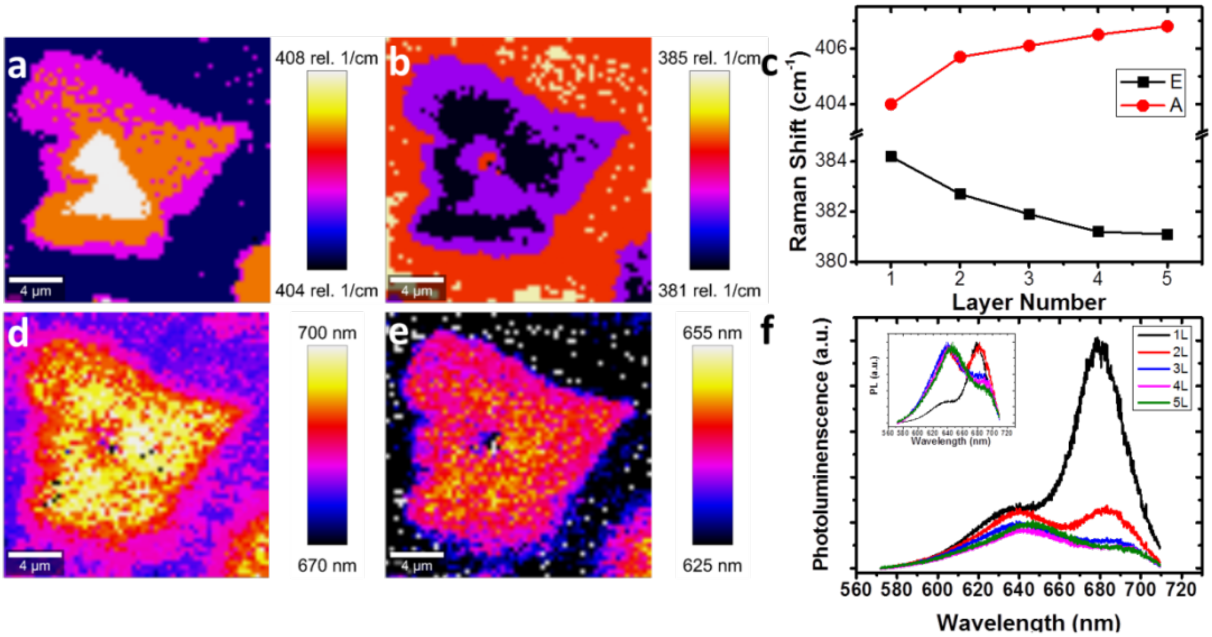

Figure 40

Additional Raman and PL analysis of MoS_2 crystals of different layer thickness extracted from the regions shown in Figure 39 previously. (a) Map of A'_1/A_{1g} mode position (b) Map of $E'/E_g/E^1_{2g}$ mode position (c) Plot of position of A'_1/A_{1g} and $E'/E_g/E^1_{2g}$ modes as a function of layer number. (d) Map of A1 exciton position (e) Map of B1 exciton position (f) PL spectra extracted from 1-5L regions corresponding to same areas as Raman spectra for each layer. Inset: Normalised version of the same spectra.

Figure 41 presents the low-frequency SMs and LBMs of MoS_2. Spectra of 1-5L MoS_2 are shown in Figure 41(a), in close agreement with previous measurements of mechanically exfoliated MoS_2.[74, 174] Figure 41(b to e) show peak intensity maps of SMs/LBMs for 2-5L MoS_2. There is some overlap in peak intensity maps, due to peaks for different layer numbers appearing at similar Raman shifts; however, the relative intensity of these modes provides a strong indication of layer number. While peak intensity maps allow a step-by-step assignation of layer number, this can be better visualised by generating a map of the position of maximum peak intensity in the low-frequency regime as shown in Figure 41(f). Such maps represent a clear and facile method of assigning the layer number present in MoS_2, by uniquely identifying the highest intensity SMs and LBMs present in 2-5L MoS_2 by their position in the range of 10-50 cm^{-1}, noting that 1L MoS_2 has no peaks in this region.

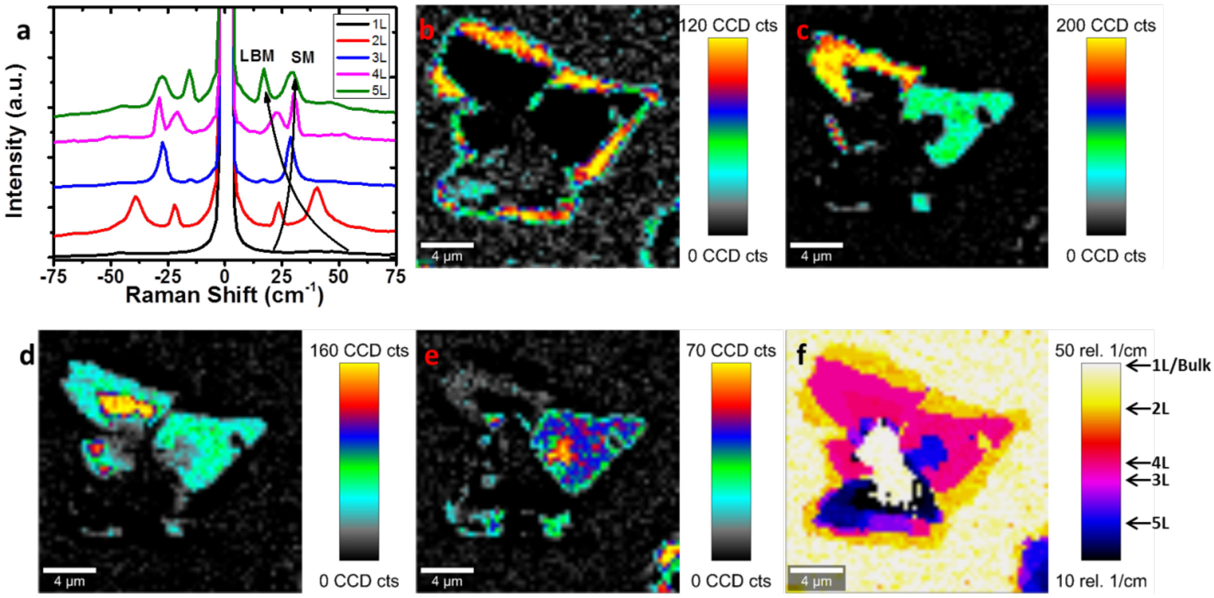

Figure 41

(a) Low-frequency Raman spectra of SMs and LBMs of 1, 2, 3, 4 and 5L MoS_2 (b) Peak intensity map of LBM mode for 2L MoS_2 at ~40 cm^{-1} (c) Peak intensity map of max SM/LBM for 3L MoS_2 at ~29 cm^{-1} (d) Peak intensity map of max SM for 4L MoS_2 at ~31 cm^{-1} (e) Peak intensity map of LBM for 5L MoS_2 at ~17 cm^{-1} (f) Map of position of maximum peak intensity in the region of 10-50 cm^{-1}.

5.3.2 $MoSe_2$ Raman Mapping

Raman analysis of CVD-grown $MoSe_2$ with a variety of layer numbers is shown in Figure 42. In $MoSe_2$, the in-plane ($E'/E_g/E^1_{2g}$) and out-of-plane (A'_1/A_{1g}) Raman-active modes occur in the vicinity of ~287 and ~240 cm^{-1}, respectively. The significant red-shift of peaks compared with MoS_2 occurs due to the larger mass of the selenium vs. sulfur atoms.[174] Similar to MoS_2, the in-plane ($E'/E_g/E^1_{2g}$) and out-of-plane (A'_1/A_{1g}) modes exhibit a red- and blue-shift, respectively, with increasing layer thickness. In Figure 42(a), an optical image of CVD-grown layers is shown. A Raman map of A'_1/A_{1g} (~240 cm^{-1}) peak intensity is shown in Figure 42(b). It is clear from these images that while the intensity varies significantly with thickness, following an initial jump from 1 to 2L, the A'_1/A_{1g} (~240 cm^{-1}) position does not change dramatically with layer number. A map of the $E'/E_g/E^1_{2g}$ (~287 cm^{-1}) intensity is shown in Figure 42(c). This Raman mode's intensity and position changes significantly from monolayer to bilayer, but shows no further significant change between 2, 3, and 4 layers, and is therefore not useful for layer number determination. Figure 42(d) shows spectra of 1 to 4L 2H $MoSe_2$ crystals extracted from different areas in Figure 42(a), which are in good agreement with previously reported spectra.[168, 170, 175] The intensity maximum and position maps of the $A'_1/A_{1g}/B^1_{2g}$ mode (~350 cm^{-1}) can also be considered. This mode is inactive in bulk material, but has previously been observed to become weakly Raman-active in bilayer and few-layer crystals due to the breakdown of translation symmetry.[168] To avoid confusion with other modes, this will henceforth be referred to as the B^1_{2g} mode. As this mode does not appear for monolayer $MoSe_2$, as shown in the peak intensity map in Figure 42(e), its absence (in combination with a characteristic PL signal) serves as a confirmation of monolayer presence. However, similar to $E'/E_g/E^1_{2g}$ (~287 cm^{-1}), it does not shift significantly in intensity or position for 2+ layers as shown in the map of B^1_{2g} position in Figure 43(d). A map of PL intensity is shown in Figure 42(f). The intense PL seen in certain areas serves as confirmation of monolayer presence, with some drop-off in intensity, as expected, in the regions of grain boundaries. The apparent lack of PL in other layers does not necessarily signify bulk behaviour – rather the signal for few-layer crystals is overshadowed by the massive PL of the monolayer.

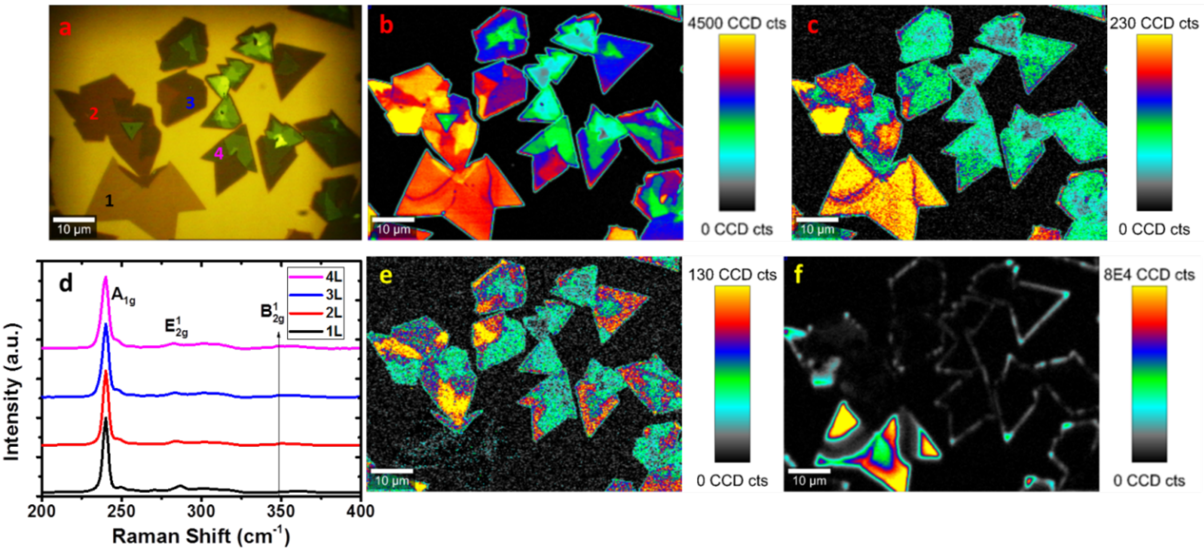

Figure 42

(a) Optical image of CVD-grown $MoSe_2$ with varying layer numbers (b) Peak intensity map of A'_1/A_{1g} (~ 240 cm^{-1}) Raman mode for $MoSe_2$ (c) Peak intensity map of $E'/E_g/E^1_{2g}$ (~287 cm^{-1}) Raman mode (d) Raman spectra of 1-5 L MoS_2 normalised to A'_1/A_{1g} mode intensity (e) Peak intensity map of B^1_{2g} (~350 cm^{-1}) mode (f) PL intensity map.

Peak position maps for A'_1/A_{1g} and $E'/E_g/E^1_{2g}$ modes are shown in Figure 43(a) and (b), respectively. In the peak position maps for A'_1/A_{1g} in Figure 43(a), negligible variation is seen over the areas mapped, with the exception of expected decreases in the positions of grain boundaries,[90] and variation at crystal edges, possibly due to doping or strain in these regions as has been reported for CVD-MoS_2.[63, 176] Figure 43(b) shows the peak position map for $E'/E_g/E^1_{2g}$, where a shift towards higher wavenumbers with decreasing layer numbers is observed. A slight blue-shift of $E'/E_g/E^1_{2g}$ is also seen at the edges of layers, likely due to edge and termination effects. Figure 43(c) shows a plot of Raman shift position for the $E'/E_g/E^1_{2g}$ and A'_1/A_{1g} modes as a function of layer number, with a significant red-shift observed for $E'/E_g/E^1_{2g}$ with increasing layer number, similar to MoS_2, but a less significant blue-shift in A'_1/A_{1g} with increasing layer number. Figure 43(d) shows the map of B^1_{2g} mode position. This illustrates that this mode does not appear for monolayer, and while it is present for 2+L it does not vary significantly in position. The map of PL position for $MoSe_2$ is shown in Figure 43(e), showing a shift in position at the edge of each crystal, similar to previous observations for TMDs.[57, 63] The general shift in PL position for different regions is further shown in Figure 43(f), which shows the PL spectra extracted for the layer number regions discussed previously. The PL peak for monolayer occurs as a single prominent maximum at a wavelength of ~800 nm, in line with previous reports of CVD and mechanically exfoliated $MoSe_2$.[168, 170] The shift in PL towards higher wavelengths (lower bandgaps) with increasing layer number is also consistent with previous reports.[168] Inset in Figure 43(f) shows the same PL spectra normalised to maximum PL intensity, in order to show clearly the shift in PL position with layer number.

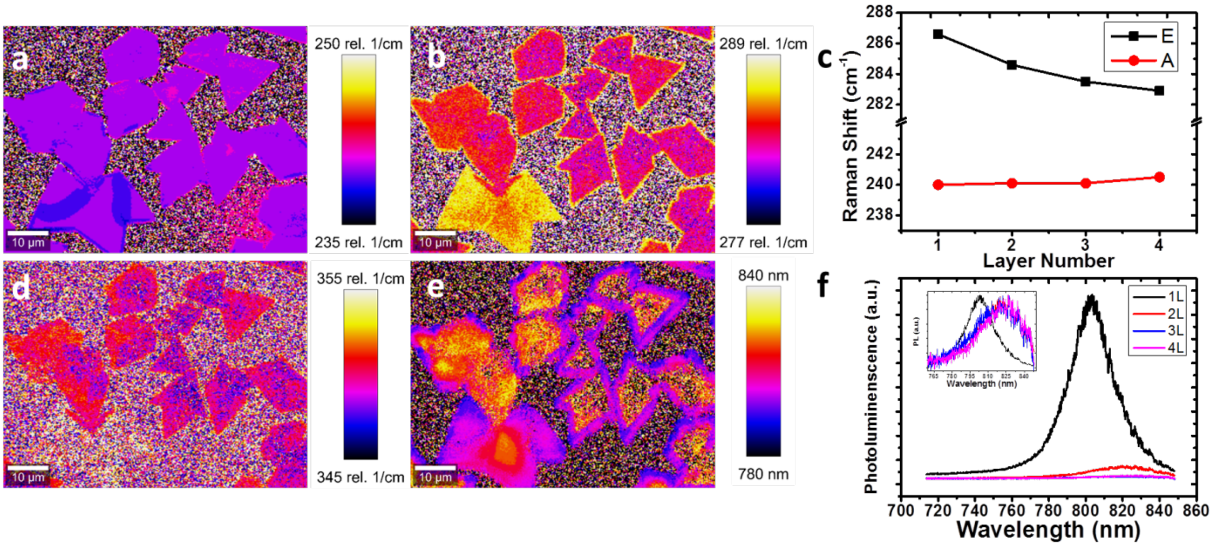

Figure 43

Raman and PL maps of $MoSe_2$ crystals of different layer thickness extracted from the regions shown in Figure 42 above. (a) Map of A'_1/A_{1g} peak position (b) Map of $E'/E_g/E^1_{2g}$ peak position (c) Plot of Raman shift for A'_1/A_{1g} and $E'/E_g/E^1_{2g}$ modes. (d) Map of B^1_{2g} peak position (e) Map of PL peak position (f) PL spectra of $MoSe_2$ crystals of different layer thickness extracted from the regions shown in Figure 42(a). Inset: Normalised version of the same spectra highlighting the evolution in peak position with changing layer thickness.

Low-frequency Raman modes in $MoSe_2$ will now be considered. Figure 44(a) shows spectra of 1 to 4L 2H-$MoSe_2$ which have been extracted from different areas marked in the optical image in Figure 42(a), and are in close agreement with spectra previously shown in the literature.[170] These spectra have been normalised to the intensity of the high-frequency A_{1g} mode, and offset for clarity, as have the rest of the $MoSe_2$ spectra in Figure 44.

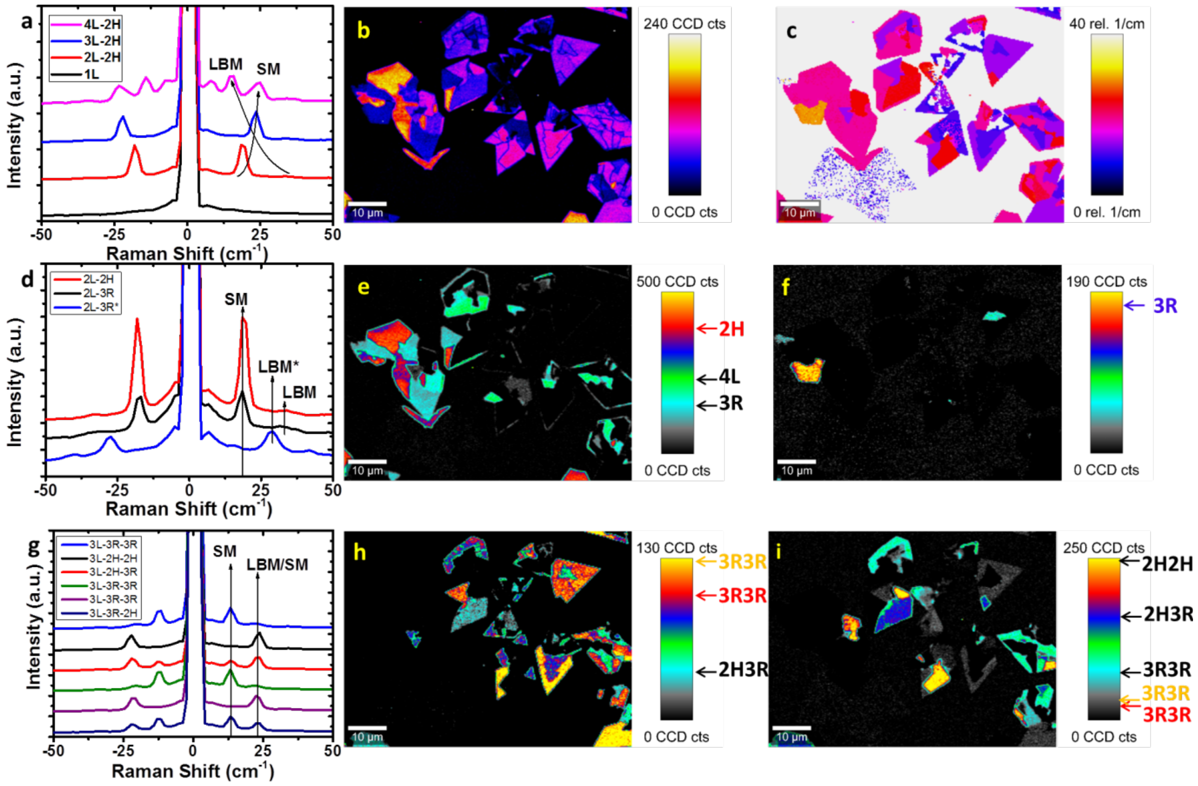

Figure 44

(a) Low-frequency Raman spectra of SMs and LBMs of 1, 2, 3, and 4L 2H $MoSe_2$ (b) Peak intensity map over the range 10-50 cm^{-1} (c) Map of position of maximum peak intensity of the low-frequency Raman modes in the range of 0-40 cm^{-1} (d) Low-frequency Raman spectra of SMs and LBMs of 2H and 3R stacking configurations in 2L $MoSe_2$ (e) Peak intensity map for 2L $MoSe_2$ SM at ~18 cm^{-1} (f) Peak intensity map for 2L $MoSe_2$ LBM at ~29 cm^{-1} (g) Low-frequency Raman spectra of SMs and LBMs of 2H and 3R combination stacking configurations for 3L $MoSe_2$ (h) Peak intensity map for 3L $MoSe_2$ at ~13 cm^{-1} (i) Peak intensity map for 3L $MoSe_2$ at ~24 cm^{-1}.

A Raman map of the maximum signal over the range 10-50 cm^{-1} is shown in Figure 44(b). Interestingly, this map shows fractures and splitting in areas where no change is discernible in the optical image and therefore further investigation into the low-frequency modes was warranted. By analysis of various regions that appeared to be the same thickness according to optical contrast, it was possible to extract different low-frequency Raman signals correlating to different combinations of 2H and 3R stacking of $MoSe_2$ layers. These different stacking configurations have previously been observed in CVD-grown transition metal diselenide layers and their formation attributed to the small difference in formation energy between the two different configurations.[160] It should be noted that there was no evidence of these different stacking configurations in the CVD-grown MoS_2 presented here, with all areas probed displaying a purely 2H signal. However, recent reports have emerged on the Raman signatures of mechanically exfoliated 2H and 3R MoS_2 indicating significant differences in low-frequency modes for each polytype, similar to what is observed here for $MoSe_2$.[177] In Figure 44(c), a map of position of peak intensity maximum in the low-frequency region is shown. Study of the differences in intensity maximum in Figure 44(b) and the position of this intensity maximum for each layer shows that there is no direct overlap in each – rather, some areas have peaks of maximum intensity in the same position but of different intensity, while others have peaks of similar intensity but in different areas. To explain this observation, the low-frequency spectra for each layer number will be examined. In Figure 44(d), low-frequency Raman spectra for different regions of 2L MoS_2 are shown, corresponding to 2H (max at 18 cm^{-1}), 3R (max at 18 cm^{-1}, but significantly lower in relative intensity), and 3R* (max at 29 cm^{-1}). The difference between 3R (max at 18 cm^{-1}) and 3R* (max at 29 cm^{-1}) is attributed to one being 3R and the other being the vertically flipped 3R, labelled here as 3R* for clarity. This was previously predicted to exist,[160] and to interact differently with incoming photons. The intensity maximum for 2H and 3R (18 cm^{-1}) is shown in Figure 44(e), which shows (with some overlap with peaks present in 4L) the areas where these peaks are present. The difference in intensity between 2H and 3R here is consistent with previous reports.[160] Additionally, as shown in Figure 44(f), a previously predicted Raman mode at ~29 cm^{-1}, attributed to the A_1 mode in the 3R* stacking configuration, is observed.[160] Similar evidence for different stacking configurations is seen in the 3L low-frequency Raman spectra in Figure 44(g), where it is possible to identify a variety of 3L stacking configurations, including 2H-2H, 2H-3R, and 3R-3R. The trends in intensity for the peaks at ~13 cm^{-1} and ~24 cm^{-1} are clear when the peak intensity maps are considered. In Figure

44(h), a peak intensity map of the SM at ~13 cm^{-1} is shown, which is present for 3R-3R stacking, but also present at higher intensities as the SM mode in 2H-3R stacking, where it appears in parallel with another SM mode at 24 cm^{-1}. Therefore, the relative intensity of this mode at ~13 cm^{-1} can be used to distinguish between 3R-3R and 2H-3R stacking, as labelled on the intensity scale bar in Figure 44(h), with further verification of the 2H-3R mode afforded by the presence of a SM/LBM overlap peak at ~24 cm^{-1}, the intensity of which is mapped out in Figure 44(i). This peak is highest in intensity in 2H-2H stacking, as is expected for pristine mechanically exfoliated 2H crystals,[175] and decreases as stacking configuration goes from 2H-2H to 2H-3R to 3R-3R. This is logical when considering the decreasing interlayer interactions and force constants present in 3R stacking in comparison to 2H stacking. The respective intensities for the different stacks, as shown in Figure 44(i), indicate clearly that different intensities are present for this peak in different areas, allowing one to distinguish between 2H-2H, 2H-3R and different 3R-3R stacking configurations. Evidence for changing stacking configurations is seen in the 4L low-frequency Raman spectra in Figure 45, where it is possible to identify a variety of 4L stacking configurations, which has been labelled A-H. The characteristic modes at ~11 cm^{-1}, 18 cm^{-1} and 24 cm^{-1} are mapped in Figure 45(a), (b) and (c), with labels for each spectrum extracted on the intensity scale for each. To facilitate identification of the layers in this area, an optical image of Figure 42(a) with enhanced contrast applied is shown here in Figure 45(d). By analysis of the Raman maps in Figure 45(a)-(c), it was possible to extract spectra A-H shown in Figure 45(e).

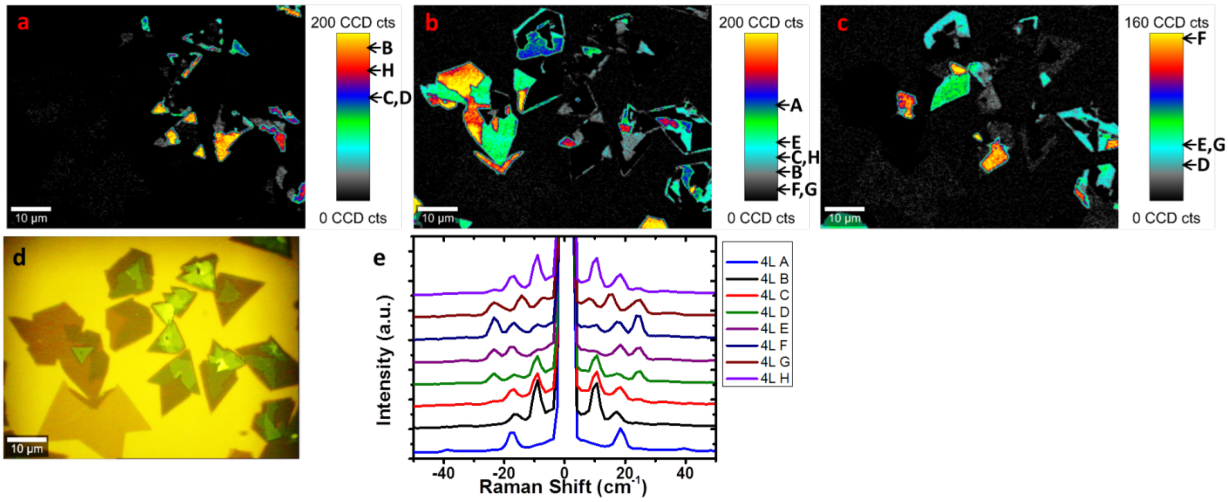

Figure 45

Additional Raman mapping of $MoSe_2$ crystals of different layer thickness extracted from the regions shown in Figure 42(a) previously. (a) Peak intensity map for 4L $MoSe_2$ SM at ~11 cm^{-1} (b) Peak intensity map for 4L $MoSe_2$ SM at ~18 cm^{-1} (c) Peak intensity map for 4L $MoSe_2$ SM at ~24 cm^{-1} (d) Optical image of the region of $MoSe_2$ crystals mapped with additional contrast applied (e) Spectra of 4L $MoSe_2$ crystals of different stacking orientations extracted.

In Figure 46, high-frequency Raman spectra for different stacking configurations are shown for the same regions for which each low-frequency spectrum was extracted. These spectra have been normalised to the A'_1/A_{1g} peak and offset for clarity. In Figure 46(a), the 2L-2H, -3R and -3R* spectra are shown for the high-frequency Raman spectral region, with no significant change in the spectra discernible between different stacking configurations. In Figure 46(b), the 3L spectra for differing stacking configurations are shown, with no major change in the spectra between different stacking configurations, however a small relative intensity change in B^1_{2g} mode can be observed in some of the 3L-3R-3R configurations. In Figure 46(c), the 4L spectra for differing stacking configurations are shown, with no observable change in the spectra between stacking configurations.

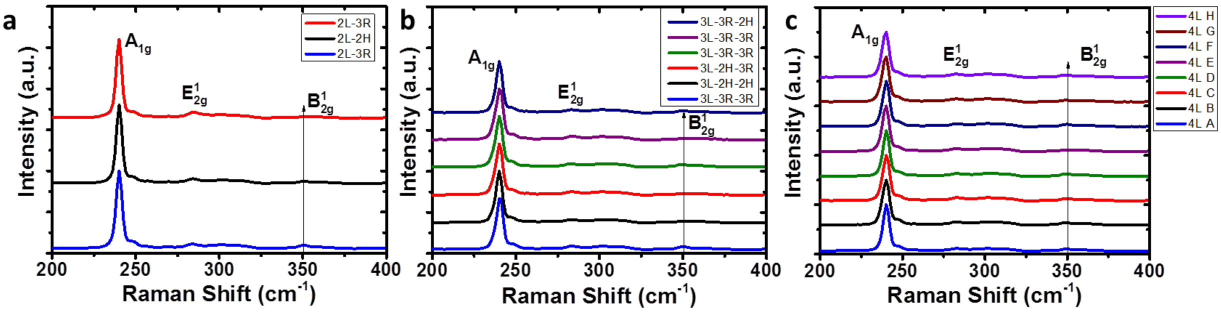

Figure 46

Comparison of high-frequency Raman spectra for different stacking configurations within each layer number for (a) 2L (b) 3L (c) 4L.

The use of low-frequency Raman intensity maps serves to highlight the ubiquitous nature of the different stacking configurations in CVD-grown $MoSe_2$, which would not be readily apparent in comparing standard high-frequency spectra of different crystals, which show little change between 2H and 3R stacking configurations,[159] as shown in the extracted spectra in Figure 46. Low-frequency Raman mapping can distinguish between different stacking configurations rapidly and non-destructively, allowing TMDs in different stacking configurations to be identified and studied without the need for high-resolution imaging *via* electron microscopy.[88] The peak positions of SMs and LBMs observed here are in good agreement with previously observed low-frequency modes in mechanically exfoliated 2H $MoSe_2$[175, 178] and CVD-grown $MoSe_2$.[160]

Much of the analysis here relies on the identification of layer number or stacking polytype using Raman spectroscopy. Therefore, it was deemed necessary to verify layer number of TMDs using a separate technique. AFM was used as an independent means of measuring the layer thickness, in order to verify the layer-number assignment from Raman spectroscopy and also to show that there was no change in thickness for different stacking polytypes of the same layer thickness. The AFM scans shown here were taken by Dr. Toby Hallam. Figure 47 depicts AFM analysis of two $MoSe_2$ regions analysed previously. In Figure 47(a) and (b), the maps of low-frequency maximum and position of maximum intensity have been reproduced from Figure 44, with the relevant optical image shown in Figure 47(c). Figure 47(d) shows an AFM image of this region with layer-thickness assignments from Raman spectroscopy overlaid; this has been rotated slightly in order to facilitate a direct comparison between AFM and Raman images. Figure 47(e-h) reproduce the low-frequency maps shown in Figure 44(e), (f), (h) and (i), respectively. The centre triangle in Figure 47(g) is present due to overlap of peaks at this frequency for 3L with those of higher layer numbers. Figure 47(i) shows an AFM height map over this crystal region, with several height profiles marked. These correspond to height profiles 1-5 in Figure 47. Height profile 1 shows a decrease in layer number from 3L to 2L, as expected. Height profile 2 shows no change in layer number across a 3L region, which contains several different stacking polytypes according to low-frequency Raman analysis. Height profile 3 shows an increase in layer number from a 2L region to a 3L region. Height profile 4 shows an increase in layer number from 0L (background) to a 2L region. Height profile 5 shows no increase in height across 2L regions of different stacking polytype, as shown through low-frequency Raman analysis, and then an increase on going from a 2L region to a 3L region, as expected. The height differences between different layers in each instance are labelled on each profile, and range from 0.9-1 nm per layer, comparable to previous reports of CVD-grown TMDs.[179, 180] Decorative contamination can be seen in the AFM scans, which has been observed previously for CVD-grown TMDs.[90, 166] This is likely due to preferential particle adsorption at the growth front, or atmospheric contamination post growth. Some wrinkles are also present in the AFM image, between the 2L-2H and 2L-3R regions. These are likely caused by strain in the MoS_2 layers,[181] similar to effects which have previously been studied in graphene.[182] These height profiles support the layer numbers previously identified by Raman spectroscopic measurements and further show the lack of any measurable change in height across different stacking polytypes within a given layer number. This confirms that the changes observed in the Raman spectra cannot be attributed to changing layer number, and support the previous assertions that different stacking orders are present within the layers. Further, the AFM scans illustrate that low-frequency Raman spectroscopy can identify features which cannot be observed using AFM alone.

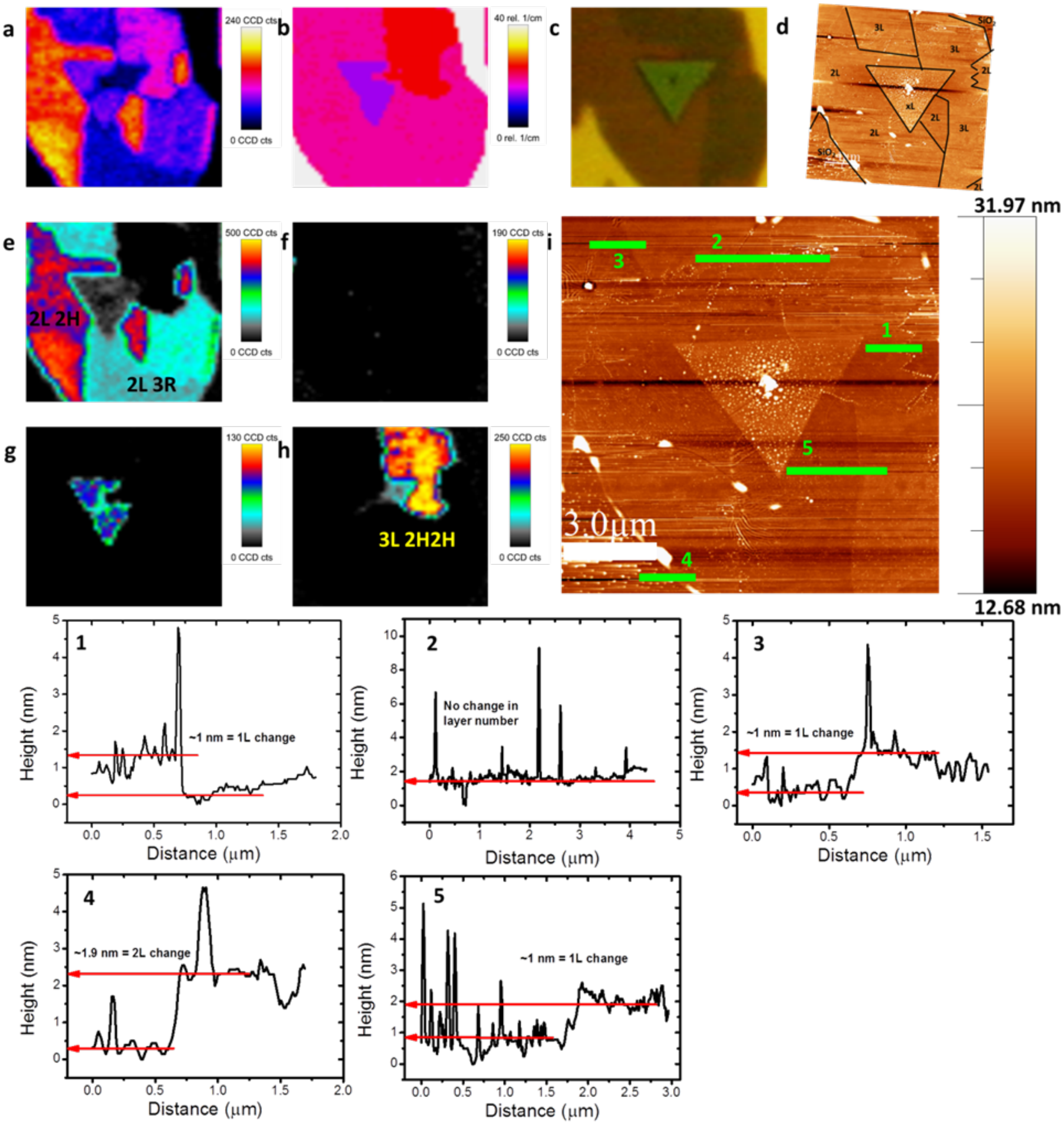

Figure 47

(a) Peak intensity map over the range 10-50 cm^{-1} (b) Map of position of maximum peak intensity of the low-frequency Raman modes in the range of 0-40 cm^{-1} (c) Optical image of CVD-grown MoSe$_2$ crystal from the area shown in Figure 42 and Figure 44. (d) AFM scan with layer numbers overlaid as identified by Raman spectroscopy (e) Peak intensity map for 2L MoSe$_2$ SM at ~18 cm^{-1} (f) Peak intensity map for 2L MoSe$_2$ LBM at ~29 cm^{-1} (g) Peak intensity map for 3L MoSe$_2$ at ~13 cm^{-1} (h) Peak intensity map for 3L MoSe$_2$ at ~24 cm^{-1} (i) AFM height scan over MoSe$_2$ crystal with height profiles 1-5 labelled in overlay.

5.3.3 WSe_2 Raman Mapping

A sample of CVD-grown WSe_2 with a variety of layer numbers present is shown in Figure 48(a). The WSe_2 Raman spectrum displays the in-plane (E'/E_g) and out-of-plane (A'_1/A_{1g}) modes typical for layered TMDs. Under the experimental conditions used here, these appear as a single overlapping peak at ~250 cm^{-1} in mono- and few-layer WSe_2. In the case of resonant excitation conditions, as applies when using a 532 nm excitation laser in resonance with the A' exciton peak of WSe_2,[83, 183] the *2LA(M)* phonon also appears. This is a second order resonant Raman mode that occurs due to *LA* phonons at the M point in the BZ,[169] similar to the case of MoS_2 and WS_2 in resonance.[58, 147, 184] Figure 48(d) shows spectra of 1 to 3L WSe_2 extracted from different areas marked in Figure 48(a), which are in agreement with previous studies.[160, 175] A peak intensity Raman map of the peak at ~250 cm^{-1} is shown in Figure 48(b), with the corresponding position map in Figure 49(a). This peak is a combination of contributions from the A'_1/A_{1g} and $E'/E_g/E^1_{2g}$ modes that coincidentally overlap at this Raman shift. This mode shows a decrease in intensity with layer number, and a slight shift in position as shown and discussed in Figure 49(a). The changing intensity of this peak between the two bilayer regions, as labelled on the optical image, suggests some change in stacking configuration, with one region displaying a higher intensity than the other.[160] This is likely due to a decrease in in-plane contributions due to the decreasing magnitude of Raman tensors in 3R symmetry contributions, but high-frequency modes alone are not sufficient to assign a definitive stacking configuration to each region. The labels shown on the optical image will be discussed in the low-frequency analysis below. A Raman map of the *2LA(M)* mode (~260 cm^{-1}) intensity is shown in Figure 48(c), with the corresponding position map in Figure 49(b). The *2LA(M)* mode's intensity changes significantly from monolayer to bilayer, but shows no further significant change for 3L. It is clear that this mode, similar to the peak at 250 cm^{-1}, is also more intense for one bilayer region than another. The relative intensity of *2LA(M)* increases with respect to the A'_1/A_{1g} and $E'/E_g/E^1_{2g}$ combination peak, however, the overall intensity decreases sufficiently for this not to be apparent in the peak intensity maps. The B_{2g} (~310 cm^{-1}) peak intensity map is shown in Figure 48(e), with the corresponding peak position map shown in Figure 49(d). This mode, similar to the case for $MoSe_2$, is inactive in bulk material, but becomes Raman-active in few-layer samples.[168] However, the absence of a discernible change in the intensity or position for 2-3 layers means it is of little use for layer-number analysis. This mode is most intense in the case of one 2L stacking configuration, which is tentatively attributed to increased interlayer interactions in ideal (likely 2H stacking) in comparison to other (3R) configurations. The brightest areas in the PL intensity map in Figure 48(f) signify the presence of monolayers. This is confirmed by the extracted PL spectra and position map shown in Figure 49(c) and (e), respectively. As layer number increases, the PL position shifts to higher wavelengths, and decreases in intensity, as is expected due to the change in band structure.[7, 147] No significant change in PL intensity or position is seen between the two different bilayer regions.

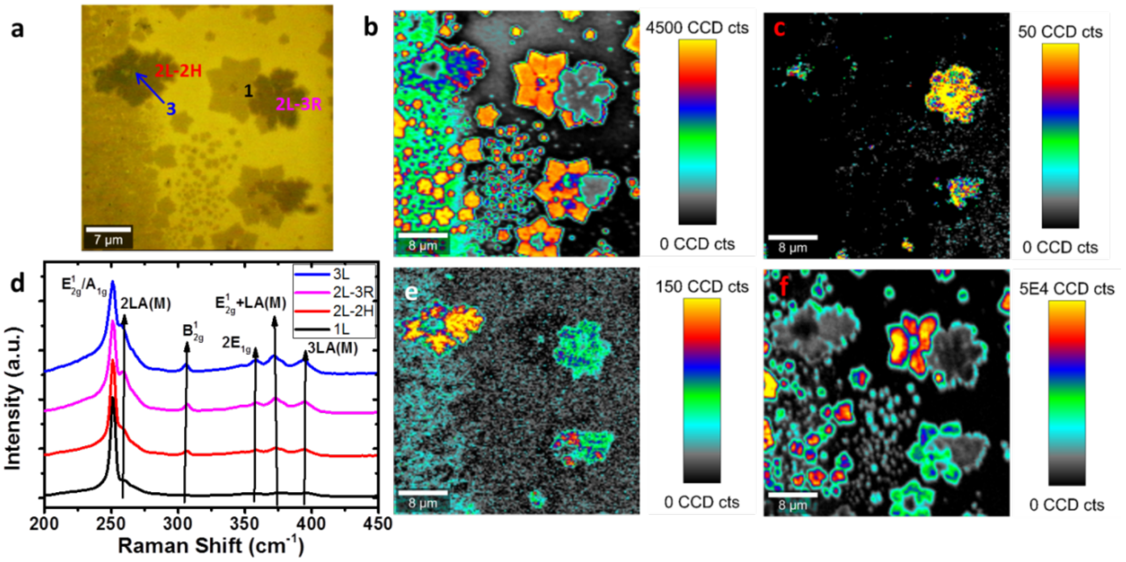

Figure 48
(a) Optical image of CVD WSe_2 with varying layer numbers (b) Peak intensity map of A'_1/A_{1g} and $E'/E_g/E^1_{2g}$ overlapping modes (~250 cm^{-1}) (c) Peak intensity map of *2LA(M)* peak (~260 cm^{-1}) (d) Raman spectra of 1L, 2L-2H, 2L-3R and 3L-2H WSe_2 (e) Peak intensity map of $A'_1/A_{1g}/B_{2g}$ (~310 cm^{-1}) Raman mode (f) PL intensity map.

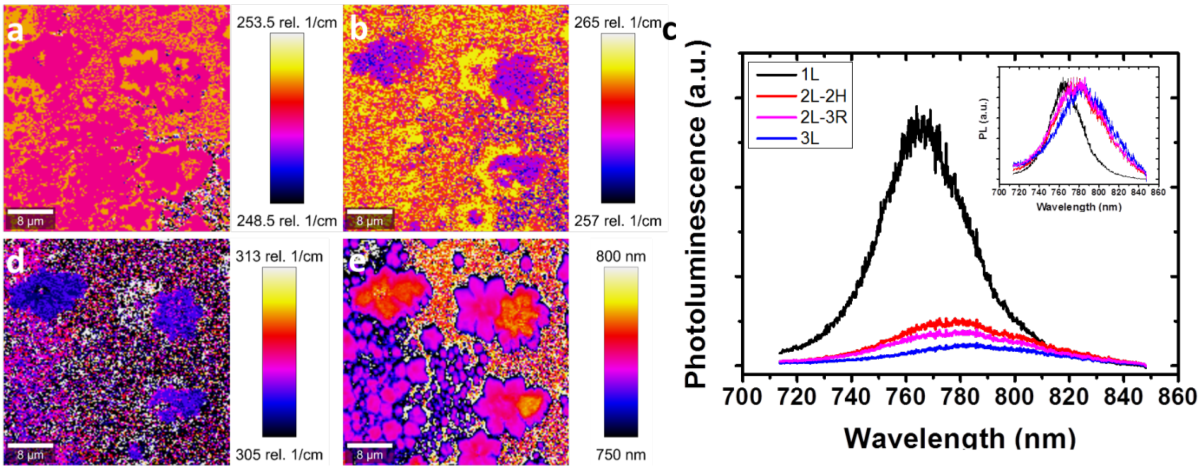

Figure 49

Raman and PL maps of WSe_2 crystals of different layer thickness extracted from the regions shown in Figure 48 above. (a) Map of A'_1/A_{1g} and $E'/E_g/E^1_{2g}$ overlapping peak position (b) Map of *2LA(M)* peak position (c) PL spectra of WSe_2 crystals of different layer thickness extracted from the regions shown in Figure 48. Inset: Normalised version of the same spectra highlighting the evolution in peak position with changing layer thickness. (d) Map of B^1_{2g} peak position (e) Map of PL position.

The peak position map for the A'_1/A_{1g} and $E'/E_g/E^1_{2g}$ overlapping mode is shown in Figure 49(a), with no discernible differences noted between different layer numbers. By comparison of the peak intensity map in Figure 48(b) with the peak position map in Figure 49(a), it can be seen that this peak position red-shifts to lower wavenumbers as layer number increases from 1 to 2+ layers, before blue-shifting to higher wavenumbers as layer number approaches bulk values. This can be attributed to the enhancement of $E'/E_g/E^1_{2g}$ mode as layer number initially increases from 1 to 2+ layers, followed by the domination of the out-of-plane A'_1/A_{1g} mode as more layers contribute in bulk-like regions, as is indicated in the spectra in Figure 48(d). The *2LA(M)* mode peak position map is shown in Figure 49(b), with a notable blue-shift between mono- and few-layer samples – however, this may simply be due to the enhanced relative intensity of the *2LA(M)* mode to the A'_1/A_{1g} and $E'/E_g/E^1_{2g}$ overlapping mode with increasing layer number. The PL position for monolayer appears at a wavelength of ~765 nm consistent with those previously reported for CVD-grown[185, 186] and mechanically exfoliated WSe_2,[168, 186, 187] showing an expected increase in wavelength with increasing layer number.

The low-frequency Raman modes of WSe_2 are shown in Figure 50. Figure 50(a) shows spectra of 1 to 3L WSe_2 SMs and LBMs, which have been extracted from different areas, as marked in the optical image in Figure 48(a), and are in close agreement with spectra previously reported.[160, 175] A clear decrease in intensity of the SM from 2L-2H to 2L-3R stacking is observed, highlighting that a change in stacking order has occurred. A corresponding increase in the LBM for 2L-3R stacking is also observed, similar to what was discussed previously for $MoSe_2$. The low-frequency peaks shown here agree with previous reports of different stacking configurations of 2L WSe_2.[160] A Raman map of the 2L-2H SM (~17 cm^{-1}) intensity is shown in Figure 50(b), which shows (with some overlap from peaks present in different layers) the areas where 2L-2H coverage is present. Raman intensity maps are also shown here for the 2L-3R LBM (~27 cm^{-1}) and the 3L-2H SM/LBM peak overlap (~21 cm^{-1}) in Figure 50(c) and (d), respectively. The lack of overlap of the layer regions in Figure 50(b), (c) and (d) emphasises the differences in the spectra of each stacking configuration in the low-frequency region. This is further shown in the map of maximum intensity position for the low-frequency region in Figure 50(e), where the measurement of peak position over the range of 10-40 cm^{-1} allows for clarification of each layer number and stacking order from a single Raman map.

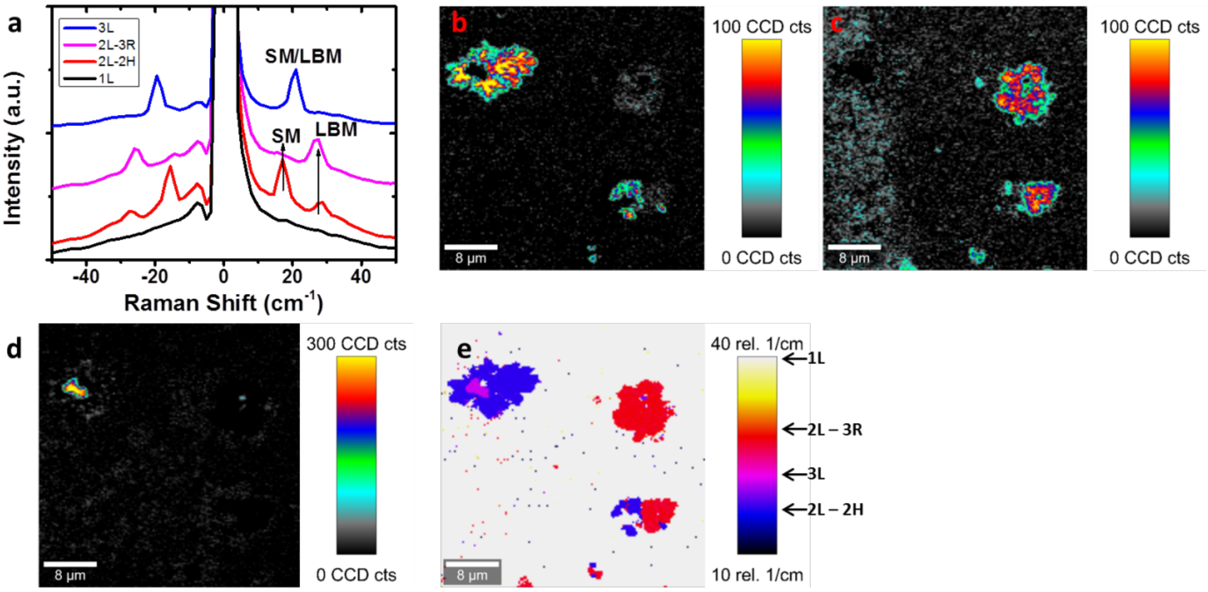

Figure 50

(a) Low-frequency Raman spectra of SMs and LBMs of 1, 2 and 3L WSe_2 (b) Peak intensity map of SM mode for 2L-2H WSe_2 at ~17 cm^{-1} (c) Peak intensity map for 2L-3R WSe_2 at ~27 cm^{-1} (d) Peak intensity map of SM/LBM mode for 3L-2H WSe_2 at ~21 cm^{-1} (e) Map of position of maximum peak intensity of the low-frequency Raman modes in the range of 10-40 cm^{-1}.

5.3.4 WS_2 Raman Mapping

A sample of CVD-grown WS_2 with a variety of layer numbers present is shown in Figure 51(a). The WS_2 Raman spectrum with an excitation wavelength of 532 nm is characterised by the $E'/E_g/E^1_{2g}$ and A'_1/A_{1g} modes at ~355 cm^{-1} and 417 cm^{-1}, respectively, and the resonant *2LA(M)* phonon mode at ~352 cm^{-1}, similar to that discussed previously for WSe_2. The resonance mode appears here due to the 532 nm laser wavelength used being in resonance with the B exciton peak of WS_2.[83, 183, 184] Resonant Raman spectroscopy is a powerful tool in the study of exciton-phonon interactions in 2D materials; through careful selection of the excitation wavelength certain modes can be enhanced and additional resonant contributions such as the *2LA(M)* mode observed.[188] A Raman map of intensity of the peak centred at ~352 cm^{-1} is shown in Figure 51(b), with the corresponding peak position map in Figure 52(a). This peak is a combination of contributions from the resonant *2LA(M)* and $E'/E_g/E^1_{2g}$ modes that coincidentally overlap at this Raman shift.

This peak is most intense in monolayer crystals, correlating to the PL map in Figure 51(e). A Raman map of the A'_1/A_{1g} mode intensity is shown in Figure 51(d), with the corresponding peak position map shown in Figure 52(b). The Raman spectrum of these layers is shown in Figure 51(c), with the spectra normalised to the peak at 352 cm^{-1} and offset for clarity. This shows changing behaviour from monolayer to few-layer crystals that is consistent with previous reports.[58, 189]

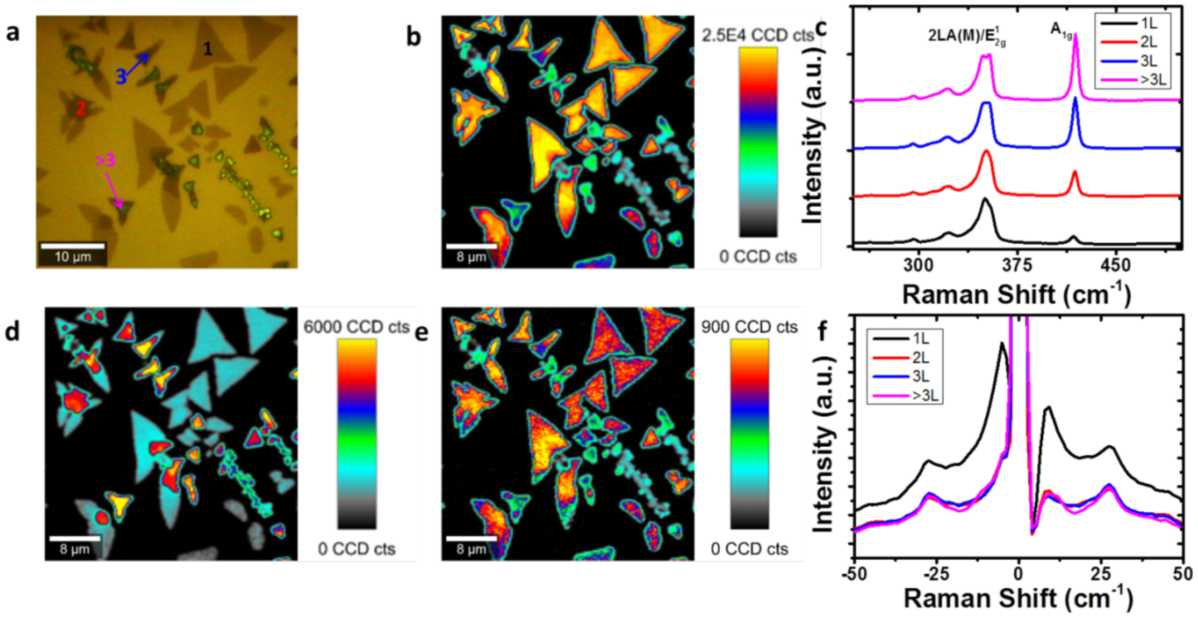

Figure 51
(a) Optical image of CVD WS_2 with varying layer numbers (b) Peak intensity map of $2LA(M)+E'/E_g/E^1_{2g}$ (~352 cm^{-1}) (c) Raman spectra of 1, 2, 3, and >3L WS_2 in the high-frequency region (d) Peak intensity map of max A'_1/A_{1g} peak (~417 cm^{-1}) (e) Peak intensity map of low-frequency resonance mode at 27 cm^{-1} in WS_2 (f) Raman spectra of 1, 2, 3, and 4L WS_2 in the low-frequency region.

While for MoS_2, $MoSe_2$ and WSe_2 the practicality of low-frequency Raman spectroscopy for assessment of layer-number and stacking orientation has been highlighted, in the case of WS_2 the possible presence of resonant modes in the low-frequency region of the Raman spectrum will now be discussed. Low-frequency Raman spectra of WS_2 regions of different layer thickness are shown in Figure 51(f). A peak at ~27 cm^{-1} is observed for all layer numbers, essentially obscuring SMs and LBMs at the Raman excitation wavelength used (532 nm). This peak is most intense in monolayer, as can be seen by the map in

Figure 51(e). A recent report has shown similar behaviour in the low-frequency region of the Raman spectrum of MoS_2 probed with a 633 nm excitation laser[190] and attributed this to strong resonance with excitons or exciton-polaritons, while previous reports have attributed this resonant Raman process to be reflective of a subtle splitting in the conduction band at *K* points.[191] This new peak in WS_2 is assigned tentatively as a *LA(M)* related mode, due to the peak intensity maps appearing almost identical in relative intensity to the *2LA(M)* peak intensity map shown in Figure 51(b). It should be noted that these resonance effects are not seen in WSe_2, with the laser wavelength used (532 nm), as this is only in resonance with the A' split exciton peak, and not an exciton absorption peak as is the case for WS_2.[83] This peak is seen in WS_2 for all layer thicknesses measured and while it is most intense in monolayer it does not vary significantly in intensity for other layer numbers. To further strengthen the link between this newly observed peak and the resonant modes, a comparison between Figure 52(c), a peak intensity map of the *LA(M)* mode, and the low-frequency resonance peak in Figure 51(e) shows that these correlate in relative intensity. It is suggested that further exploration of WS_2 low-frequency modes with multiple wavelengths would confirm this assignment, as has held true for MoS_2.[190, 191] The map of low-frequency resonance peak position in Figure 52(d) shows no change in the position of this peak with layer number, in stark contrast to the SM and LBM changes in position expected for TMDs. This further indicates that this peak must have a different origin to the SMs and LBMs generally studied for 2D materials.

A map of peak position for the overlapping *2LA(M)* and $E'/E_g/E^1_{2g}$ peak is shown in Figure 52(a). A red-shift in position of maximum intensity with increasing layer number is evident, likely due to enhanced contributions with increasing layer number from the $E'/E_g/E^1_{2g}$ mode at a higher Raman shift than *2LA(M)*. A position maximum map of the A'_1/A_{1g} mode is shown in Figure 52(b). A blue-shift in position of maximum intensity is clear as layer number increases. This is due to stronger interlayer contributions to the phonon restoring forces as layer number increases, resulting in a stiffening of the out-of-plane A'_1/A_{1g} mode, as the vibrations of this mode are more strongly affected by forces between the layers.[58] A peak intensity map of the zone-edge *LA(M)* phonon[58] is shown in Figure 52(c), with the corresponding spectra shown in Figure 52(h), which have been normalised to the 2LA(M) mode and offset for clarity. It is clear that this *LA(M)* mode has strongest intensity in monolayer crystals, with a negligible change in position with increasing layer number, and its relative intensity can be compared to that of the low-frequency resonance peak as discussed previously.

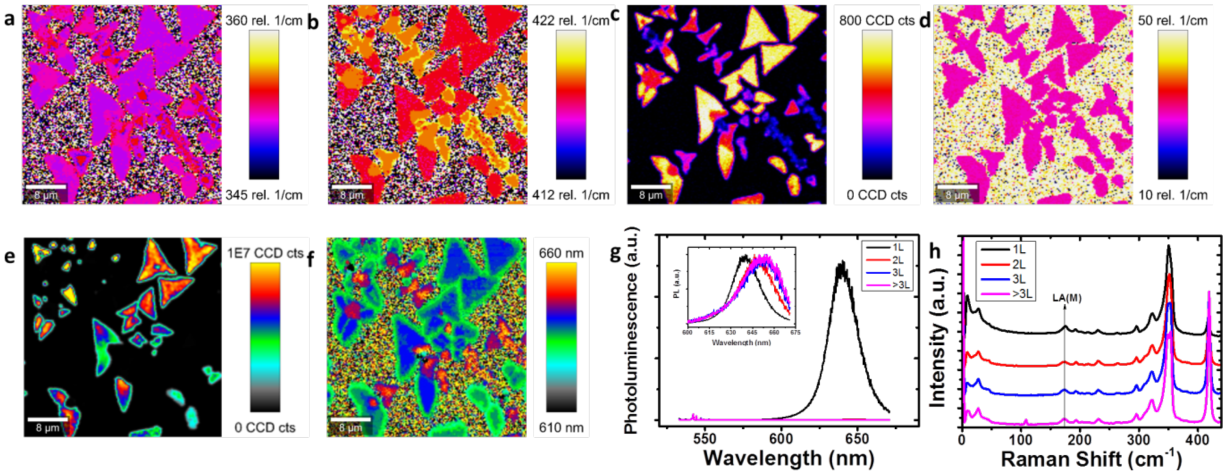

Figure 52

Additional Raman and PL mapping of WS_2 crystals of different layer thickness extracted from the regions shown in the optical image in Figure 51. (a) Map of $2LA(M)$ and $E'/E_g/E^1_{2g}$ overlap peak position (b) Map of A'_1/A_{1g} peak position (c) Map of *LA(M)* mode intensity (d) Position map of low-frequency peak at ~27 cm^{-1} (e) PL intensity map (f) Map of PL peak position (g) Corresponding PL spectra of 1, 2, 3 and 3+L WS_2. Inset shows plots normalised to PL intensity (h) Spectra of 1, 2, 3 and 3+L WS_2 centred on the *LA(M)* mode.

The remarkable PL in WS_2 monolayers is evident in the PL intensity map and the PL spectra in Figure 52(e) and (g) respectively. The apparent absence of PL in this map for 2+ layers is simply due to the relative intensity of the PL in 2+ layers being dwarfed by the emission from the monolayer crystals, where the intensity ratio of PL to $2LA(M)/E^1_{2g}$ is ~25. The presence of PL in 2+ layers can be seen in the graph inset in Figure 52(g), where the PL is normalised to intensity. Further changes in PL between mono and few-layer films are evident in the map of PL peak position in Figure 52(f), which demonstrates the position shift from ~640 nm for monolayers to ~650 nm for few layers, as is expected as the addition of layers causes shifting of the band structure towards a smaller and more indirect bandgap.

5.4 Summary

A comprehensive study of Raman scattering in CVD-grown mono- and few-layer MoS_2, $MoSe_2$, WSe_2 and WS_2 has been presented. Phonon modes for in-plane and out-of-plane vibrations show thickness dependent intensities and positions in both the high- and low-frequency regions. The general peak shift trends are similar for all materials studied due to their similar lattice structures, where a stiffening (blue-shift) is observed in SMs, while a softening (red-shift) is observed in LBMs, with increasing layer number. However, the intensity dependencies and Raman shifts vary in each material due to the different atomic masses of the metal/chalcogen in each crystal type, and due to the stacking order of the layers. The determination of layer number via systematic low-frequency mode mapping is a significant result in the analysis of TMD thin films, as is the stacking configuration determination, which has been shown here by Raman mapping. Furthermore, a new peak is reported, observable in resonance conditions at ~27 cm^{-1} in WS_2 crystals.

6 Raman Spectroscopy of Suspended MoS_2

This chapter studies the Raman spectrum of freely-suspended CVD-grown MoS_2. As-grown CVD-MoS_2 was transferred to holey substrates using a polymer support technique, allowing Raman spectra of freely suspended MoS_2 to be measured. Significant differences in suspended and supported MoS_2 were observed, which are attributed to strain in the MoS_2 suspended over the holey regions in the substrate.

6.1 Introduction

While much research has been carried out on the characterisation and potential applications of 2D materials on SiO_2/Si substrates which they are typically grown or exfoliated upon, certain applications are only accessible through the use of suspended films. For example, suspended graphene membranes have been shown to demonstrate the piezoresistive effect,[192, 193] highlighting their potential for use in nanoelectromechanical system transducers. It has also recently been suggested that the interface between TMDs and their substrate can be a critical factor in device performance.[128, 194] The use of high-K dielectrics, as a substrate and to encapsulate 2D material devices, is accepted practice to reduce Coulomb scattering, improve the electron mobility and improve the on/off ratio by orders of magnitude in comparison to non-encapsulated devices on SiO_2/Si substrates.[128] The lower mobility observed for such non-encapsulated devices has been associated with the adsorption of atmospheric gases or other contaminants on the TMD surface, or the presence of trapped adsorbates between the TMD and the SiO_2 layer.[194] Similar studies on suspended graphene suggested that the scattering of external charge carriers by the underlying substrate may limit graphene device mobility, with possible contributions from surface charge traps, interfacial phonons, substrate stabilised ripples and fabrication residues on or under the 2D sheet.[195] Therefore, to fully understand the properties of MoS_2, it is important to study it by itself. Here, the effect of suspending MoS_2 is examined by detailed analysis of its Raman spectrum.

6.2 Experimental Techniques

MoS_2 was synthesised by CVD as described previously in Chapter 3, on Si substrates with 300 nm dry thermal SiO_2. A polymer support technique was used for the transfer process, where polymethyl methacrylate (PMMA, MicroChem) was spin-coated onto the as-grown MoS_2 sample and baked in atmosphere at 150 ^{o}C on a hotplate for 5 min. The films were then floated on 2 M NaOH at 80 ^{o}C until the CVD-grown MoS_2/PMMA films were floating on the surface. After cleaning in deionised water the films were transferred onto a p-doped Si(100) substrates with a 90 nm oxide layer that had holes etched by photolithography. The substrates were provided by Dr. Nils Scheuschner and fabricated in the cleanroom at the Fraunhofer Institute for Reliability and Microintegration. The holes had a diameter of 3 μm, a depth of ~8 μm and a distance of 10 μm between them. The transferred films were then allowed to dry in a desiccator until all remaining water had evaporated. It should be noted that the films had a tendency to "punch through" the holes on the substrates, which is attributed to the wet transfer process dragging the films down, and therefore it was necessary to adopt a gentler lifting and cleaning strategy for the films. The PMMA support layer was dissolved by gradual immersion in a beaker of acetone for 20 mins, rinsed by gradual immersion in a beaker of IPA, and allowed to dry in a desiccator until all remaining solvent had evaporated. A schematic of the transfer process is shown in Figure 53. Despite the care taken during transfer, many areas still had films that had "punched" through, and future work will need to be done to determine a better and more reliable experimental method for the fabrication of large-scale suspended MoS_2 for both studying the fundamental properties and for device processing. This will include optimisation of the process in order to ensure cleanliness of the sample and allow measurements in the absence of any dirt or contaminating residue. One potential strategy for improving the quality of the suspended layers is to incorporate the use of critical point dryers or supercritical drying, which have been previously used to fabricate suspended graphene devices.[196] Critical point drying removes liquid from samples in a controlled manner, and can allow preservation of the structure of delicate materials that may otherwise be damaged by conventional drying techniques.

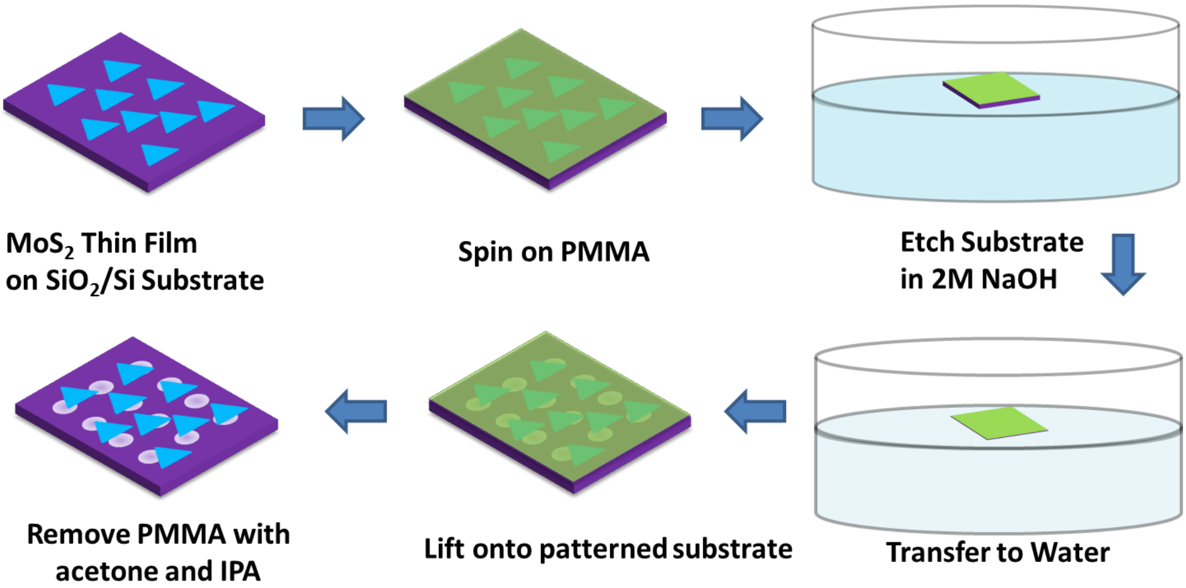

Figure 53
Schematic of the method used to make free-standing MoS_2. As-grown CVD films are transferred, using a polymer support, onto pre-etched substrates.

6.3 Results and Discussion

In Figure 54(c), an optical image of MoS_2 transferred onto a patterned holey substrate is shown. A scan was taken over 16 holes covered with MoS_2, of various thicknesses, in order to examine the effects of suspending MoS_2 freely. The layer numbered areas labelled on the map are those from which the spectra were extracted. The map of maximum intensity of the $E'/E_g/E^1_{2g}$ and A'_1/A_{1g} peaks are shown in Figure 54(a) and (b), respectively.

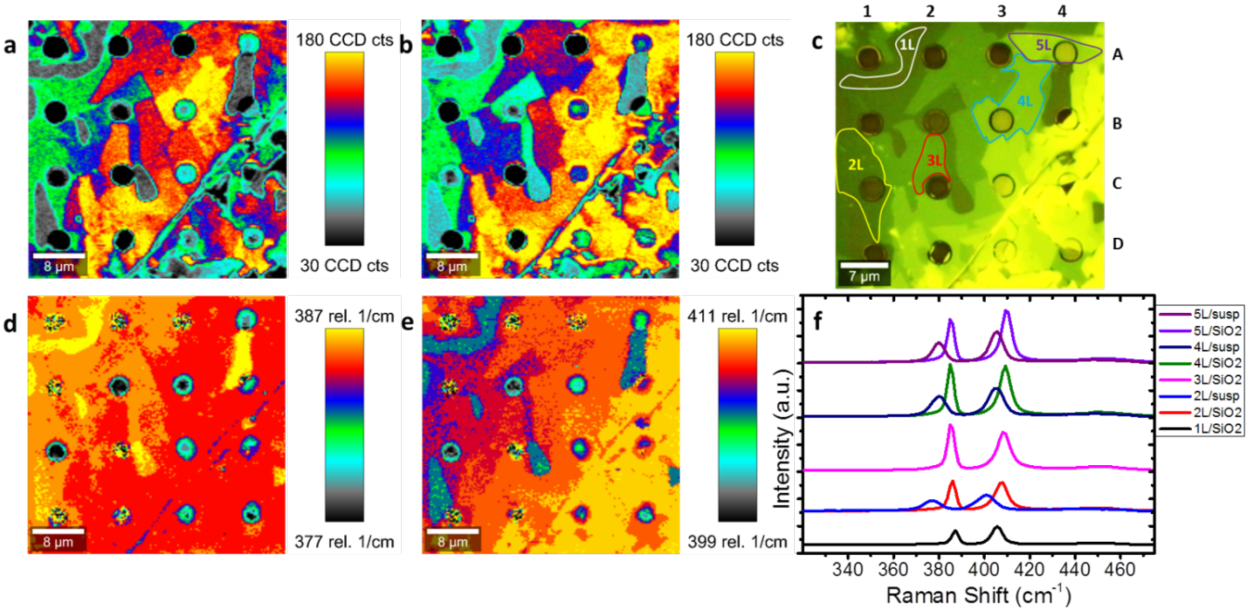

Figure 54

(a) Peak intensity map of $E'/E_g/E^1_{2g}$ (~385 cm^{-1}) Raman mode. (b) Peak intensity map of A'_1/A_{1g} (~403 cm^{-1}) Raman mode. (c) Optical image of CVD-grown MoS_2 with hole numbers labelled by row and column. (d) Map of $E'/E_g/E^1_{2g}$ mode position (e) Map of A'_1/A_{1g} mode position (f) Extracted Raman spectra of 1-5L MoS_2 with legend indicating if suspended or on substrate.

The map of the position of maximum intensity of the $E'/E_g/E^1_{2g}$ and A'_1/A_{1g} peaks are shown in Figure 54(d) and (e) respectively, and extracted spectra in Figure 54(f). There are notable changes in peak intensity and position for the $E'/E_g/E^1_{2g}$ and A'_1/A_{1g} vibrational modes with respect to changing layer number, for reasons which have been discussed in previous chapters. Therefore, the areas suspended over holes will be focused on. It is immediately clear that many of the holes do not have any material suspended over them. This is evident from the lack of any signal in peak intensity maps and the presence of noise in the peak position maps. The reason for this may be due to limitations associated with the polymer assisted transfer technique applied. It is likely that in the transfer or cleaning stage, the delicate few-layer and monolayer MoS_2, without any support from a substrate, simply tore due to the transfer procedure or subsequent PMMA removal by acetone and IPA. Nevertheless, some suspended areas remain with sufficient material to study. These have been labelled in a grid as shown in Figure 54(c), where for example the top left hole is 1A and bottom right is 4D.

Bilayer MoS_2 regions can be found on hole 1C and its surrounding regions. The supported 2L spectrum, shown in Figure 54(f), is typical for 2H stacked 2L MoS_2. The suspended 2L spectrum changes dramatically from this. A red-shift is observed in the $E'/E_g/E^1_{2g}$ and A'_1/A_{1g} peaks, as well as a significant decrease in the Raman mode intensity. The overall intensity decrease can be attributed to the absence of an underlying substrate, resulting in a lower reflection of the laser. The relative increase of the intensity of the A'_1/A_{1g} to the $E'/E_g/E^1_{2g}$ can be attributed to increased out-of-plane motion of the sulfur atoms when free of substrate interactions. The decrease in Raman shift for both modes upon suspension of MoS_2 has previously been suggested to be due to a release from residual substrate strain or doping.[197] Previous reports have also suggested that this shift may be due to biaxial strain in MoS_2 as it “sags” over the holey area,[198] and calculated a red-shift rate of strain of -2.2 cm^{-1}/% for the A'_1/A_{1g} mode and -5.2 cm^{-1}/% for the $E'/E_g/E^1_{2g}$ mode in bilayer MoS_2. Using these values as benchmarks for this work results in an estimation of biaxial tensile strain for the suspended 2L MoS_2 presented here of ~ 1.77% from the $E'/E_g/E^1_{2g}$ red-shift of ~9.2 cm^{-1}, and ~ 3.02% from the A'_1/A_{1g} red-shift of ~6.7 cm^{-1}. There are a number of possible reasons for the difference in results. Firstly, it should be noted that the results here are for CVD-grown MoS_2, consisting of large-area samples with a variety of layer thicknesses in the area studied, rather than pristine and well separated single crystals. This may allow the MoS_2 to be further strained in one direction than another, resulting in increased strain in one area compared to another. Secondly, this difference may be due to defects or dopants. While the $E'/E_g/E^1_{2g}$ mode has been reported to show little change with doping,[81, 199] the A'_1/A_{1g} mode has been reported to blue-shift with p-doping and red-shift with n-doping.[81, 105] The MoS_2 may be partially defective due to the wet polymer transfer process used to place the MoS_2 over the holes, or the MoS_2 may be doped from polymer residues, as has previously been shown for transferred CVD-graphene.[200] Here, the red-shift in the A'_1/A_{1g} mode indicates the presence of n-type dopants[201] in the films, particularly in the suspended MoS_2 areas which can be damaged from both sides. This contributes to the increased red-shift of the A'_1/A_{1g} mode in comparison to what is expected from strain alone in the suspended regions specifically. Therefore, the estimation of biaxial tensile strain of ~ 1.77% from the $E'/E_g/E^1_{2g}$ mode calculation is taken as the more realistic result.

Replotted spectra of the suspended and supported 2L, 4L and 5L high-frequency Raman regions are shown in Figure 55(a), (b) and (c) respectively. The spectra are separated in order to clearly highlight the changes in Raman peak shift discussed previously. The red-shift of Raman spectra and corresponding decrease in Raman mode intensity when the layers are suspended can also be seen in 4L MoS_2 and 5L MoS_2, although it should be noted that the change is less dramatic, with a shift of ~5 cm^{-1} the $E'/E_g/E^1_{2g}$ mode and ~4 cm^{-1} for the A'_1/A_{1g} mode for both. This decreasing shift is attributed to less sagging-induced strain of the MoS_2 with increasing layer number, as the layers begin to support each other.

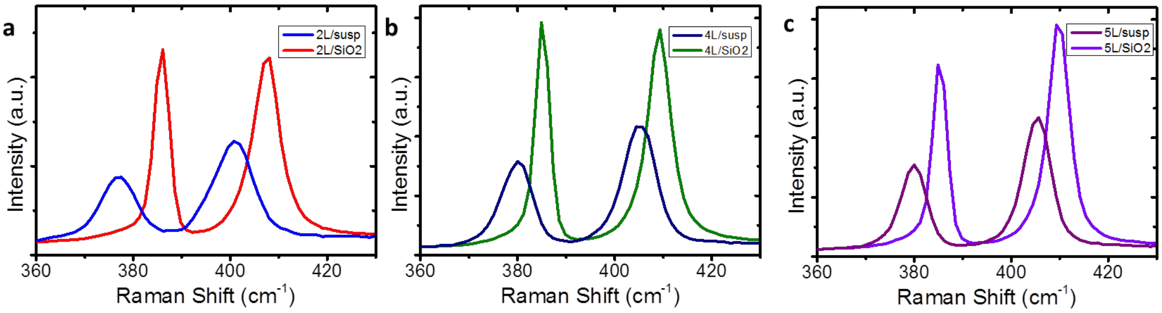

Figure 55
Individual Raman spectra from Figure 54(f), replotted in order to clearly demonstrate the observed changes, showing the suspended and supported high-frequency regions for (a) 2L (b) 4L and (c) 5L MoS_2.

Analysis of the low-frequency Raman spectra for the same sample can be found in Figure 56. A map of the position of maximum peak intensity in the low-frequency regime is shown in Figure 56(a). As shown previously in Chapter 5 and in the literature,[154, 202] position maps of low-frequency Raman modes can be used as a facile method of layer number characterisation in MoS_2 and other TMDs. Bilayer MoS_2 is found over hole 1C and its surrounding area. The map of peak intensity for the LBM at ~40 cm^{-1}, which can be used to identify bilayer regions, is shown in Figure 56(b). It is clear that the intensity of the 2L LBM peak increases dramatically when suspended over hole 1C. This can be attributed to increased out-of-plane motion as the layers breathe against each other without substrate effects. The suspended 2L spectrum is slightly red-shifted in comparison to the 2L on substrate, which is attributed to strain effects as discussed above. While suspended 3L MoS_2 suspended could was not found on this sample, possibly due to tearing of the film during transfer, the intensity of the low-frequency peak at ~29 cm^{-1} for 3L MoS_2 was mapped in Figure 56(c). The brightest yellow regions indicate 3L MoS_2 is present. 4L MoS_2 in hole 3B and its surrounding area is mapped in Figure 56(d), which shows the map of peak intensity centred at ~31 cm^{-1}, the SM in the low-frequency region for 4L MoS_2. This SM decreases in intensity for the suspended 4L MoS_2, in comparison to 4L MoS_2 on the substrate. This decrease in intensity can be attributed to the suspended layers no longer being supported by the substrate, and therefore no longer pulling in a shear motion against the substrate, combined with a decreased reflectivity of the signal from the substrate. The LBM at ~23 cm^{-1} increases in intensity, as was the case for 2L, due to increased out-of-plane motion as the layers breathe. The change in spectra between supported and suspended MoS_2 for the 5L region in hole 4A and the surrounding area is negligible in the low-frequency region, which is attributed to the increasing layer number, as the relative motions of the layers to each other may change less as the layer number increases due to increased stiffening and support. The map of maximum intensity of the 5L low-frequency LBM at ~17 cm^{-1} is shown in Figure 56(e) to illustrate this. All of the extracted spectra in the low-frequency region are shown in the plot in Figure 56(f).

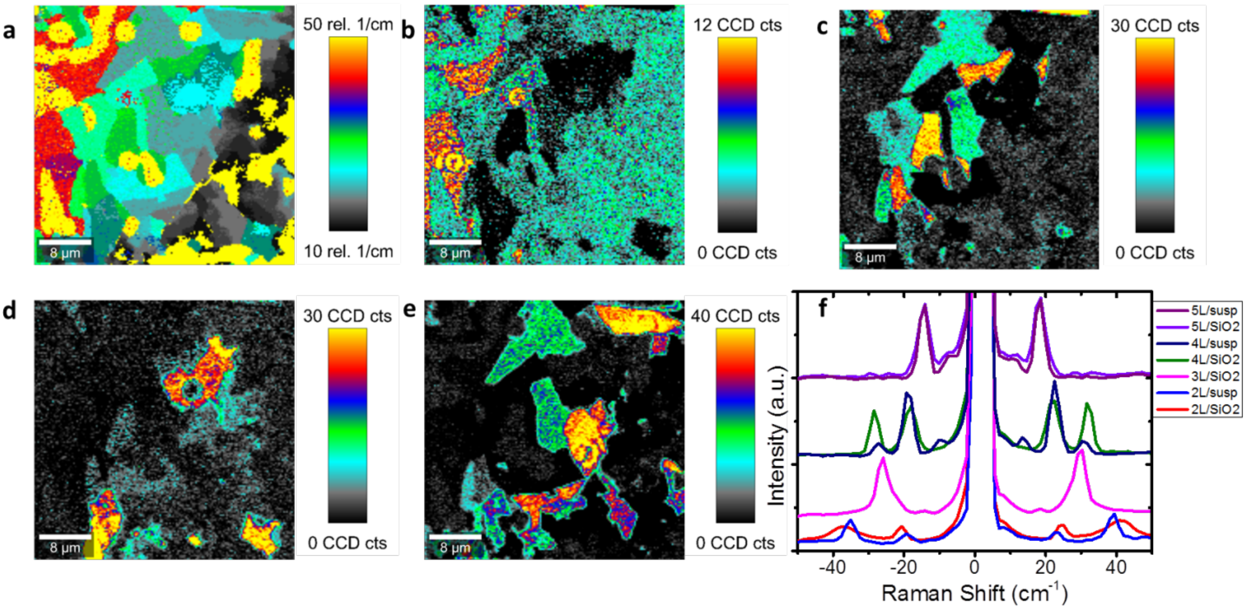

Figure 56
(a) Map of position of maximum peak intensity in the region of 10–50 cm^{-1}. (b) Peak intensity map of LBM peak for 2L MoS_2 at ~40 cm^{-1}. (c) Peak intensity map of SM/LBM peak for 3L MoS_2 at ~29 cm^{-1}. (d) Peak intensity map of max SM for 4L MoS_2 at ~31 cm^{-1}. (e) Peak intensity map of max LBM for 5L MoS_2 at ~17 cm^{-1}. (f) Low-frequency Raman spectra of SMs and LBMs of 1-5L MoS_2, with legend indicating if suspended or on substrate.

Replotted spectra of the suspended and supported 2L, 4L and 5L low-frequency Raman regions are shown in Figure 57(a), (b) and (c) respectively. The spectra are separated in order to clearly highlight the changes in Raman peak shift discussed previously. In Figure 57(a), the low-frequency region of 2L MoS_2 is shown, emphasising the enhancement in intensity and slight red-shift of the LBM upon suspension over a hole as discussed previously. A similar yet less obvious increase in intensity can be seen for the 4L suspended LBM in Figure 57(b), while in the 5L in Figure 57(c), the increase is not significant.

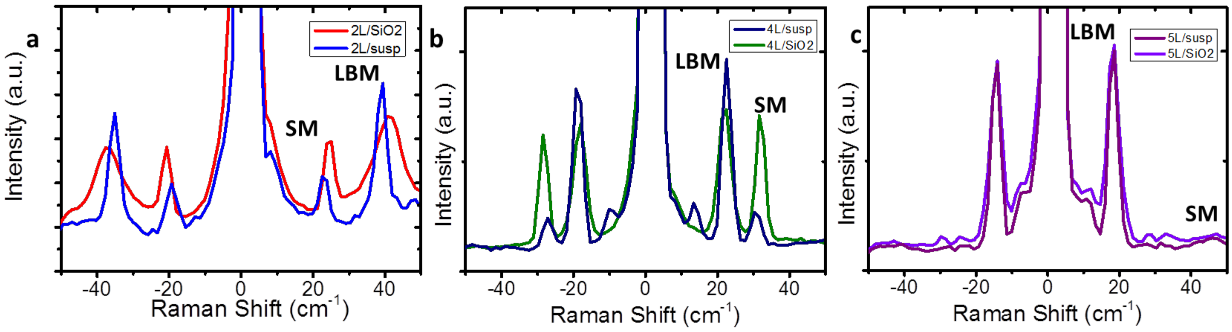

Figure 57
Individual Raman spectra from Figure 56(f), replotted in order to clearly demonstrate the observed changes, showing the suspended and supported low-frequency regions for (a) 2L (b) 4L and (c) 5L MoS_2.

6.4 Summary

Raman spectroscopic measurements were performed on CVD-grown MoS_2 which was transferred to a pre-patterned holey SiO_2/Si substrate. Significant differences in suspended and supported MoS_2 were observed up to 4L MoS_2, in both high and low-frequency Raman spectral regions, which were attributed to strained MoS_2 over the holes and increased out-of-plane motion of the layers due to lack of substrate inhibitions. For 5L MoS_2, while a significant change was observed in the high-frequency Raman spectrum of suspended vs. supported MoS_2 due to increased strain, little change was seen in the low-frequency region. This was attributed to a lower relative change in the motions of the layers as layer number increases and the sample becomes self-supporting. Future work could include examining the electrical device characteristics of suspended vs. supported CVD-grown MoS_2 as a pathway towards fully suspended 2D material devices, and analysing the change in material strain with different sized holes on substrates. It is envisaged that future work will also include further studies on other TMD materials in order to understand the effects of strain on their properties and performance, and how this is likely to affect their future industrial adaption.

7 Conclusions

7.1 Conclusions

The work presented here focuses on the development of reliable growth methods of thin films transition metal dichalcogenides and subsequent characterisation of these materials by Raman spectroscopy.

Initial work focused on the fabrication of TMDs by TAC of pre-deposited layers. This was shown to be successful and was concluded to be a suitable technique for the fabrication of thin TMD films for applications where a highly crystalline film is not required. A method for low-temperature synthesis of polycrystalline TMD thin films was presented, by converting WO_3 to WS_2 with an inductively coupled H_2S plasma used as the sulfur source. These films were used to demonstrate the first gas sensing response for WS_2 thin films, with highly sensitive detection towards NH_3.

A method for reliable production of TMD monolayers was presented, by use of liquid-phase exfoliated TMO nanosheet precursors in a close proximity microreactor setup for CVD growth. The quality of the as-grown layers was investigated using XPS, SEM and TEM. Raman and PL spectra were used to further probe the quality of the layers and the properties of the grain boundaries present. Electrical transport results showed carrier mobilities comparable to single crystal devices without encapsulating layers. This process was extended to the growth of patternable TMD monolayers, by directly transferring patterns made with precursor layers to a growth substrate. This is a new pathway which could potentially lead to the development of patterned CVD monolayers for the production of future device components.

TAC was shown to be useful in the synthesis of little-studied TMDs such as $PtSe_2$, in which mechanical or liquid-phase exfoliation is an unrealistic route to scale-up due to the relative scarcity of naturally-occurring starting powders and crystals. $PtSe_2$ thin films of controllable thickness were synthesised using TAC by direct selenisation of predeposited Pt layers at a low temperature of 450 ^oC. STEM studies confirmed that the crystal lattice of $PtSe_2$ is a 1T crystal structure, allowing the Raman spectrum of $PtSe_2$ to be analysed and interpreted. The Raman-active modes in $PtSe_2$ were investigated in detail. The A_{1g} and E_g out-of-plane and in-plane modes, respectively, were identified using a variety of different laser wavelengths, and these assignments were confirmed using polarisation-dependent measurements and theoretical modelling. Furthermore, the thickness dependent behaviour of the Raman spectrum of $PtSe_2$ was investigated, which is anticipated to facilitate further investigation into the properties of $PtSe_2$ and other exotic TMDs.

A detailed analysis of Raman scattering in CVD-grown mono- and few-layer TMDs was presented. The general peak shift trends were similar for all the TMDs studied due to their similar lattice structures, however, the intensity dependencies and Raman shifts varied in each due to the different masses of metal and chalcogen, and due to the stacking order of the layers. The determination of layer number and material properties via low-frequency Raman measurements is a crucial development in the research and analysis of TMDs, as is the stacking configuration determination, which is shown in this work by Raman mode mapping techniques. Low-frequency Raman mode mapping of CVD-$MoSe_2$ and WSe_2 allowed identification of 2H and 3R stacking configurations, even across what optically can appear to be the same crystal. This highlights the usefulness of Raman spectroscopy in the identification of material properties which would otherwise require laborious and destructive electron microscopy. Further, a new peak in the low-frequency region of WS_2 was observed at ~27 cm^{-1} in resonance conditions.

Suspended CVD-MoS_2 was studied *via* Raman spectroscopy. Significant differences in suspended and supported MoS_2 were observed up to 5L in the high-frequency Raman spectrum, and up to 4L in the low-frequency region. These changes were attributed to strain induced in the MoS_2 due to its sagging over the holes, and increased out-of-plane motion of the layers due to lack of substrate interactions.

7.2 Future Work

The CVD microreactor methodology outlined here could be extended to other TMDs, depending on the dispersability of the metal precursor used. The growth of these materials on substrates such as SiO_2/Si will facilitate their electrical, optical and chemical characterisation.

The synthesis and characterisation route detailed here for $PtSe_2$ paves the way for similar work on other little-studied TMDs, many of which are theoretically predicted to exist but have not been synthesised yet. It envisaged that future work will entail the physical, electrical and perhaps electrochemical characterisation of these materials and their subsequent assessment for use in applications such as sensing, (opto)electronics, and electrocatalysis.

Low-frequency Raman mapping could be readily applied to quickly assess the layer number of TMDs produced by other methods, such as liquid-phase exfoliation, to ascertain their suitability for specific applications. Importantly, this methodology could be extended to other TMD crystals that do not show significant changes in the high-frequency region of their Raman spectrum with layer number, such as ReS_2[203]. Furthermore, it is anticipated that this technique will be useful for investigating layer number and stacking orientation in 2D material alloys[204] and recently fabricated TMD heterostructures.[165, 166] Future work could further explore the low-frequency modes of TMDs with a variety of laser wavelengths. This would allow the full characterisation of the behaviour of low-frequency modes under a variety of excitation energies, and probe for the presence of resonance peaks in these materials beyond what has been shown here for WS_2 and previously in the literature for MoS_2.[191] The low-frequency mapping techniques outlined here could also be extended to artificial stacks of different 2D materials, or 2D materials with functional organic layers, in order to assess the crystallinity and registry of the layers by studying how they interact with each other.

Further work on TMDs suspended over cavities or holes could include examination of the electrical device characteristics of suspended vs. supported TMDs as a pathway towards fully suspended 2D devices. The change in material strain with different sized holes on substrates is also important to examine, as it could significantly alter the material properties. It is envisaged that future work will also include PL measurements on suspended 2D layers, as well as similar studies on other TMD materials with different crystal structures, such as 1T-$PtSe_2$, in order to understand the effects of strain on their properties and performance.

Publications and Presentations

Publications

The following list details all co-authored research publications that the work carried out in this thesis has contributed to.

1. Elibol, K. et al. Grain boundary-mediated nanopores in molybdenum disulfide grown by chemical vapor deposition. *Nanoscale* **9**, 1591-1598 (2017).
2. Yim, C. et al. High-Performance Hybrid Electronic Devices from Layered $PtSe_2$ Films Grown at Low Temperature. *ACS Nano* **10**, 9550-9558 (2016).
3. Vega-Mayoral, V. et al. Photoluminescence from Liquid-Exfoliated WS_2 Monomers in Poly(Vinyl Alcohol) Polymer Composites. *Advanced Functional Materials* **26**, 1028-1039 (2016).
4. O'Brien, M. et al. Raman characterization of platinum diselenide thin films. *2D Materials* **3**, 021004 (2016).
5. O'Brien, M. et al. Mapping of Low-Frequency Raman Modes in CVD-Grown Transition Metal Dichalcogenides: Layer Number, Stacking Orientation and Resonant Effects. *Scientific reports* **6,** 19476 (2016).
6. Zhang, S. et al. Direct Observation of Degenerate Two-Photon Absorption and Its Saturation in WS_2 and MoS_2 Monolayer and Few-Layer Films. *ACS Nano* **9**, 7142-7150 (2015).
7. Wirtz, C. et al. Atomic layer deposition on 2D transition metal chalcogenides: Layer dependent reactivity and seeding with organic ad-layers. *Chemical Communications* **51**, 16553-16556 (2015).

8. O'Brien, M. et al. Low wavenumber Raman spectroscopy of highly crystalline $MoSe_2$ grown by chemical vapor deposition. *physica status solidi (B)* **252**, 2385-2389 (2015).
9. Yim, C. et al. Investigation of the optical properties of MoS_2 thin films using spectroscopic ellipsometry. *Applied Physics Letters* **104**, 103114 (2014).
10. Yim, C. et al. Heterojunction hybrid devices from vapor phase grown MoS_2. *Scientific reports* **4**, 5458 (2014).
11. O'Brien, M. et al. Transition metal dichalcogenide growth via close proximity precursor supply. *Scientific reports* **4**, 7374 (2014).
12. O'Brien, M. et al. Plasma assisted synthesis of WS_2 for gas sensing applications. *Chemical Physics Letters* **615**, 6-10 (2014).
13. Nolan, H. et al. Molybdenum disulfide/pyrolytic carbon hybrid electrodes for scalable hydrogen evolution. *Nanoscale* **6**, 8185-8191 (2014).
14. Gatensby, R. et al. Controlled synthesis of transition metal dichalcogenide thin films for electronic applications. *Applied Surface Science* **297**, 139-146 (2014).

Presentations

The following list details all presentations of the work carried out in this thesis

Oral Presentations

1. “Synthesis and Applications of 2D Materials” Intel Ireland Research Conference, 12th October 2016, University College Dublin.
2. “2D Materials - The Future of Electronics?” Dorgan Postgraduate Prize Presentation, September 2016, Trinity College Dublin.
3. “Raman Spectroscopy of Vapour Phase Synthesised 2D Semiconductors” Third Year Talk, May 2016, Trinity College Dublin.
4. “Vapour Phase Synthesis of Transition Metal Dichalcogenides” BOC Gases Talk, 24th April 2015, Trinity College Dublin.
5. “Spectroscopic Analysis of Transition Metal Dichalcogenides” Annual Symposium of the Microscopy Society of Ireland, 26-28th August 2015, University of Limerick.
6. “Spectroscopic Analysis of CVD grown Monolayer MoS_2 to identify Suitability for Device Applications” Intel Ireland Research Conference, 18th November 2014, Science Gallery, Trinity College Dublin.
7. “Novel Approaches to Vapour Phase Growth of TMDs” Flatlands beyond Graphene, Trinity College Dublin, 9-11th July 2014.

Poster Presentations

1. “Low-Frequency Raman Spectroscopy of TMDs: Layer Number and Stacking Configuration” 30th International Winterschool on Electronic Properties of Novel Materials, Kirchberg, Tirol, 13-20th February 2016.

2. “Raman Spectroscopy of 2D Semiconductors” NanoNet Ireland, University of Limerick, 21-22nd October 2015.
3. “Raman Spectroscopy of 2D Semiconductors” Intel Ireland Research Conference, Smock Alley Theatre, Dublin, 20th October 2015.
4. “Chemical Vapour Deposition of MoS_2 and WS_2 Monolayers in a Microreactor” University of Manchester, 22-26th June 2015.
5. “Chemical Vapor Deposition of TMDs” 29th International Winterschool on Electronic Properties of Novel Materials, Kirchberg, Tirol, 7-14th March 2015
8. “Vapour Phase Growth of TMDs” Flatlands beyond Graphene, Trinity College Dublin, 9-11th July 2014.
9. “CVD Synthesis of Monolayer Transition Metal Dichalcogenides” SFI Ireland-China Symposium on Nanotechnology, 12-14th May 2014.
6. “Low Temperature Plasma Assisted Synthesis of WS_2 Thin Films” 28th International Winterschool on Electronic Properties of Novel Materials, Kirchberg, Tirol, 8-15th March 2015.
7. “MoS_2 Photodiodes” SFI AMBER Launch, Croke Park, Dublin, 24th October 2013.

Bibliography

1. Novoselov, K.S. et al. Electric Field Effect in Atomically Thin Carbon Films. *Science* **306**, 666-669 (2004).
2. Nicolosi, V., Chhowalla, M., Kanatzidis, M.G., Strano, M.S. & Coleman, J.N. Liquid Exfoliation of Layered Materials. *Science* **340** (2013).
3. Geim, A.K. & Grigorieva, I.V. Van der Waals heterostructures. *Nature* **499**, 419-425 (2013).
4. Lee, G.-H. et al. Heterostructures based on inorganic and organic van der Waals systems. *APL Materials* **2** (2014).
5. Duesberg, G.S. Heterojunctions in 2D semiconductors: A perfect match. *Nature materials* **13**, 1075-1076 (2014).
6. Geim, A.K. & Novoselov, K.S. The rise of graphene. *Nature materials* **6**, 183-191 (2007).
7. Mak, K.F., Lee, C., Hone, J., Shan, J. & Heinz, T.F. Atomically Thin MoS_2: A New Direct-Gap Semiconductor. *Physical Review Letters.* **105**, 136805 (2010).
8. Splendiani, A. et al. Emerging photoluminescence in monolayer MoS_2. *Nano Letters* **10**, 1271-1275 (2010).
9. Novoselov, K.S. et al. Two-dimensional atomic crystals. *Proceedings of the National Academy of Sciences* **102**, 10451-10453 (2005).
10. Cao, T. et al. Valley-selective circular dichroism of monolayer molybdenum disulphide. *Nature Communications.* **3**, 887 (2012).
11. Radisavljevic, B., Radenovic, A., Brivio, J., Giacometti, V. & Kis, A. Single-layer MoS_2 transistors. *Nature Nanotechnology.* **6**, 147-150 (2011).
12. Ovchinnikov, D., Allain, A., Huang, Y.-S., Dumcenco, D. & Kis, A. Electrical Transport Properties of Single-Layer WS_2. *ACS nano* **8**, 8174-8181 (2014).
13. Iqbal, M.W. et al. High-mobility and air-stable single-layer WS_2 field-effect transistors sandwiched between chemical vapor deposition-grown hexagonal BN films. *Scientific reports* **5**, 10699 (2015).
14. Lee, K., Gatensby, R., McEvoy, N., Hallam, T. & Duesberg, G.S. High-performance sensors based on molybdenum disulfide thin films. *Advanced Materials* **25**, 6699-6702 (2013).
15. Lembke, D. & Kis, A. Breakdown of High-Performance Monolayer MoS_2 Transistors. *ACS Nano* **6**, 10070-10075 (2012).
16. Lopez-Sanchez, O. et al. Light Generation and Harvesting in a van der Waals Heterostructure. *ACS Nano* **8**, 3042-3048 (2014).
17. Lopez-Sanchez, O., Lembke, D., Kayci, M., Radenovic, A. & Kis, A. Ultrasensitive photodetectors based on monolayer MoS_2. *Nature nanotechnology.* **8**, 497-501 (2013).
18. Sarkar, D. et al. MoS_2 Field-Effect Transistor for Next-Generation Label-Free Biosensors. *ACS Nano* **8**, 3992-4003 (2014).
19. Bernardi, M., Palummo, M. & Grossman, J.C. Extraordinary Sunlight Absorption and 1 nm-Thick Photovoltaics using Two-Dimensional Monolayer Materials. *Nano Letters* (2013).
20. Tsai, M.-L. et al. Monolayer MoS_2 Heterojunction Solar Cells. *ACS Nano* **8**, 8317-8322 (2014).

21. Kappera, R. et al. Phase-engineered low-resistance contacts for ultrathin MoS_2 transistors. *Nature materials* **13**, 1128-1134 (2014).
22. Kappera, R. et al. Metallic 1T phase source/drain electrodes for field effect transistors from chemical vapor deposited MoS_2. *APL Materials* **2**, 092516 (2014).
23. Acerce, M., Voiry, D. & Chhowalla, M. Metallic 1T phase MoS_2 nanosheets as supercapacitor electrode materials. *Nature Nanotechnology.* **10**, 313-318 (2015).
24. Eda, G. et al. Photoluminescence from Chemically Exfoliated MoS_2. *Nano Letters* **11**, 5111-5116 (2011).
25. Pizzocchero, F. et al. The hot pick-up technique for batch assembly of van der Waals heterostructures. *Nature Communications.* **7**, 11894 (2016).
26. Rezania, B., Dorn, M., Severin, N. & Rabe, J.P. Influence of graphene exfoliation on the properties of water-containing adlayers visualized by graphenes and scanning force microscopy. *Journal of Colloid and Interface Science* **407**, 500-504 (2013).
27. Castellanos-Gomez, A. et al. Deterministic transfer of two-dimensional materials by all-dry viscoelastic stamping. *2D Materials* **1**, 011002 (2014).
28. Novoselov, K.S. & Neto, A.H.C. Two-dimensional crystals-based heterostructures: materials with tailored properties. *Physica Scripta* **2012**, 014006 (2012).
29. Coleman, J.N. et al. Two-Dimensional Nanosheets Produced by Liquid Exfoliation of Layered Materials. *Science* **331**, 568-571 (2011).
30. Backes, C. et al. Edge and confinement effects allow in situ measurement of size and thickness of liquid-exfoliated nanosheets. *Nature Communications.* **5**, 4576 (2014).
31. Lee, K. et al. Electrical Characteristics of Molybdenum Disulfide Flakes Produced by Liquid Exfoliation. *Advanced Materials* **23**, 4178-4182 (2011).
32. Paton, K.R. et al. Scalable production of large quantities of defect-free few-layer graphene by shear exfoliation in liquids. *Nature materials* (2014).
33. Cunningham, G. et al. Solvent Exfoliation of Transition Metal Dichalcogenides: Dispersibility of Exfoliated Nanosheets Varies Only Weakly between Compounds. *ACS Nano* **6**, 3468-3480 (2012).
34. Cunningham, G. et al. Photoconductivity of solution-processed MoS_2 films. *Journal of Materials Chemistry C* **1**, 6899-6904 (2013).
35. Boland, C.S. et al. Sensitive electromechanical sensors using viscoelastic graphene-polymer nanocomposites. *Science* **354**, 1257 (2016).
36. Cunningham, G. et al. Percolation scaling in composites of exfoliated MoS_2 filled with nanotubes and graphene. *Nanoscale* **4**, 6260-6264 (2012).
37. Bonaccorso, F. & Sun, Z. Solution processing of graphene, topological insulators and other 2D crystals for ultrafast photonics. *Optical Materials Express.* **4**, 63-78 (2014).
38. Backes, C. et al. Production of Highly Monolayer Enriched Dispersions of Liquid-Exfoliated Nanosheets by Liquid Cascade Centrifugation. *ACS Nano* **10**, 1589-1601 (2016).
39. Kelly, A.G. et al. All-printed thin-film transistors from networks of liquid-exfoliated nanosheets. *Science* **In Press** (2017).
40. Kong, D. et al. Synthesis of MoS_2 and $MoSe_2$ films with vertically aligned layers. *Nano Letters* **13**, 1341-1347 (2013).
41. Gatensby, R. et al. Controlled synthesis of transition metal dichalcogenide thin films for electronic applications. *Applied Surface Science.* **297**, 139-146 (2014).
42. Yim, C. et al. Heterojunction Hybrid Devices from Vapor Phase Grown MoS_2. *Scientific reports* **4**, 5458 (2014).

43. Duffy, R. et al. Structural and Electrical Investigation of MoS_2 Thin Films Formed by Thermal Assisted Conversion of Mo Metal. *ECS Journal of Solid State Science and Technology* **5**, Q3016-Q3020 (2016).
44. Yu, J.H. et al. Vertical Heterostructure of Two-Dimensional MoS_2 and WSe_2 with Vertically Aligned Layers. *Nano Letters* **15**, 1031-1035 (2015).
45. Lide, D.R. CRC handbook of chemistry and physics. (CRC press, 2004).
46. Lin, Y.-C. et al. Wafer-scale MoS_2 thin layers prepared by MoO_3 sulfurization. *Nanoscale* **4**, 6637-6641 (2012).
47. Nolan, H. et al. Molybdenum disulfide/pyrolytic carbon hybrid electrodes for scalable hydrogen evolution. *Nanoscale* **6**, 8185-8191 (2014).
48. Laskar, M.R. et al. Large area single crystal (0001) oriented MoS_2. *Applied Physics Letters.* **102**, 252108 (2013).
49. Gatensby, R., Hallam, T., Lee, K., McEvoy, N. & Duesberg, G.S. Investigations of vapour-phase deposited transition metal dichalcogenide films for future electronic applications. *Solid-State Electronics.* **125**, 39-51 (2016).
50. Nishi, Y. & Doering, R. Handbook of semiconductor manufacturing technology. (CRC Press, 2000).
51. Creighton, J. & Ho, P. Introduction to chemical vapor deposition (CVD). *Chemical vapor deposition* **2**, 1-22 (2001).
52. Amani, M. et al. Electrical performance of monolayer MoS_2 field-effect transistors prepared by chemical vapor deposition. *Applied Physics Letters.* **102**, 193107 (2013).
53. Kang, K. et al. High-mobility three-atom-thick semiconducting films with wafer-scale homogeneity. *Nature* **520**, 656-660 (2015).
54. Lee, Y.H. et al. Synthesis of large-area MoS_2 atomic layers with chemical vapor deposition. *Advanced Materials* **24**, 2320-2325 (2012).
55. Zhan, Y., Liu, Z., Najmaei, S., Ajayan, P.M. & Lou, J. Large-area vapor-phase growth and characterization of MoS_2 atomic layers on a SiO_2 substrate. *Small* **8**, 966-971 (2012).
56. Néstor, P.-L. et al. CVD-grown monolayered MoS_2 as an effective photosensor operating at low-voltage. *2D Materials* **1**, 011004 (2014).
57. Gutierrez, H.R. et al. Extraordinary Room-Temperature Photoluminescence in Triangular WS_2 Monolayers. *Nano Letters* **13** 3447-3454 (2012).
58. Berkdemir, A. et al. Identification of individual and few layers of WS_2 using Raman Spectroscopy. *Scientific reports* **3**, 1755 (2013).
59. Elías, A.L. et al. Controlled Synthesis and Transfer of Large-Area WS_2 Sheets: From Single Layer to Few Layers. *ACS Nano* **7**, 5235-5242 (2013).
60. Liu, Y. et al. Mesoscale Imperfections in MoS_2 Atomic Layers Grown by a Vapor Transport Technique. *Nano Letters* **14**, 4682-4686 (2014).
61. Cheng, Y. et al. Van der Waals epitaxial growth of MoS_2 on SiO_2/Si by chemical vapor deposition. *RSC Advances* **3**, 17287-17293 (2013).
62. Ji, Q. et al. Epitaxial Monolayer MoS_2 on Mica with Novel Photoluminescence. *Nano Letters* **13**, 3870-3877 (2013).
63. van der Zande, A.M. et al. Grains and grain boundaries in highly crystalline monolayer molybdenum disulphide. *Nature materials.* **12**, 554-561 (2013).
64. Ling, X. et al. Role of the Seeding Promoter in MoS_2 Growth by Chemical Vapor Deposition. *Nano Letters* **14**, 464-472 (2014).
65. Ionescu, R. et al. Synthesis of Atomically Thin MoS_2 Triangles and Hexagrams and Their Electrical Transport Properties. *Nanotechnology, IEEE Transactions on* **13**, 749-754 (2014).

66. Najmaei, S. et al. Vapour phase growth and grain boundary structure of molybdenum disulphide atomic layers. *Nature materials* **12**, 754-759 (2013).
67. Dumcenco, D. et al. Large-Area Epitaxial Monolayer MoS_2. *ACS Nano* **9**, 4611-4620 (2015).
68. Dieing, T., Hollricher, O. & Toporski, J. Confocal raman microscopy, Vol. 158. (Springer Science & Business Media, 2011).
69. Ferraro, J.R. Introductory Raman spectroscopy. (Academic press, 2003).
70. Ferrari, A.C. & Basko, D.M. Raman spectroscopy as a versatile tool for studying the properties of graphene. *Nature Nanotechnology.* **8**, 235-246 (2013).
71. Lee, C. et al. Anomalous Lattice Vibrations of Single- and Few-Layer MoS_2. *ACS Nano* **4**, 2695-2700 (2010).
72. Scheuschner, N., Gillen, R., Staiger, M. & Maultzsch, J. Interlayer resonant Raman modes in few-layer MoS_2. *Physical Review B.* **91**, 235409 (2015).
73. Verble, J.L. & Wieting, T.J. Lattice Mode Degeneracy in MoS_2 and Other Layer Compounds. *Physical Review Letters.* **25**, 362-365 (1970).
74. Zhang, X. et al. Raman spectroscopy of shear and layer breathing modes in multilayer MoS_2. *Physical Review B.* **87**, 115413 (2013).
75. Li, H. et al. From Bulk to Monolayer MoS_2: Evolution of Raman Scattering. *Advanced Functional Materials* **22**, 1385-1390 (2012).
76. Zhang, X. et al. Phonon and Raman scattering of two-dimensional transition metal dichalcogenides from monolayer, multilayer to bulk material. *Chemical Society reviews* **44**, 2757-2785 (2015).
77. Zhu, C. et al. Strain tuning of optical emission energy and polarization in monolayer and bilayer MoS 2. *Physical Review B.* **88**, 121301 (2013).
78. Yan, R. et al. Thermal Conductivity of Monolayer Molybdenum Disulfide Obtained from Temperature-Dependent Raman Spectroscopy. *ACS Nano* **8**, 986-993 (2014).
79. Beechem, T., Graham, S., Kearney, S.P., Phinney, L.M. & Serrano, J.R. Invited Article: Simultaneous mapping of temperature and stress in microdevices using micro-Raman spectroscopy. *Review of Scientific Instruments* **78**, 061301 (2007).
80. Shi, Y. et al. Selective Decoration of Au Nanoparticles on Monolayer MoS_2 Single Crystals. *Scientific reports* **3**, 1839 (2013).
81. Chakraborty, B. et al. Symmetry-dependent phonon renormalization in monolayer MoS_2 transistor. *Physical Review B.* **85**, 161403 (2012).
82. Mignuzzi, S. et al. Effect of disorder on Raman scattering of single-layer MoS_2. *Physical Review B.* **91**, 195411 (2015).
83. Zhao, W. et al. Lattice dynamics in mono- and few-layer sheets of WS_2 and WSe_2. *Nanoscale* **5**, 9677-9683 (2013).
84. Ma, Y. et al. Electronic and magnetic properties of perfect, vacancy-doped, and nonmetal adsorbed $MoSe_2$, $MoTe_2$ and WS_2 monolayers. *Physical Chemistry Chemical Physics.* **13**, 15546-15553 (2011).
85. Ballif, C. et al. Preparation and characterization of highly oriented, photoconducting WS_2 thin films. *Applied Physics A.* **62**, 543-546 (1996).
86. Hertz, H. Ueber einen Einfluss des ultravioletten Lichtes auf die electrische Entladung. *Annalen der Physik* **267**, 983-1000 (1887).
87. Einstein, A. Über einen die Erzeugung und Verwandlung des Lichtes betreffenden heuristischen Gesichtspunkt. *Annalen der Physik* **322**, 132-148 (1905).
88. Shmeliov, A. et al. Unusual Stacking Variations in Liquid-Phase Exfoliated Transition Metal Dichalcogenides. *ACS Nano* **8**, 3690-3699 (2014).
89. Hetherington, C. Aberration correction for TEM. *Materials Today.* **7**, 50-55 (2004).

90. O'Brien, M. et al. Transition Metal Dichalcogenide Growth via Close Proximity Precursor Supply. *Scientific reports* **4**, 7374 (2014).
91. O'Brien, M. et al. Plasma assisted synthesis of WS_2 for gas sensing applications. *Chemical Physics Letters* **615**, 6-10 (2014).
92. Yim, C. et al. Investigation of the optical properties of MoS_2 thin films using spectroscopic ellipsometry. *Applied Physics Letters.* **104**, 103114 (2014).
93. Zhang, J. et al. Scalable Growth of High-Quality Polycrystalline MoS_2 Monolayers on SiO_2 with Tunable Grain Sizes. *ACS Nano* **8**, 6024-6030 (2014).
94. Ennaoui, A. et al. Iron disulfide for solar energy conversion. *Solar Energy Materials and Solar Cells* **29**, 289-370 (1993).
95. Yu, L. et al. Iron Chalcogenide Photovoltaic Absorbers. *Advanced Energy Materials* **1**, 748-753 (2011).
96. Morrish, R., Haak, T. & Wolden, C.A. Low-Temperature Synthesis of n-Type WS_2 Thin Films via H_2S Plasma Sulfurization of WO_3. *Chemistry of Materials* **26**, 3986–3992 (2014).
97. Ross-Medgaarden, E.I. & Wachs, I.E. Structural determination of bulk and surface tungsten oxides with UV-vis diffuse reflectance spectroscopy and Raman spectroscopy. *The Journal of Physical Chemistry C* **111**, 15089-15099 (2007).
98. Yao, J.N., Chen, P. & Fujishima, A. Electrochromic behavior of electrodeposited tungsten oxide thin films. *Journal of Electroanalytical Chemistry* **406**, 223-226 (1996).
99. Sivakumar, R., Gopalakrishnan, R., Jayachandran, M. & Sanjeeviraja, C. Investigation of X-ray photoelectron spectroscopic (XPS), cyclic voltammetric analyses of WO_3 films and their electrochromic response in FTO/WO_3/electrolyte/FTO cells. *Smart Materials and Structures* **15**, 877 (2006).
100. Mao, X., Xu, Y., Xue, Q., Wang, W. & Gao, D. Ferromagnetism in exfoliated tungsten disulfide nanosheets. *Nanoscale Research Letters.* **8**, 1-6 (2013).
101. Chhowalla, M. et al. The chemistry of two-dimensional layered transition metal dichalcogenide nanosheets. *Nature Chemistry* **5**, 263-275 (2013).
102. Li, X.L. & Li, Y.D. Formation of MoS_2 Inorganic Fullerenes (IFs) by the Reaction of MoO_3 Nanobelts and S. *Chemistry – A European Journal* **9**, 2726-2731 (2003).
103. Hussain, S. et al. Controlled synthesis and optical properties of polycrystalline molybdenum disulfide atomic layers grown by chemical vapor deposition. *Journal of Alloys and Compounds* **653**, 369-378 (2015).
104. Helveg, S. et al. Atomic-Scale Structure of Single-Layer MoS_2 Nanoclusters. *Physical Review Letters.* **84**, 951-954 (2000).
105. Shi, Y. et al. Selective Decoration of Au Nanoparticles on Monolayer MoS_2 Single Crystals. *Scientific Reports.* **3**, 1839 (2013).
106. Senthilkumar, V. et al. Direct vapor phase growth process and robust photoluminescence properties of large area MoS_2 layers. *Nano Research,* **7**, 1759-1768 (2014).
107. Chen, S. et al. Millimeter-Size Single-Crystal Graphene by Suppressing Evaporative Loss of Cu During Low Pressure Chemical Vapor Deposition. *Advanced Materials* **25**, 2062-2065 (2013).
108. Li, X. et al. Large-Area Graphene Single Crystals Grown by Low-Pressure Chemical Vapor Deposition of Methane on Copper. *Journal of the American Chemical Society* **133**, 2816-2819 (2011).
109. Hanlon, D. et al. Production of Molybdenum Trioxide Nanosheets by Liquid Exfoliation and Their Application in High-Performance Supercapacitors. *Chemistry of Materials* **26**, 1751-1763 (2014).

110. Camacho-López, M.A. et al. Micro-Raman study of the m-MoO_2 to α-MoO_3 transformation induced by cw-laser irradiation. *Optical Materials* **33**, 480-484 (2011).
111. Baker, M.A., Gilmore, R., Lenardi, C. & Gissler, W. XPS investigation of preferential sputtering of S from MoS_2 and determination of MoS_x stoichiometry from Mo and S peak positions. *Applied Surface Science.* **150**, 255-262 (1999).
112. Elibol, K. et al. Grain boundary-mediated nanopores in molybdenum disulfide grown by chemical vapor deposition. *Nanoscale* **9**, 1591-1598 (2017).
113. Werfel, F. & Minni, E. Photoemission study of the electronic structure of Mo and Mo oxides. *Journal of Physics C: Solid State Physics* **16**, 6091 (1983).
114. Bang, G.S. et al. Effective liquid-phase exfoliation and sodium ion battery application of MoS_2 nanosheets. *ACS applied materials & interfaces* **6**, 7084–7089 (2014).
115. Muneer, A. et al. Nanoscale investigation of charge transport at the grain boundaries and wrinkles in graphene film. *Nanotechnology* **23**, 285705 (2012).
116. Duong, D.L. et al. Probing graphene grain boundaries with optical microscopy. *Nature* **490**, 235-239 (2012).
117. Huang, P.Y. et al. Grains and grain boundaries in single-layer graphene atomic patchwork quilts. *Nature* **469**, 389-392 (2011).
118. Diehl, R., Brandt, G. & Salje, E. The crystal structure of triclinic WO_3. *Acta Crystallographica Section B: Structural Crystallography and Crystal Chemistry* **34**, 1105-1111 (1978).
119. Li, J. et al. Carbon nanotube sensors for gas and organic vapor detection. *Nano Letters* **3**, 929-933 (2003).
120. Schedin, F. et al. Detection of individual gas molecules adsorbed on graphene. *Nature materials* **6**, 652-655 (2007).
121. Ko, G. et al. Graphene-based nitrogen dioxide gas sensors. *Curr Appl Phys* **10**, 1002-1004 (2010).
122. Schmidt, H. et al. Transport Properties of Monolayer MoS_2 Grown by Chemical Vapor Deposition. *Nano Letters* **14**, 1909-1913 (2014).
123. Qiu, H. et al. Electrical characterization of back-gated bi-layer MoS_2 field-effect transistors and the effect of ambient on their performances. *Applied Physics Letters.* **100**, - (2012).
124. Das, S., Chen, H.-Y., Penumatcha, A.V. & Appenzeller, J. High Performance Multilayer MoS2 Transistors with Scandium Contacts. *Nano Letters* **13**, 100-105 (2012).
125. Perera, M.M. et al. Improved Carrier Mobility in Few-Layer MoS2 Field-Effect Transistors with Ionic-Liquid Gating. *ACS Nano* **7**, 4449-4458 (2013).
126. Yoon, Y., Ganapathi, K. & Salahuddin, S. How Good Can Monolayer MoS_2 Transistors Be? *Nano Letters* **11**, 3768-3773 (2011).
127. Zhao, P. et al. Effects of annealing on top-gated MoS_2 transistors with HfO_2 dielectric. *Journal of Vacuum Science & Technology B, Nanotechnology and Microelectronics: Materials, Processing, Measurement, and Phenomena* **35**, 01A118 (2017).
128. Cui, X. et al. Multi-terminal transport measurements of MoS_2 using a van der Waals heterostructure device platform. *Nature Nanotechnology.* **10**, 534-540 (2015).
129. Wirtz, C. et al. Atomic layer deposition on 2D transition metal chalcogenides: layer dependent reactivity and seeding with organic ad-layers. *Chemical Communications* **51**, 16553-16556 (2015).

130. Wilson, J.A. & Yoffe, A.D. The transition metal dichalcogenides discussion and interpretation of the observed optical, electrical and structural properties. *Advances in Physics.* **18**, 193-335 (1969).
131. Miró, P., Ghorbani-Asl, M. & Heine, T. Two Dimensional Materials Beyond MoS_2: Noble-Transition-Metal Dichalcogenides. *Angewandte Chemie International Edition* **53**, 3015-3018 (2014).
132. Miró, P., Audiffred, M. & Heine, T. An atlas of two-dimensional materials. *Chemical Society reviews* **43**, 6537-6554 (2014).
133. Ullah, K., Ye, S., Lei, Z., Cho, K.-Y. & Oh, W.-C. Synergistic effect of $PtSe_2$ and graphene sheets supported by TiO_2 as cocatalysts synthesized via microwave techniques for improved photocatalytic activity. *Catalysis Science & Technology* **5**, 184-198 (2015).
134. Wang, Y. et al. Monolayer $PtSe_2$, a New Semiconducting Transition-Metal-Dichalcogenide, Epitaxially Grown by Direct Selenization of Pt. *Nano Letters* **15**, 4013-4018 (2015).
135. O'Brien, M. et al. Raman characterization of platinum diselenide thin films. *2D Materials* **3**, 021004 (2016).
136. Zhuang, H.L. & Hennig, R.G. Computational Search for Single-Layer Transition-Metal Dichalcogenide Photocatalysts. *The Journal of Physical Chemistry C* **117**, 20440-20445 (2013).
137. Wang, Z., Li, Q., Besenbacher, F. & Dong, M. Facile Synthesis of Single Crystal $PtSe_2$ Nanosheets for Nanoscale Electronics. *Advanced Materials* **28**, 10224-10229 (2016).
138. Zhao, Y. et al. High-Electron-Mobility and Air-Stable 2D Layered $PtSe_2$ FETs. *Advanced Materials* **29**, 1604230 (2017).
139. Yim, C. et al. High-Performance Hybrid Electronic Devices from Layered $PtSe_2$ Films Grown at Low Temperature. *ACS Nano* **10**, 9550-9558 (2016).
140. Blum, V. et al. Ab initio molecular simulations with numeric atom-centered orbitals. *Computer Physics Communications* **180**, 2175-2196 (2009).
141. Tkatchenko, A. & Scheffler, M. Accurate Molecular Van Der Waals Interactions from Ground-State Electron Density and Free-Atom Reference Data. *Physical Review Letters.* **102**, 073005 (2009).
142. Togo, A., Oba, F. & Tanaka, I. First-principles calculations of the ferroelastic transition between rutile-type and $CaCl_2$-type SiO_2 at high pressures. *Physical Review B.* **78**, 134106 (2008).
143. Voiry, D. et al. Enhanced catalytic activity in strained chemically exfoliated WS_2 nanosheets for hydrogen evolution. *Nature materials* **12**, 850-855 (2013).
144. Wang, H. et al. Electrochemical tuning of vertically aligned MoS_2 nanofilms and its application in improving hydrogen evolution reaction. *Proceedings of the National Academy of Sciences* **110**, 19701-19706 (2013).
145. Jung, Y. et al. Metal Seed Layer Thickness-Induced Transition From Vertical to Horizontal Growth of MoS_2 and WS_2. *Nano Letters* **14**, 6842-6849 (2014).
146. Koch, C.T. Determination of core structure periodicity and point defect density along dislocations. *PhD Thesis* (2002).
147. Molina-Sanchez, A. & Wirtz, L. Phonons in single-layer and few-layer MoS_2 and WS_2. *Physical Review B.* **84**, 155413 (2011).
148. Perdew, J.P. Density functional theory and the band gap problem. *International Journal of Quantum Chemistry* **28**, 497-523 (1985).
149. Ghorbani-Asl, M., Kuc, A., Miró, P. & Heine, T. A Single-Material Logical Junction Based on 2D Crystal PdS_2. *Advanced Materials* **28**, 853-856 (2016).

150. Cingolani, A., Lugarà, M. & Lévy, F. Resonance Raman scattering in $HfSe_2$ and HfS_2. *Physica Scripta* **37**, 389 (1988).
151. Cingolani, A., Ferrara, M., Lugarà, M. & Lévy, F. The Raman spectra of CdI_2. *Solid State Communications* **50**, 911-913 (1984).
152. Arguello, C.A., Rousseau, D.L. & Porto, S.P.S. First-Order Raman Effect in Wurtzite-Type Crystals. *Physical Review* **181**, 1351-1363 (1969).
153. Tan, S.M. et al. Pristine Basal- and Edge-Plane-Oriented Molybdenite MoS_2 Exhibiting Highly Anisotropic Properties. *Chemistry – A European Journal* **21**, 7170-7178 (2015).
154. O'Brien, M. et al. Mapping of Low-Frequency Raman Modes in CVD-Grown Transition Metal Dichalcogenides: Layer Number, Stacking Orientation and Resonant Effects. *Scientific reports* **6**, 19476 (2016).
155. Wang, X. et al. Chemical Vapor Deposition Growth of Crystalline Monolayer $MoSe_2$. *ACS Nano* (2014).
156. Tongay, S. et al. Thermally Driven Crossover from Indirect toward Direct Bandgap in 2D Semiconductors: $MoSe_2$ versus MoS_2. *Nano Letters* **12**, 5576-5580 (2012).
157. Ross, J.S. et al. Electrical control of neutral and charged excitons in a monolayer semiconductor. *Nature Communications.* **4**, 1474 (2013).
158. Tan, P.H. et al. The shear mode of multilayer graphene. *Nature materials* **11**, 294-300 (2012).
159. Song, I., Park, C. & Choi, H.C. Synthesis and properties of molybdenum disulphide: from bulk to atomic layers. *RSC Advances* **5**, 7495-7514 (2015).
160. Puretzky, A.A. et al. Low-Frequency Raman Fingerprints of Two-Dimensional Metal Dichalcogenide Layer Stacking Configurations. *ACS Nano* **9**, 6333-6342 (2015).
161. Suzuki, R. et al. Valley-dependent spin polarization in bulk MoS_2 with broken inversion symmetry. *Nature nanotechnology.* **9**, 611-617 (2014).
162. Xia, M. et al. Spectroscopic Signatures of AA′ and AB Stacking of Chemical Vapor Deposited Bilayer MoS_2. *ACS Nano* **9**, 12246–12254 (2015).
163. Lui, C.H. et al. Observation of interlayer phonon modes in van der Waals heterostructures. *Physical Review B.* **91**, 165403 (2015).
164. van der Zande, A.M. et al. Tailoring the Electronic Structure in Bilayer Molybdenum Disulfide via Interlayer Twist. *Nano Letters* **14**, 3869-3875 (2014).
165. Withers, F. et al. Light-emitting diodes by band-structure engineering in van der Waals heterostructures. *Nature materials* **14**, 301-306 (2015).
166. Gong, Y. et al. Vertical and in-plane heterostructures from WS_2/MoS_2 monolayers. *Nature materials* **13**, 1135-1142 (2014).
167. Terrones, H. et al. New First Order Raman-active Modes in Few Layered Transition Metal Dichalcogenides. *Scientific reports* **4**, 4215 (2014).
168. Tonndorf, P. et al. Photoluminescence emission and Raman response of monolayer MoS_2, $MoSe_2$, and WSe_2. *Optics Express* **21**, 4908-4916 (2013).
169. Zhao, W.J. et al. Evolution of Electronic Structure in Atomically Thin Sheets of WS_2 and WSe_2. *ACS Nano* **7**, 791-797 (2013).
170. Xia, J. et al. CVD synthesis of large-area, highly crystalline $MoSe_2$ atomic layers on diverse substrates and application to photodetectors. *Nanoscale* **6**, 8949-8955 (2014).
171. Conley, H. et al. Bandgap Engineering of Strained Monolayer and Bilayer MoS_2. *Nano Letters* **13**, 3626–3630 (2013).
172. Castellanos-Gomez, A. et al. Local Strain Engineering in Atomically Thin MoS_2. *Nano Letters* **13**, 5361-5366 (2013).

173. Lui, C.H. & Heinz, T.F. Measurement of layer breathing mode vibrations in few-layer graphene. *Physical Review B.* **87**, 121404 (2013).

174. Zhao, Y. et al. Interlayer breathing and shear modes in few-trilayer MoS_2 and WSe_2. *Nano Letters* **13**, 1007-1015 (2013).

175. Chen, S.-Y., Zheng, C., Fuhrer, M.S. & Yan, J. Helicity-Resolved Raman Scattering of MoS_2, $MoSe_2$, WS_2, and WSe_2 Atomic Layers. *Nano Letters* **15**, 2526-2532 (2015).

176. Liu, Z. et al. Strain and structure heterogeneity in MoS_2 atomic layers grown by chemical vapour deposition. *Nature Communications.* **5** (2014).

177. Lee, J.-U. et al. Raman Signatures of Polytypism in Molybdenum Disulfide. *ACS Nano* **10**, 1948-1953 (2016).

178. Lu, X. et al. Large-Area Synthesis of Monolayer and Few-Layer $MoSe_2$ Films on SiO_2 Substrates. *Nano Letters* **14**, 2419-2425 (2014).

179. Shaw, J. et al. Chemical vapor deposition growth of monolayer $MoSe_2$ nanosheets. *Nano Research,* **7**, 511-517 (2014).

180. Duan, X. et al. Lateral epitaxial growth of two-dimensional layered semiconductor heterojunctions. *Nature Nanotechnology.* **9**, 1024-1030 (2014).

181. Siwei, L. et al. Formation of ripples in atomically thin MoS_2 and local strain engineering of electrostatic properties. *Nanotechnology* **26**, 105705 (2015).

182. Zhang, K. & Arroyo, M. Understanding and strain-engineering wrinkle networks in supported graphene through simulations. *Journal of the Mechanics and Physics of Solids* **72**, 61-74 (2014).

183. del Corro, E. et al. Excited Excitonic States in 1L, 2L, 3L, and Bulk WSe_2 Observed by Resonant Raman Spectroscopy. *ACS Nano* **8**, 9629-9635 (2014).

184. Pimenta, M.A., del Corro, E., Carvalho, B.R., Fantini, C. & Malard, L.M. Comparative Study of Raman Spectroscopy in Graphene and MoS_2-type Transition Metal Dichalcogenides. *Accounts of Chemical Research* **48**, 41-47 (2015).

185. Huang, J.-K. et al. Large-Area Synthesis of Highly Crystalline WSe_2 Monolayers and Device Applications. *ACS Nano* **8**, 923-930 (2014).

186. Kai, X. et al. Atomic-layer triangular WSe_2 sheets: synthesis and layer-dependent photoluminescence property. *Nanotechnology* **24**, 465705 (2013).

187. Zeng, H. et al. Optical signature of symmetry variations and spin-valley coupling in atomically thin tungsten dichalcogenides. *Scientific reports* **3** (2013).

188. Carvalho, B.R., Malard, L.M., Alves, J.M., Fantini, C. & Pimenta, M.A. Symmetry-Dependent Exciton-Phonon Coupling in 2D and Bulk MoS_2 Observed by Resonance Raman Scattering. *Physical Review Letters.* **114**, 136403 (2015).

189. Cong, C. et al. Synthesis and Optical Properties of Large-Area Single-Crystalline 2D Semiconductor WS_2 Monolayer from Chemical Vapor Deposition. *Advanced Optical Materials* **2**, 131-136 (2014).

190. Lee, J.-U., Park, J., Son, Y.-W. & Cheong, H. Anomalous excitonic resonance Raman effects in few-layered MoS_2. *Nanoscale* **7**, 3229-3236 (2015).

191. Zeng, H. et al. Low-frequency Raman modes and electronic excitations in atomically thin MoS_2 films. *Physical Review B.* **86**, 241301 (2012).

192. Smith, A.D. et al. Electromechanical Piezoresistive Sensing in Suspended Graphene Membranes. *Nano Letters* **13**, 3237-3242 (2013).

193. Smith, A.D. et al. Piezoresistive Properties of Suspended Graphene Membranes under Uniaxial and Biaxial Strain in Nanoelectromechanical Pressure Sensors. *ACS Nano* **10**, 9879-9886 (2016).

194. Jin, T., Kang, J., Su Kim, E., Lee, S. & Lee, C. Suspended single-layer MoS_2 devices. *Journal of Applied Physics.* **114**, 164509 (2013).

195. Bolotin, K.I. et al. Ultrahigh electron mobility in suspended graphene. *Solid State Communications* **146**, 351-355 (2008).
196. van der Zande, A.M. et al. Large-Scale Arrays of Single-Layer Graphene Resonators. *Nano Letters* **10**, 4869-4873 (2010).
197. Lee, J.-U., Kim, K. & Cheong, H. Resonant Raman and photoluminescence spectra of suspended molybdenum disulfide. *2D Materials* **2**, 044003 (2015).
198. Scheuschner, N. et al. Photoluminescence of freestanding single- and few-layer MoS_2. *Physical Review B.* **89**, 125406 (2014).
199. Frey, G.L., Tenne, R., Matthews, M.J., Dresselhaus, M.S. & Dresselhaus, G. Raman and resonance Raman investigation of MoS_2 nanoparticles. *Physical Review B.* **60**, 2883-2892 (1999).
200. Hallam, T., Berner, N.C., Yim, C. & Duesberg, G.S. Strain, Bubbles, Dirt, and Folds: A Study of Graphene Polymer-Assisted Transfer. *Advanced Materials Interfaces* **1**, 1400115 (2014).
201. Qin, P. et al. In situ growth of double-layer MoO_3/MoS_2 film from MoS_2 for hole-transport layers in organic solar cell. *Journal of Materials Chemistry A* **2**, 2742-2756 (2014).
202. O'Brien, M. et al. Low wavenumber Raman spectroscopy of highly crystalline $MoSe_2$ grown by chemical vapor deposition. *physica status solidi (b)* **252**, 2385-2389 (2015).
203. Tongay, S. et al. Monolayer behaviour in bulk ReS_2 due to electronic and vibrational decoupling. *Nature Communications.* **5**, 3252 (2014).
204. Feng, Q. et al. Growth of Large-Area 2D $MoS_{2(1-x)}Se_{2x}$ Semiconductor Alloys. *Advanced Materials.* **26**, 2648-2653 (2014).